

Novel Engineered Refractory Materials for Advanced Reactor Applications

**Fuel Cycle/Reactor Concepts
Mission Relevant Investigator Initiative Research**

Steven Shannon
North Carolina State University

In collaboration with:
University of Tennessee

Sue Lesica, Federal POC
Bulent Biner, Technical POC

Novel engineered refractory materials for advanced reactor applications

Final Report

For the period September 2010 - May 2015

Principal Investigator: Steven C. Shannon^{1,*}

Collaborators: Jon-Paul Maria², Jacob Eapen¹, William Weber³

Students: Matthew Cabral¹, Christopher Hardiman¹,

1. North Carolina State University, Department of Nuclear Engineering, 2500 Stinson Drive, Campus Box 7909, Raleigh NC 27695-7909
2. North Carolina State University, Department of Materials Science and Engineering, 911 Partners Way, Raleigh, NC 27606
3. University of Tennessee, Department of Materials Science and Engineering, 414 Ferris Hall 1508 Middle Drive, The University of Tennessee, Knoxville, TN 37996-2100

* Primary point of contact. Phone/SMS (919) 802-7255, Fax (919) 515-5115, eMail: scshannon@ncsu.edu

Papers

Annamareddy V.A., Eapen J. (2015). Mobility propagation and dynamic facilitation in superionic conductors. *Journal of Chemical Physics* 143, accepted for publication

Imada, K., Ishimaru, M., Sato, K., Xue, H., Zhang, Y., Shannon, S., et al. (2015). Atomistic structures of nano-engineered SiC and radiation-induced amorphization resistance. *Journal of Nuclear Materials*, 465, 433-437.

Jamison, L., Sridharan, K., Shannon, S., & Szlufarska, I. (2014). Temperature and irradiation species dependence of radiation response of nanocrystalline silicon carbide. *Journal of Materials Research*, 29(23), 2871-2880.

Chen, C., Zhang, Y., Fu, E., Wang, Y., Crespillo, M. L., Liu, C., et al. (2014). Irradiation-induced microstructural change in helium-implanted single crystal and nano-engineered SiC. *Journal of Nuclear Materials*, 453(1), 280-286.

Zhang, Y., Varga, T., Ishimaru, M., Edmondson, P., Xue, H., Liu, P., et al. (2014). Competing effects of electronic and nuclear energy loss on microstructural evolution in ionic-covalent materials. *Nuclear Instruments and Methods in Physics Research Section B: Beam Interactions with Materials and Atoms*, 327, 33-43.

Jamison, L., Zheng, M., Shannon, S., Allen, T., Morgan, D., & Szlufarska, I. (2014). Experimental and ab initio study of enhanced resistance to amorphization of nanocrystalline silicon carbide under electron irradiation. *Journal of Nuclear Materials*, 445(1), 181-189.

Annamareddy, V. A., Nandi, P. K., Mei, X., & Eapen, J. (2014). Waxing and waning of dynamical heterogeneity in the superionic state. *Physical Review E*, 89(1), 010301.

Ishimaru, M., Zhang, Y., Shannon, S., & Weber, W. J. (2013). Origin of radiation tolerance in 3C-SiC with nanolayered planar defects. *Applied Physics Letters*, 103(3), 033104.

Zhang, Y., Ishimaru, M., Varga, T., Oda, T., Hardiman, C., Xue, H., et al. (2012). Nanoscale engineering of radiation tolerant silicon carbide. *Physical Chemistry Chemical Physics*, 14(38), 13429-13436.

Hardiman C.M.(2013). *Characterization of the Effect of Radiation Damage on the Thin-Film Stress Behavior of Nanocrystalline 3C SiC*. (Master's Thesis) Retrieved from the NCSU Institutional Repository (<http://www.lib.ncsu.edu/resolver/1840.16/8841>)

Cabral M.J. (2013). Electrical characterization of radiation induced defects in 3C-SiC. (Master's Thesis) Retrieved from the NCSU Institutional Repository (<http://www.lib.ncsu.edu/resolver/1840.16/8485>)

Networks or Collaborations Fostered

Dr. Todd Allen, Idaho National Laboratory / University of Wisconsin

Dr. Laura Jameson, University of Wisconsin

Dr. Isabella Szlufarska, University of Wisconsin

Dr. Yanwen Zhang, University of Tennessee

Dr. Manabu Ishimaru, Osaka University

Dr. Kenta Imada, Kyushu Institute of Technology

Dr. Kazuhisa Sato, Tohoku University

Summary

This report summarizes the results of DOE-NEUP grant 10-853 titled “Novel engineered refractory materials for advanced reactor applications”. The project spanned 48 months (36 months under the original grant plus a 12 month no cost extension). The overarching goal of this work was to fabricate and characterize refractory materials engineered at the atomic scale with emphasis on their tolerance to accumulated radiation damage. With an emphasis on nano-scale structure, this work included atomic scale simulation to study the underlying mechanisms for modified radiation tolerance at these atomic scales.

To achieve these goals, this project was broken into four primary tasks with well defined deliverables and milestones. Although these tasks were intended to break up the project into smaller thrusts, each leveraged the activities of the other three tasks to strengthen the effort beyond the sum of the parts. These tasks were defined as follows:

- *Synthesis of refractory materials with controllable nano-scale structure* - the overarching deliverable of this task was to generate reproducible highly controllable process flows for the fabrication of refractory materials with controllable properties spanning from the macroscopic (material stress, thickness, etc.) to the nanoscale (crystalline size, orientation, shape, grain condition, etc.). Using material synthesis techniques derived from micro- and nanoelectronic fabrication processes, methodologies were advanced for the controllable synthesis of silicon carbide and cerium oxide. Grain size, crystal orientation, grain shape (equiax vs. columnar), and film stress were controlled, varied, and characterized for irradiation study.
- *Characterization of fabricated materials* - the overarching deliverable of this task was to establish metrology processes for the measurement of changes in material properties due to irradiation, with emphasis on low dose conditions where the onset of damage could be studied. This task focused on both traditional metrology methods and electrical measurements of devices fabricated using the synthesized materials from the first task. The goal of the electrical measurement effort was to move towards in-situ characterization of materials during controlled irradiation experiments. TEM, SEM, XPS, and XRD measurements of pre and post irradiated samples were combined with pre and post electrical characterization of resistors, diodes, micromachined cantilevers, and capacitors fabricated with 3C SiC and ceria.
- *Simulation of the onset and accumulation of radiation damage* - the overarching deliverable for this task was to work in synergy with experimental efforts to simultaneously provide insight into first principle mechanisms for observed irradiation trends and leverage experimental efforts to validate simulation code development. Simulation efforts focused on damage accumulation in UO_2 and the influence of grain boundaries in damage accumulation in SiC. In this work, new pathways for damage recovery in UO_2 were identified, the influence of grain boundaries in SiC damage recovery was quantified, and the experimentally observed stacking fault induced recovery pathways in SiC were demonstrated.
- *Controlled irradiation of fabricated material* - this task's main goal was to provide controllable, repeatable irradiation of samples with the capability to measure material properties in-situ to study the accumulation of radiation damage at very low doses. The ion beam irradiation facility

at the University of Tennessee was the primary facility for irradiation work. In collaboration with the investigators at Tennessee, extensive irradiation of ceria and SiC was carried out at various doses. A novel sample stage that enabled in-situ characterization of electrical devices with a semiconductor device characterization system was designed and constructed; electrical measurements as a function of total ion beam dose revealed good correlation between ex-situ material measurements and electrical trends.

In the next four sections, activities for each of these four tasks are expanded on. The results presented focus primarily on results previously reported in article published as part of this effort.

Task 1: Controllable synthesis of refractory materials with well defined nano-scale microstructure

Silicon carbide (3C polyform) and cerium oxide were synthesized utilizing material processing techniques more commonly employed in electronic device fabrication. The reason for employing these techniques are two-fold. The first is that these techniques are born out of an application that demands material control down to the nanoscale, and therefore enables controlled engineering of these materials to scales of interest for this study. Second, these techniques enable material synthesis to be part of a larger process flow that enables patterning and layering to form simple electronic devices where the material of interest is the active electrical component. This thereby enables material characterization through device characterization. This section covers the synthesis and characterization of these materials for irradiation study.

1.1.Synthesis and characterization of nano-crystalline SiC: process development, material characterization, and demonstration of controlled, measurable films stresses using micromachined cantilevers.

3C-SiC was synthesized on single crystal silicon wafers with [100] orientation using a thermal chemical vapor deposition process. Chemical vapor deposition (CVD) involves the process of chemically reacting volatile compounds which contain the desired constituents that make up the film with other gases in order to produce a nonvolatile solid which deposits atomistically on a substrate. One thing that makes CVD so unique is that the controllable growth of films with varying stoichiometry is possible.¹ The governing mechanisms of any CVD process can be divided into the following stages: introduction of chemically reactive gaseous species into the reactor, diffusion of the reactants to the substrate, adsorption of the reactants on the substrate, chemical reaction of the reactant and the substrate, and the desorption and gaseous transport of any reaction by-products out of the reactor.

The manner in which a thin-film grows depends on several growth process factors such as pressure, substrate temperature, the ratio of the individual reactants introduced, and the substrate on which the thin-film is grown. Regardless of the material being grown, the progression of thin-film formation involves stages of nucleation and growth. The beginning stages of film growth occur when a sufficient number of the reactant vapor atoms/molecules condense on the substrate. This is known as nucleation and after enough atoms have bonded together, small clusters or islands are formed.¹ These islands are highly mobile and as adatoms impinge on the small clusters, the islands grow in size and the density of islands

on the substrate increases rapidly. The collection of smaller clusters and subsequent merging of the islands occurs by a process of coalescence, which ultimately decreases the island density by forming a connected network of larger islands between which denuded zones exist. The isolated denuded zones are free of condensed reactant atoms and thus further nucleation can occur. With further deposition, these denuded zones fill in and shrink due to coalescence and the process proceeds until a continuous layer exists.

There are three accepted modes regarding thin-film nucleation and growth for CVD processes: Volmer-Weber, Frank-Van der Merwe, and Stranski-Krastanov. In the Volmer-Weber model nucleation of the film occurs in the form of discrete 3D nuclei on the surface of the substrate. The film growth progresses by an increase in both the number and size of the present nuclei. This increases until the nuclei inter-grow with each other to form a continuous film. In the Frank and Van der Merwe model, film growth tends to proceed in a layer-by-layer growth. This is due to the fact that adatoms are more likely to attach to the substrate surface than to other film material surfaces.² Once small islands are formed, additional adatoms form on the periphery of the islands where they can bond directly to both the substrate and film atoms. This process proceeds by subsequent epitaxial growth. The Stransky-Krastanov model combines features of the two previous models. Nucleation and growth occurs in a layer-by-layer manner until a finite number of monolayers are produced. Subsequent film formation occurs by the formation of discrete nuclei as described by the Volmer-Weber model.^{2,3}

Silicon carbide is only just beginning to become a widespread substitute for Si as the semiconductor material of choice due in no small part to issues regarding the deposition of SiC films. For most MEMS applications Si/polysilicon films can be grown on a mass production scale using relatively low temperatures and simple resistive heating furnaces. SiC presents a greater challenge due to its structure. When heteroepitaxially growing SiC on Si the resulting thermal mismatch results in residual stresses of the SiC film as is the case when growing any thin-film material heteroepitaxially. One material property of SiC that is very promising for applications to MEMS also poses a considerable problem for deposition of SiC, with that being the thermodynamic stability of SiC at very high temperatures. This makes the use of an annealing process to eliminate the residual stresses impractical.⁴ The only practical method in reducing the film stress of the SiC film is to adjust certain parameters in the furnace process being used to grow thin-film material.

Several techniques have been developed for growing the three most relevant polytypes: 3C, 4H, and 6H. 3C SiC has emerged as the polytype of choice in MEMS applications because it can be heteroepitaxially grown on Si which is readily available. The two hexagonal polytypes form at temperatures above the melting point of Si making synthesis on Si wafers impossible.⁴ However, 6H SiC pressure and acceleration sensors have been fabricated by growing epitaxial 6H films on commercially available 6H SiC wafers using CVD furnace processes similar to those commonly used in the fabrication of Si devices.⁴ Due to the preference of 3C SiC in MEMS applications the following discussion of various deposition techniques is geared toward the 3C polytype.

Atmospheric Pressure Chemical Vapor Deposition (APCVD) was one of the first techniques used to grow epitaxial 3C and 6H SiC films mainly because this method has fewer components that are sensitive to temperature than low-pressure systems. This is advantageous for SiC epitaxy since typical temperatures

range from approximately 900 to 1300 °C for the growth of 3C films on Si substrates to over 1700 °C for 6H growth on 6H SiC substrates.⁴ In general, APCVD reaction chambers consist of a double walled fused silica tube which has chilled water running between the walls. Maintaining a low temperature on the chamber walls acts to minimize deposition, as well as any particulate formation.⁴ These systems can be either orientated horizontally or vertically, with the latter being useful for larger wafer sizes and can also serve to minimize particulate deposition on the substrate due to the vertical orientation of the wafer. To achieve the high temperatures for deposition needed in order for epitaxial growth, the substrates are loaded onto a susceptor which is coated with SiC. This SiC coated, graphite piece is placed central in the chamber with respect to the RF-driven induction coils wound around the chamber. This susceptor is heated by the RF coils through induction to the elevated temperatures required for SiC CVD growth.

The most common APCVD process for growing 3C SiC on Si involves exposing the Si wafer to a hydrocarbon gas mixed with an H₂ carrier gas and heating the susceptor to roughly 1300 °C. The most common of the hydrocarbon gases used in this type of process is propane (C₃H₈). Over about a 90 second period, the gas flow and temperature control is held constant during which a process known as carbonization occurs. The carbonization process consists of the propane gas flowing over the heated sample where it is decomposed into reactive hydrocarbon radicals. These radicals readily react with the free Si atoms to form a thin layer of SiC.⁵ This process alone is not the sole means of growing the 3C SiC films because the growth rates tend to be nonlinear, dropping off with time.^{4,5} To produce the several micron thicknesses used in MEMS applications, the growth rate is increased by the addition of a gas containing Si, typically silane (SiH₄) into the carrier gas.^{4,5} This process is not limited to epitaxial growth of SiC and a similar process has been created to grow polycrystalline, 3C SiC films.⁵ Poly-SiC films have been shown to be more versatile in MEMS applications because they can be grown on several different substrates i.e. SiO₂, polysilicon, and Si₃N₄.⁴ The process for growing Poly-SiC varies with the substrate, but if the substrate is amorphous then a carbonization stage is not very effective and the susceptor is heated to a temperature slightly lower than that for heteroepitaxial 3C SiC growth and the precursor gases are injected .

Another important growth technique used in SiC MEMS fabrication is plasma-enhanced chemical vapor deposition (PECVD). PECVD enables SiC films to be formed at much lower temperatures than APCVD in the range of just 200-400 °C. Typically the microstructure of as-deposited PECVD SiC films is amorphous but crystalline SiC films can be achieved by a post-growth anneal.⁴ PECVD SiC is particularly useful because it can be deposited using commercially available PECVD systems due to its amorphous nature. Typical precursor gases used in PECVD processes include SiH₄, CH₄, and C₆H₁₈Si₂. With the latter, hexamethyldisilane, being a single precursor feed gas. The low operating temperature is due to the process being controlled by the electron temperature, T_e, of the plasma.

Perhaps the most widely used method of SiC film growth, however, is low pressure chemical vapor deposition (LPCVD). This process allows for a wide range of precursors to be used and due to the low processing pressure film thicknesses tend to be more uniform than the previously mentioned APCVD method⁴ . For epitaxial 3C SiC growth, several processes exist using both single and dual precursors. Processes involving single precursors can be used for epitaxial 3C growth without a need for a carbonization stage and at lower temperatures than APCVD and dual precursor LPCVD processes.⁴ One such process which is useful in the development of free-standing 3C SiC membranes for sensors involves

the use of mono-methylsilane ($\text{H}_3\text{Si-CH}_3$) which yielded 3C SiC films on Si substrates at temperatures as low as 1000 °C.⁴ An example of dual precursors used in the epitaxial growth of 3C SiC involved the use of dichlorosilane or DCS (SiH_2Cl_2) and acetylene (C_2H_2) over a much lower temperature range of 750-1050 °C with the maximum temperature corresponding to the film growth steps. Using a multiple step process which involved an initial carbonization stage, the DCS and acetylene flows were alternated such that the first step involved the deposition of a thin Si epitaxial layer and the second carbon-based precursor carbonized the Si layer producing a SiC epitaxial film.⁴

LPCVD is also widely used to deposit polycrystalline 3C SiC films, which is quickly becoming the dominant crystalline phase in SiC MEMS. Since the growth of poly-SiC films does not require an initial carbonization step prior to film growth, LPCVD growth of polycrystalline 3C SiC only requires that the precursors dissociate and react at a specified substrate temperature. Both single and dual precursors can be used for the growth of poly-3C SiC. This process involves the use of the dual precursors DCS and acetylene and can deposit MEMS quality poly-3C SiC films at temperatures ranging from 750-900 °C and pressures from 460 mTorr to 5 Torr.⁴

The process used to grow the 3C SiC is similar to already reported LPCVD processes discussed previously. The poly-SiC films were deposited on 100 mm diameter (100) silicon wafers in a high-throughput, hot-wall, horizontal furnace using the dual precursor gases dichlorosilane (SiH_2Cl_2) and acetylene (C_2H_2) as the supply of silicon and carbon. In order to produce semiconductor-grade poly-SiC films, ammonia was incorporated to introduce nitrogen as an in-situ n-type dopant in order to study the effects of radiation on electrical performance. In most of the runs made, the ammonia gas flow was minimal in order to grow thin-films for mechanical characterization. However, since the characterization involved an already established baseline process, the gas flow parameters were held constant and a 7 sccm NH_3 flow was present for each undoped run. The dual-precursor gases were introduced into the cylindrical reaction chamber simultaneously following an initial carbonization stage in which an ultra-thin carbon film was deposited on the silicon substrate. The purpose of the initial carbon film is to promote stoichiometry and to improve the uniformity of the SiC films.^{6,7} The gas flow rates during the main deposition step of the process were held constant for the duration. The temperature of the LPCVD process was also constant and was maintained along the length of the quartz tube at 900 °C. Figure 1.1.1 shown below depicts the LPCVD process used with temperature as a function of time.

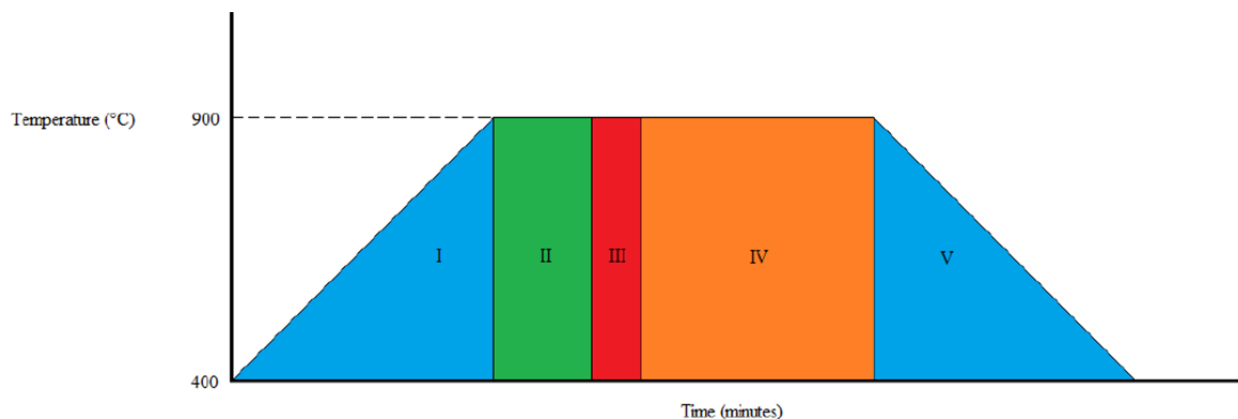


Figure 1.1.1 - Process flow for 3C SiC synthesis

The initial step of the LPCVD process (I) represents a ramp-up stage for the heating coils in the furnace tube for which the ambient temperature varied between 400 and 424 °C. Step II involved a temperature stabilization to eliminate any deviation and nonuniformity of the temperature measured at the back, center, and front of the quartz tube. In addition, this step included an N₂ purge where a maximum nitrogen flow was introduced in order to automatically adjust the throttle valve position to the predetermined growth process pressure. The carbonization of the silicon substrate was conducted in step III and involved a two-minute flow of C₂H₂ mixed with a hydrogen carrier gas. Step IV in Figure 1.1.1 represents the bulk growth step of the 3C SiC thin-film. The time of the main deposition stage depends exclusively on the deposition pressure and the desired thickness. This is due to the fact that the process pressure was found to directly affect the deposition rate as is shown below in Figure 1.1.2. All deposition rates were determined for the wafer that corresponded to the middle position with respect to the other wafers in the run. Typically each run consisted of 3-4 wafers in all. The deposition rates were found to be consistent across the small section of the quartz boat. It is important to note that the undoped 3C SiC thin-films grown using this process included a small amount of ammonia since the undoped films were run with the baseline process on the LPCVD furnace.

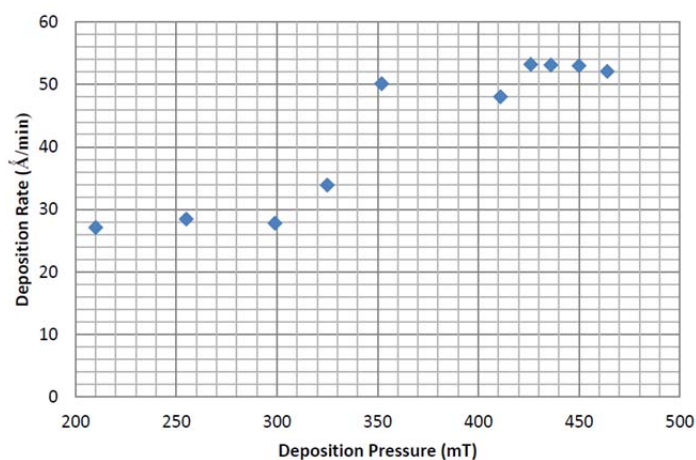


Figure 1.1.2 - 3C SiC deposition rate vs. pressure for fixed temperature and gas flow

Evaluation of the radiation tolerance of material under mechanical stress is important for capturing stress driven mechanisms for radiation damage acceleration or remediation. Thin film growth of materials of

interest on dissimilar substrates presents a pathway for designing material systems for irradiation studies under stressed conditions.

A common concern for materials used in the fabrication of MEMS structures is residual stress and stress gradient in thin-films. It has been reported in literature that poly-SiC films deposited on silicon substrates generally exhibit high residual stress and stress gradients.⁸ For MEMS applications, the residual stress and stress gradients can be highly detrimental to the performance of MEM devices. For instance, highly tensile stresses can result in deformation of the active structures and highly compressive stresses can lead to buckling of clamped structures. Residual stress gradients can also result in deflection of cantilever structures that is out-of-plane. While the effects of high residual stress are undesirable in MEMS application, they are the basis of this report as an effective method of determining the change in the stress characteristics of the thin-film SiC as a result of radiation damage.

Stress in thin films is divided into two categories: intrinsic and extrinsic stresses. Intrinsic or growth stresses are strongly dependent on the mobility of adatoms on the growth surface and the mobility of the grain boundaries during growth⁹, as well as the homologous temperature ($T_{\text{sub}}/T_{\text{melt}}$). The main source of extrinsic stress for the growth of nanocrystalline 3C-SiC on Si is the difference in the thermal expansion coefficient (~8%) which results in the external loading as a result of the post-growth temperature change. This effect is constant and repeatable provided the substrate and film thicknesses are consistent. Therefore understanding the development of the intrinsic stress is an important aspect since it can be directly controlled through adjustment of the growth parameters.

It is first important to understand the nature of the measureable effect of residual stresses present in film-substrate systems. The initial assumptions are that the film and substrate are represented as two thin plates, each of which have different lateral dimensions, and that the thickness of the film is much smaller than that of the substrate.¹ Following the adhesion of the film to the substrate, the film seeks to recover its previous lateral dimensions and this in turn causes the substrate to deform to reach a new equilibrium state. The actual bending occurs due to the presence of bending moments at the edges of the film-substrate stack. The induced strain on the substrate caused by the thin-film seeking to return to its original geometry is due to several stress mechanisms which for polycrystalline films are thermal and intrinsic in nature.

The cause of the strain induced matching of the thin-film to the substrate is predominantly caused by lattice mismatching for single-crystal SiC. This is caused by the ~22% difference in the lattice constants of SiC and Si. In poly-SiC this is due to the mismatch (~8%) of the thermal expansion coefficients as well as intrinsic, microstructure strain as a result of defects such as stacking faults and twins and the nature of the grain growth and the evolution of the grain structure.¹⁰ Regardless of the cause the measureable response of residual stress is general, a film which is stretched to match the surface area of the substrate will generate uncompensated bending moments at the edges which will bend the substrate upwards and result in a residual tensile stress state in the thin-film and vice versa for a film which has a compressive stress state.¹ The bending is ultimately the result of counterbalancing the bending moments that are generated as a result of the deformation induced. These thermal and intrinsic strain mechanisms are superimposed as a total residual stress in the film which was measured using mechanical profilometry and quantified using the Stoney relation. This approximation of film stress is given by

$$\sigma = \frac{1}{6R} \frac{E_s d_s^2}{(1-\nu_s) d_f} \quad 1.1.1$$

where R is the radius of curvature of the thin-film/substrate, E_s is Young's modulus of the substrate, d_s is the thickness of the substrate, d_f is the thickness of the film, and ν_s is the Poisson ratio of the substrate. A more accurate model, especially for the 3C SiC films discussed in this report includes the contribution of thermally induced strain on the extent of bowing is

$$\frac{1}{R} = \frac{6E_f(1-\nu_s)}{E_s(1-\nu_f)} \frac{d_f}{d_s^2} (\alpha_s - \alpha_f) \Delta T \quad 1.1.2$$

where α_s and α_f are the thermal expansion coefficients of the substrate and film, respectively and ΔT is the difference between the temperature of the growth process and room temperature.¹ This deflection is based on a thermal stress addition to the Stoney relation

$$\sigma_f(T) = (\alpha_s - \alpha_f) \Delta T \frac{E_f}{(1-\nu_f)} \quad 1.1.3$$

There are some assumptions in determining residual film stress by using the Stoney formula that affects the accuracy of this model. This method assumes that substrate deflections are initially small for all dimensions, which is a reasonable assumption since the initial silicon wafers are relatively flat, indicating low residual stress in the pre-deposited substrate. This is evident by the pre-deposition scans taken for a typical run made while creating the stress matrix. All curvature measurements were made at three standard angles and the stress is determined using a built in algorithm based on Equation 1.1.2. A second assumption made by the Stoney relation is that both the film and substrate material properties are homogeneous and isotropic.¹¹ This is not quite accurate as the difference in the maximum and the average stress in some runs was found to be over 100 MPa.

In order to control the residual stress state of the thin films, the deposition pressure was adjusted between 210 and 475 mTorr. Adjusting pressure as a means of controlling film stress was previously reported by Fu, et al.⁸ Fu and his colleagues presented a general trend of increasing compressive thin film stress state with increasing deposition pressure, however further increases in deposition pressure resulted in a saturation at -98 MPa. That same observation was made in this work as well, albeit at a much lower pressure.

The method used in the analysis of the residual film stress consisted of using a stylus-type profilometer to measure the wafer curvature at three angles relative to the major flat of the (100) Si wafer. Of these three scan angles one was perpendicular to the main flat and one parallel to the main flat. The curvature of the silicon wafers were measured before and after deposition and a stress was determined based on Equation 1.1.2. The stress values from the three scan angles were then averaged in order to get a single value for the residual stress. Shown below in Figure 1.1.3, is the experimental data of residual film stress as a function of process pressure for wafers located in the center of the range of slots used in the furnace boat. The purpose of using a small range of slots was due to the observed stress variation with respect to wafer position along the length of the furnace tube. It is a worthy note that the residual stresses obtained for this

process are comparable to predicted stresses seen by the SiC layers in TRISO fuel during normal operation.¹

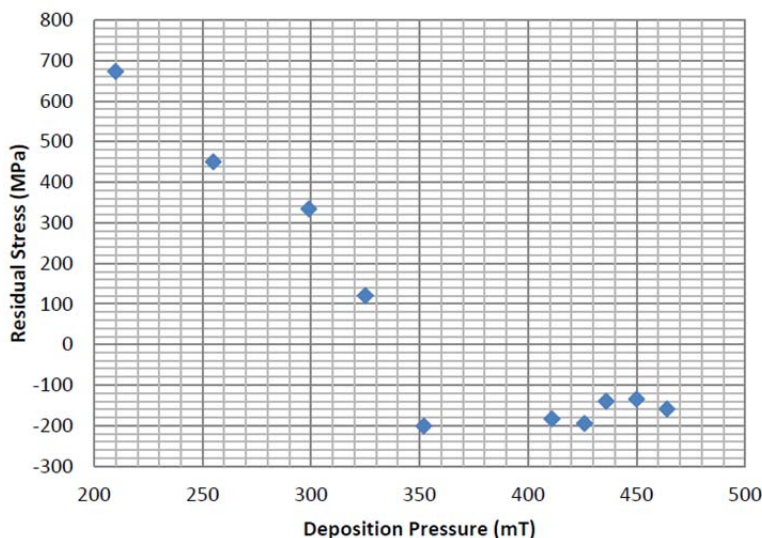


Figure 1.1.3 - Residual stress vs. deposition pressure for 3C SiC deposition processes

A possible explanation of this behavior involves the difference in the grain sizes observed at low and high pressure states.⁸ These are directly impacted by the LPCVD process parameters and general geometry of the reactor chamber. In addition, the residual stress has also been attributed to the grain formation at the film-substrate interface. It has been observed that for highly compressive 3C SiC films the grains are more aligned suggesting that the lateral growth of grains is limited during the initial stages of nucleation.⁸ This observation has been attributed to the high density of nuclei present at the surface due to the higher process pressure. The high deposition pressures result in non-preferential grain growth and grain crowding. The opposite is observed for tensile films grown at lower pressures.

For most film-substrate combinations, with a high growth flux and moderate homologous temperature (T_{sub}/T_{melt}) polycrystalline films are grown by the Volmer-Weber (VW) mode.² The adatoms form clusters on the substrate which increase in size until they impinge on adjacent clusters to ultimately form a continuous film. Stress changes in the polycrystalline film correlate with the sequential steps in the film growth process.

The initial compressive film stress observed in the growth of many polycrystalline thin films corresponds to the early stage of island growth. During the island growth process, the crystallites forming on the growth surface become “attached” to the substrate such that upon further growth of the islands an internal elastic strain is generated. Normally this strain would relax as the radius of the island increased but due to the constraint of the substrate this internal relaxation does not occur.² As a result of the increasing strain due to the increase in the size of island a volume-averaged compressive stress results in the individual crystallites. A second contributing factor is the importance of the density of the islands present on the

¹ Miller, Gregory K, and Ralph G Bennett. "Analytical solution for stresses in TRISO-coated particles." *Journal of Nuclear Materials* 206.1 (1993): 35-49.

growth surface. The stress field of an isolated island has no resultant force on the substrate and the magnitude of the field tails off within a short distance from the island. For a distribution of islands to result in a non-negligible stress field, the density of the islands must be such that the fields of the islands interact.²

This small overall compressive film stress is active until the islands establish large area contiguity or island-to-island coalescence across the substrate. As mentioned previously, this stage of the growth process as adatoms continue to impinge on the islands and as a result the surface area of the islands expand until they begin to merge together. During this process the volume-averaged film stress becomes highly tensile. The most widely accepted explanation of this compressive to tensile transition during the initial stages of polycrystalline film growth is based on work performed by Hoffman and Doljack and later by Nix.^{2,12} They hypothesized that the small gaps between impinging islands can be closed by forming grain boundaries. As the islands begin to make contact they still have a relatively high surface area and therefore a high surface energy. As the islands continue to coalesce and the grain boundary is formed, the decrease in the surface area and therefore the high surface energy is replaced by the relatively low interfacial energy of the grain boundary. In lowering the net total energy of the system of islands and the corresponding reduction in surface area of the film, the participating islands become elastically strained with a tensile state.² The critical island size at which coalescence occurs is generally influenced by a combination of process parameters such as the growth flux (function of pressure), substrate temperature, and surface diffusivity of the impinging adatoms.²

The final evolution in the stress behavior shown in Figure 1.1.3 occurs with continued film growth and is represented by a transition from tensile to a steady-state compressive stress state for a fixed growth flux and substrate temperature.² The compressive stress that arises in polycrystalline films has been attributed to the excess number of atoms in the film due to the deposition flux and the presence of grain boundaries.^{2,13} The supersaturated distribution of adatoms on the growing film provided by the growth flux have free energies greater than the surface atoms of the growing film, which have free energies higher than atoms in the interior of the film. The free energy of the surface atoms may not be sufficient to drive the incoming adatoms into interstitial sites in the lattice, but the surface atoms can lower their free energies by migrating into the grain boundaries.² This incorporation of excess atoms into the grain boundaries results in a compressive stress in the film. In addition the driving force for adding additional atoms into the grain boundaries decreases with increasing magnitude of the compressive stress, which leads to the steady-state value observed in the experimental data shown in Figure 3.3.

The high tensile stress states at lower process pressures can potentially be explained by the reduction of grain boundary area and corresponding grain growth. This coincides with the larger grain sizes observed in the 3C SiC films. This effect is a result of the fact that the material inside the grain boundaries is less dense than inside the grain due to the relative atomic disorder inside the grain boundaries. Therefore a reduction in the grain boundary area leads to a densification of the film and tensile stresses in it.² An energy per unit area is associated with each grain boundary surface which is representative of the amount of excess energy of the grain boundary above that of the lattice structure within the grains.² This excess energy can be reduced by decreasing the total area of the grain boundary surface, which is equivalent to a reduction of the net length of the grain boundary surface as measured parallel to the film-substrate interface. For a representative material sample with several interior grain boundaries, the material

undergoes a stress-free isotropic contractive strain when the grain boundary surface area is reduced.² However, since the material is constrained against normal displacement due to the surrounding bulk material an elastic extensional strain is induced. This elastic strain corresponds to an elastic energy which increases parabolically with increasing grain boundary area reduction.² The degree with which the elastic energy changes with respect to grain boundary area reduction is based on the amount and nature of the initial stress state of the material.² If it is assumed that an initial compressive stress state exists, then the critical grain size at which the free energy of the system is at a minimum increases, thereby promoting a greater degree of grain growth and a larger resulting tensile stress.²

It has been observed that the columnar grains present in the 3C SiC films exhibit highly textured (111) orientation observed by transmission electron microscopy (TEM) and X-ray diffraction (XRD) analysis. Columnar grains are formed if one crystal orientation is preferred during film growth. The initial distribution of grain orientations is random, but those grains with their preferred growth orientation parallel to the film normal dominate over the inclined grains during growth competition. Once the columnar microstructure has evolved, adatoms can immediately add to the fast-growing crystalline planes without inducing any compression. The preferred crystal orientations with the fastest growth rates are the {111} directions as is evident by the highly textured <111> grain orientation. As a consequence of the preferred growth direction, any new incoming adatom may deposit itself in the grain boundary region between two grains. Even though this will cause an increase in the strain energy, it may be the lowest overall energy state for the adatom.¹⁴ The crystallinity of the 3C SiC films does not exhibit a large difference when analyzed at different residual stress conditions. Glancing incident angle XRD (GIXRD) scans made of the high compressive stress sample were taken. By changing the tilt angle, ω , with respect to the exact 2θ angle location of the characteristic (111) 3C peak the primary silicon peak and reflection peaks which tends to obscure lower intensity SiC peaks can be eliminated. GIXRD essentially tilts the sample stage such that the x-rays interact with the thin-film only. Such scans were performed on a variety of stress states in collaboration with colleagues at the University of Tennessee-Knoxville in order to determine critical irradiation dose which is discussed later in this report. The following TEM images, shown in Figure 1.1.4, exhibit the qualitative observation mentioned above showing that the films grown at higher pressures exhibit smaller grain widths than those films grown at lower pressures.

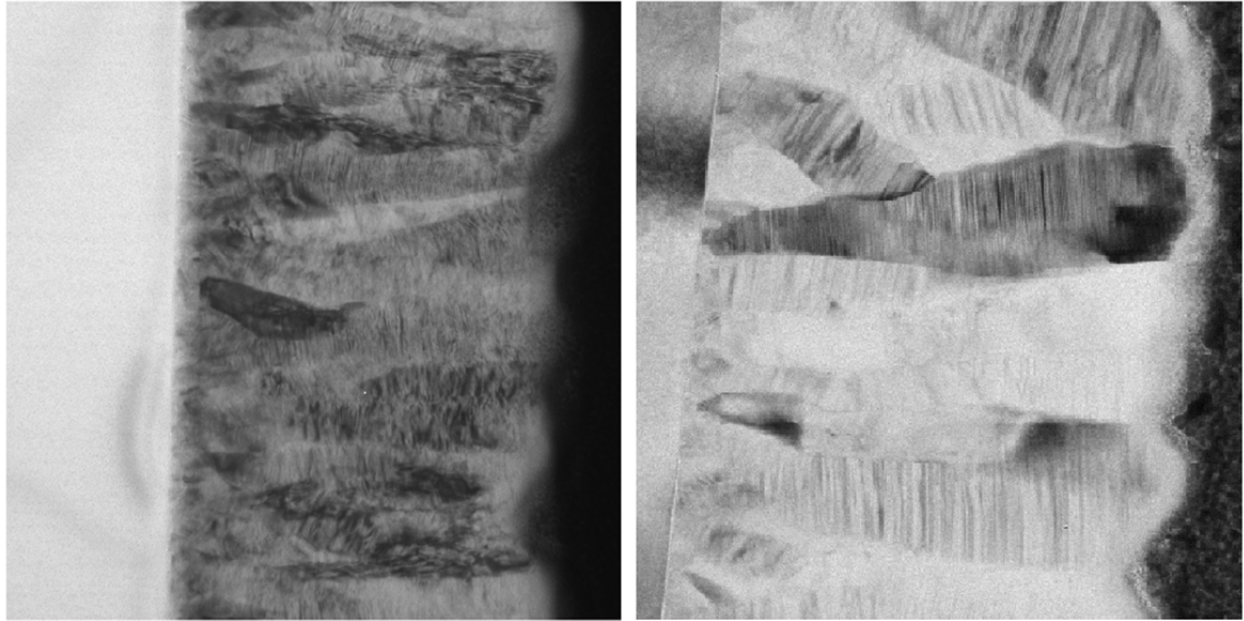


Figure 1.1.4: TEM images depicting smaller lateral growth of grain boundaries and higher degree of uniform orientation of left image (highly compressive film) compared to the right image (highly tensile film).

In order to characterize the change in the residual stress-strain characteristics of the varied stressed 3C SiC films due to the onset of radiation-induced lattice damage it was necessary to develop a platform which provided a means to quantify changes in the stress characteristics and in the crystallinity and microstructure of the film. This was achieved by using arrays of dies containing adjacent microcantilevers and open areas of 3C SiC which were utilized for focused ion beam (FIB) material removal for transmission electron microscopy (TEM) and XRD. TEM and XRD were used to analyze the microstructure of the film which is discussed below.

The polycrystalline 3C SiC films grown experimentally contain large densities of stacking faults (SFs) within the individual grains. Stacking faults are defects in which the proper order of stacking planes is interrupted by the addition of an extra plane due to misoriented islands in the LPCVD growth.⁶ These errors in stacking sequences occur along the (111) and are the result of the island growth method common to heteroepitaxy.¹⁰ The formation of these SFs is believed to be dominated by atomic deposition errors on the {111} planes of individual crystallites and mismatches of lattice sites during the coalescence of islands during film growth.¹⁰ It has been proposed that these SFs attribute to higher radiation tolerance observed in the nanocrystalline SiC.¹⁵ In order to attempt to control the SF density, the carbonization pressure was changed with respect to the main growth pressure. This idea was based on previous research conducted on single-crystal epitaxial growth of 3C SiC conducted by A. Severino, et al. where the pressure difference between carbonization processes using LPCVD and APCVD systems was investigated. Although the temperatures they used were much higher than 900°C, controlling the growth pressure of the initial carbon seed layer seemed to be a logical first attempt. Shown below in Table 3.1 are the run conditions used in these initial test runs.

Table 1.1.1 - Summary of growth pressures for LPCVD runs to control SF densities

<i>Experiment #</i>	<i>Carbonization Pressure (mTorr)</i>	<i>Main Growth Pressure (mTorr)</i>
1	231	264
2	418	434
3	330	330
4	248	444
5	434	225

The two runs investigated using high-resolution TEM are samples from the last two entries in Table 3.1. The approximate SF densities were determined to range from 0.058-0.288 nm⁻² for the run where the carbonization pressure was 248 mT compared to the growth pressure of 444 mT and 0.3891-0.6159 nm⁻² for the carbonization pressure of 434 mT compared to the growth pressure of 225 mT. Shown below in Figure 3.8 are high-resolution TEM images of the samples used to estimate the SF densities.

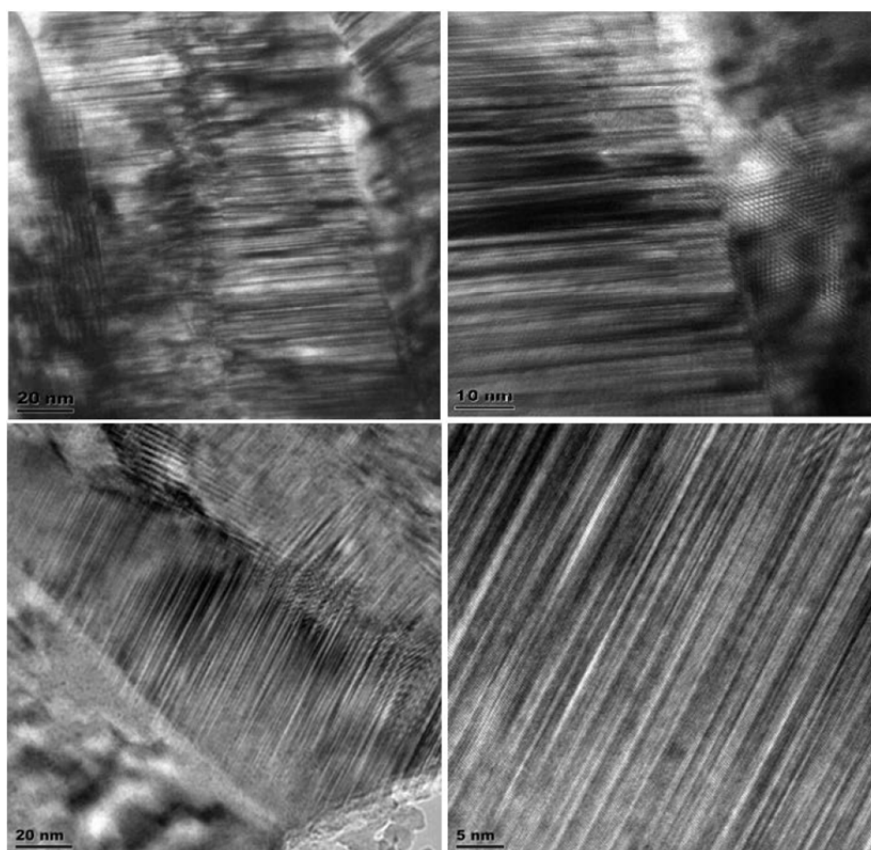


Figure 1.1.5: High-resolution TEM images of samples from experiments 4 and 5, discussed above, illustrating the difference in microstructure. (Top) Images correspond to 248 mT carbonization/444 mT growth; (Bottom) images correspond to 434 mT carbonization/225 mT growth.

Task 2: First principles simulation of irradiation effects in refractory materials

2.1: Dynamical recovery in uranium oxide following radiation impact

In the current investigation we elucidate the dynamical response following a radiation impact in UO_2 using MD simulations. Our main objective is to characterize the short-time dynamical behavior through time-resolved correlation functions that are potentially accessible, with appropriate convolutions, from ultrafast pump-probe experiments.¹⁶ Our results show that the oxygen ions show a collective behavior that enables a quick relapse, following radiation, to the native dynamics that is characterized by concerted oxygen ion jumps across lattice sites. In comparison, we also show that silicon, which is easily amorphized, portrays a distinct heterogeneous dynamics involving spatially separated groups of more mobile and less mobile atoms.

We have simulated UO_2 with a rigid-ion interionic potential that has been benchmarked to a spectrum of properties with reasonable accuracy.^{17,18} While polarization effects are important in the simulation of superionic materials, rigid-ion potentials can be made to reproduce the static and dynamic properties with reasonable fidelity by tuning the dispersion term in the interionic potential.¹⁹ In our work²⁰, we have shown that all type II superionic conductors including UO_2 show a well defined onset of dynamic disorder at which collective dynamics such as dynamical heterogeneity starts to manifest among the anions. Above the temperature corresponding to this onset ($T_\alpha \approx 2000$ K) the oxygen ions in UO_2 become more disordered and participate in a complex cooperative diffusional hopping process between the lattice sites. Thus we have established that oxygen ions in the equilibrium state of UO_2 have a natural tendency to be dynamically disordered through thermal fluctuations beyond the superionic onset temperature T_α without the formation of permanent defects. At the Bredig or superionic transition ($T_\lambda \approx 2650$ K), the oxygen ions undergo a second order phase transition accompanied by a sharp increase in the specific heat and a structural transformation to a liquid-like state; complete thermodynamic melting occurs at 3140 K. While the Bredig or premelting temperature (T_λ) is well established, the existence of a well-characterized disorder onset temperature (T_α) is relatively new.²⁰

Radiation cascade simulations are conducted in a cubic box that contain 64,000 oxygen and 32,000 uranium ions with a total of 96,000 ions. In addition to the rigid ion potential, we have employed a screened Coulombic (ZBL) repulsive potential at separation distances shorter than 1.0 Å. We start the simulation by placing the ions in the equilibrium lattice positions and assigning velocities drawn from a Maxwellian distribution centered at 300 K, followed by an equilibration period of 20 ps at zero pressure. The displacement cascade is then initiated by imparting a momentum corresponding to the excess energy of the PKA (primary knock-on atom/ion), which is a uranium ion located at the center of the simulation box, along the [100] direction. Temperature and pressure increase following the radiation impact contributing to the rapid increase of the transient defects. A thin atomic sized layer of 10 Å at the system boundaries absorb the excess energy and momentum, and keep the boundaries at 300 K and zero pressure. To acquire statistically significant data, a total of 60 independent runs have been performed, all with the same initial configuration of the atoms but with different initial velocities drawn from a Maxwellian distribution centered at 300 K. Such an iso-configurational ensemble also allows determination of statistical properties of uniquely identified atoms such as the PKA.

Two sets of displacement cascades are analyzed; one with a PKA energy of 1 keV and the other with 2 keV, both along the [100] direction. First, we delineate the short time dynamics of the PKA (uranium ion) averaged over 60 isoconfigurational runs in Figure 2.1.1.

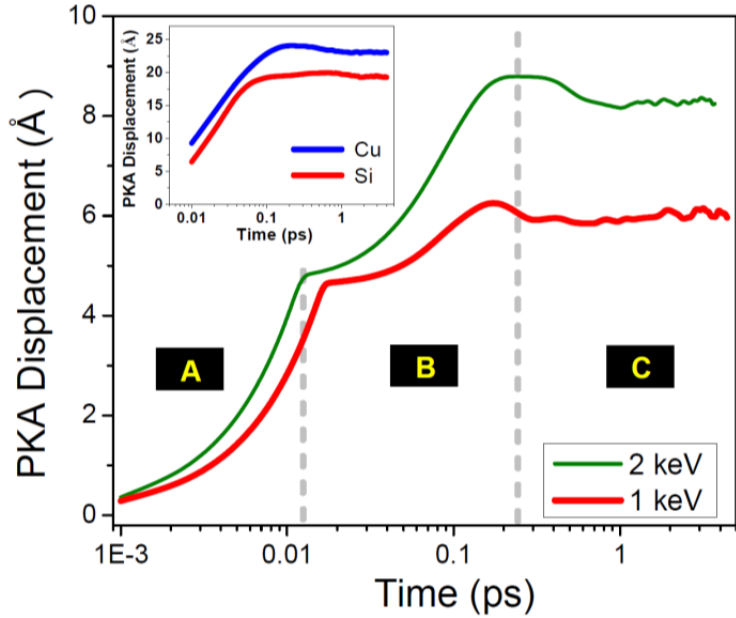


Figure 2.1.1: Time variation of the average (uranium) PKA displacement for cascades initiated with an energy of 1 keV and 2 keV. (Inset) Average PKA displacements in copper and silicon with a PKA energy of 3 keV. A three stage behavior, although not identical, is also observed with an oxygen ion PKA (results not shown).

In general, the PKA displacement shows three stages; in the first stage (A), the displacement rapidly increases linearly with time. A slope change is detected at approximately 0.01 ps when the knocked uranium ion has traveled an average distance of ~ 5 Å, which is remarkably close to the lattice parameter of the UO_2 cell. Thus the significant deceleration that is observed at the end of Stage A is attributed to an opposing force from the nearest uranium ion. In the second stage (B), the knocked uranium ion travels linearly with time, followed by the last stage (C) where the PKA loses all its excess energy and is brought to rest.

The dynamic behavior of the knocked ion is vividly different from that in metals such as copper or silicon as shown in the inset of Figure 2.1. The PKA displacement has only two stages; in the first, the PKA moves logarithmically with time followed by an abrupt cessation of motion in the second stage. We have attributed this unusual scaling to correlated serial constraints that result in a hierarchical cage being built ahead of the PKA with the faster atoms around the PKA controlling the response of the slower atoms.²¹ In stark contrast such a hierarchical cage appears to be absent in UO_2 ; the PKA motion is primarily determined by the nearest ion of the same charge. We analyze the time resolved van Hove self-correlation function to uncover plausible dynamical mechanisms that lead to a radiation tolerant behavior in UO_2 .

The self-part of the van Hove correlation function $G_s(\mathbf{r}, t)$ gives the conditional probability of finding an ion in an infinitesimal volume of $d^3\mathbf{r}$ around \mathbf{r} at time t , given that it occupied the origin at time $t = 0$. At equilibrium, $G_s(\mathbf{r}, t)$ displays a Gaussian form. Following a radiation impact, as shown in Figure 2, $G_s(\mathbf{r}, t)$

assumes a more complex profile, especially for the tail region. It is particularly interesting to note that $G_s(\mathbf{r},t)$ develops a tail that displays prominent peaks at long times. The peak positions remarkably correspond to the nearest neighbor locations of the oxygen ions in the equilibrium state. Since the peaks denote a diffusional hopping process,²² we conclude that at long times, oxygen ions engage in discrete jumps from one lattice site to another.

Our equilibrium simulations indicate that hopping motion typically involves two or more oxygen ions in a semi-correlated fashion moving from one native site to another, through interstitial/vacancy-like formation and annihilation. A typical ‘hop’ is initiated by an oxygen ion getting thermally displaced to an interstitial location followed by a diffusional jump from a neighboring oxygen ion annihilating the vacancy that was briefly generated by the original oxygen ion.²⁰ Thus the peaks in $G_s(\mathbf{r},t)$ demonstrate that the system dynamics, after the perturbation from the radiation, reverts back to that of the equilibrium state within a short period of time. In contrast, Si portrays an exponential tail (see inset in Fig. 2) that arises from the presence of groups of more mobile and less mobile atoms, which is typical of glassy states.²³ Such a prominent dynamical heterogeneity is conspicuously absent in UO_2 following radiation. From a dynamical viewpoint, we thus attribute the radiation tolerant behavior in UO_2 to the realization of the native equilibrium dynamics in a short period of time following radiation.

2.2: Cooperative motion of oxygen ions and its impact on radiation tolerance of UO_2

We have applied Molecular Dynamics (MD) simulations using empirical potentials to study the kinetic evolution of irradiation-induced point defects in UO_2 . Simulation techniques at the atomic scale can help to unravel the complex processes occurring in materials under extreme conditions. In particular, MD is an excellent tool to probe the microscopic evolution of system following irradiation and has been applied in the study of varying degrees of imperfections such as point defects, defect clusters, dislocations, voids and grain boundaries.^{24,25,26,27} Previous MD simulations of displacive radiation cascades in UO_2 have been devoted mainly to quantifying both simple and complex defect structures. These include the first study of single atomic displacement cascades by Van Brutzel *et al.* on the cascade morphology as well as assessing point defects and defect clusters.²⁸ A subsequent study examined the overlap of 5 keV cascades and revealed the damaged UO_2 matrix to consist of large vacancy clusters and smaller interstitial clusters.²⁹ Later, Devanathan *et al.* examined five different interatomic potentials and found a drastic quantitative variation in point defects as well as vacancy and interstitial clusters, even though all potentials correctly predicted the effective annealing of the system after irradiation.³⁰ More recently, Taller and Bai have studied nine different interatomic potentials applied to different cluster configurations and showed that for identical initial oxygen interstitial clusters, the relaxed cluster structures and their stabilities are vastly different whereas for defect structures containing both uranium and oxygen defects, the predictions are in good agreement.³¹ Here, we also begin with first quantifying the point defects evolution in UO_2 although, the later, more important, part focuses on a distinct, hitherto unconsidered, concerted motion of oxygen ions as the system progresses to annihilate the defects.

The primary input for any empirical MD simulation is the interatomic potential that describes interaction between the atoms. Owing to its importance as the most widely used nuclear fuel, a number of empirical potentials have already been developed to model UO_2 and many of these have been compared in some recent works involving equilibrium and non-equilibrium simulations.^{30,31,32,33} In this study, the short-range

interactions are described using the Busing-Ida type potential form³⁴, with parameters taken from Yakub *et al.*^{35,36} The potential has already been benchmarked to a spectrum of properties with reasonable accuracy. Apart from the widely implemented Buckingham-type form for ionic materials, the Busing-Ida form also contains Morse term that introduces a “covalent” component, applicable only for anion-cation pairs. Also, to take into account the partial charge transfer between the ions, the ions have fractional (non-formal) effective charges, which are the product of their “formal” charge and a defined ionicity parameter, $\zeta < 1$.³⁵ In all the simulations, the long-range Coulomb interactions are calculated using the Wolf direction-summation method³⁷, which we have benchmarked to the standard Ewald method. In the Wolf method, both the Coulombic energies and forces are truncated at a fixed cutoff radius with charge compensation on the surface of the truncation sphere. Also, periodic boundary conditions (PBC) are applied along all three dimensions. In order to integrate Newton’s equation of motion, leapfrog method has been applied³⁸ with an MD time step of 1 fs.

The ions are arranged on crystalline fluorite structure and each ion is assigned an initial velocity based on a Maxwell-Boltzmann distribution centered at 300 K. Next, the system is allowed to attain equilibrium by maintaining the simulation cell at 300 K for a few picoseconds. We then followed the conventional approach of initiating radiation damage in MD simulations by imparting the necessary energy to an atom, which is known as primary knock-on atom (PKA). The high-energy PKA creates a cascade of secondary displacements of atoms from their crystal lattice positions. This initial period of cascade defect formation is known as the *ballistic* phase. The Frenkel-pair, a combination of a displaced atom settling within the interstices of the lattice along with a vacant lattice site, is the most dominant defect type in displacive radiation conditions. The total number of defects in the system reaches a peak by the end of ballistic phase. Subsequently, kinetic evolution of defects results in lowering the number of total defects; this lowering stems from the migration of both vacancies and interstitials towards each other.

All the simulations are carried out on a cubic UO_2 single crystal containing 96,000 ions and run for little above 6 ps after the initiation of knock. A uranium PKA is generated with energy 2 keV and directed along one of the crystallographic axis. The system size is sufficient to hold the displacement cascade within its bounds, thereby avoiding any self-interaction that might have been possible with the applied PBC. We have only considered one cascade of displacement per simulation, without any overlaps. Since the objective of this work is to study the kinetically-evolving nature of defects following a collision cascade, we believe the energy imparted is sufficient enough to generate reasonable number of defects. Also, the initial direction assigned to PKA is of no consequence, as it has been shown that in UO_2 that the initial PKA direction has little effect on the final defect evolution.²⁸ To identify the defects, we compare configuration of the evolving system with the initial zero defect structure. A lattice site is considered a vacancy if it does not contain an atom within a sphere of radius 1 Å centered on the site. Similarly, an atom is considered an interstitial if it is inside a similar sphere centered on an interstitial site. An inevitable consequence of displacement cascade simulations is the close approaching of atoms that are interacting primarily by Coulombic forces. The “universal” ZBL potential³⁹, a screened Coulombic repulsion between nuclei, is applied for distances less than 1 Å and this potential is joined smoothly by a Fermi function to the pair-potential described earlier. A total of 130 independent runs are performed, deemed sufficient for good statistics, and all the results are averaged over the independent runs. It has been shown recently that the irradiation spectrum plays a very important role in determining the radiation tolerance of some pyrochlores, a close variant of fluorite-structured oxides, and demonstrated the titanate

(Ti) pyrochlores as characterized by either poor radiation tolerance or robust behavior depending on the energy of the PKA [26]. Keeping this in mind and seeking to examine our results at higher PKA energies, we have done additional 10 keV displacement cascade simulations on a $24 \times 24 \times 24$ system of UO_2 having 165,888 ions. A total of 80 independent runs are performed in this case. The results obtained, as will be shown, are in very good agreement with the 2 keV results.

In Fig. 2.2.1, we show the time variation of the number of point defects, arising due to displacement cascade, for both uranium and oxygen ions. An ion is considered a defect if it does not belong to any lattice site within a specified cut-off distance (given earlier); anti-site defects are also considered. The well-known, two-stage behavior of cascade defect evolution can be seen with the number of defects peaking initially and the recovery stage taking over afterwards. The inherent stability of UO_2 structure with a high rate of instantaneous defect recovery is quite evident; the residual number of defects after just a few picoseconds is a small fraction of the number of defects at the end of ballistic stage. Also, no anti-site defects were observed by the end of our simulations.

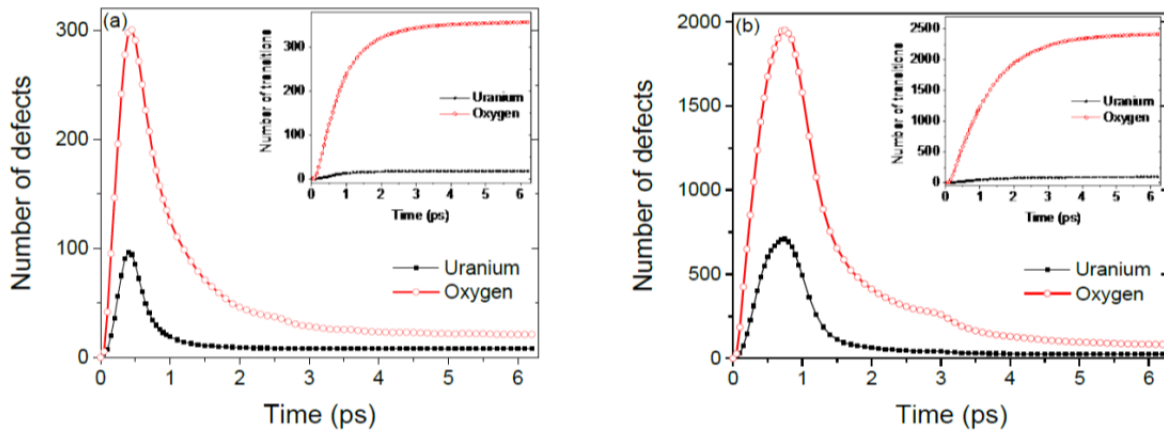


Figure 2.2.1 - (a) Time variation of number of defects during the evolution of 2 keV displacement cascade, initiated at $t = 0$, in UO_2 . The number of defects peak around 0.5 ps and starts to fall afterwards. Inset shows the plot of number of replacement transitions by uranium and oxygen ions to identical neighboring sites. The massive uranium ions are only slightly perturbed by the displacement cascade and mostly return to their original positions. By contrast, several displaced oxygen ions perform replacement jumps to get annealed. (b) Similar plots for 10 keV displacement cascade. In this case, the defects peak around 0.75 ps before the system starts to anneal. All the results are qualitatively similar to the 2 keV case.

In the case of uranium ions, the rise and fall in the number of defects is mainly attributed to a number of ions initially displaced due to the cascade, thereby becoming interstitials, and later reverting to their original sites. Very few uranium defects jump to a new cation site to get annihilated. The situation is completely different for oxygen ions. A significant number of anion defects are annihilated by means of making transitions to new lattice sites. This is evident from the inset of Fig. 2.2.1, which shows the number of replacement transitions made by both uranium and oxygen ions. Since the uranium ions are mostly immobile, as very few of them made a transition from their original sites, in the rest of this work, we concentrate only on the motion of oxygen ions, the mobile species, and ignore the uranium ions. The oxygen ions that have made transitions mostly jump to nearest neighbor or second nearest neighbor positions (i.e. along $\langle 1\ 0\ 0 \rangle$ and $\langle 1\ 1\ 0 \rangle$, respectively). This can be substantiated by means of a van Hove self-correlation function as described in section 2.1. The van Hove self-correlation function measures the

probability that a particle has displaced a distance r during a time-interval t (defined as $4\pi r^2 G_s(r,t)$), and behaves as a Gaussian under equilibrium conditions. Following radiation knock however, $G_s(r,t)$ assumes a more complex profile, as shown in Fig. 2.2.2. It is particularly interesting to note that $G_s(r,t)$ develops a tail that displays prominent peaks at longer times. The peak positions remarkably correspond to the nearest neighbor locations of the oxygen ions in the equilibrium state. Since the peaks denote a diffusional hopping process [28], we conclude that at longer times, oxygen defects annihilate by engaging in *collective* jumps to neighboring sites.

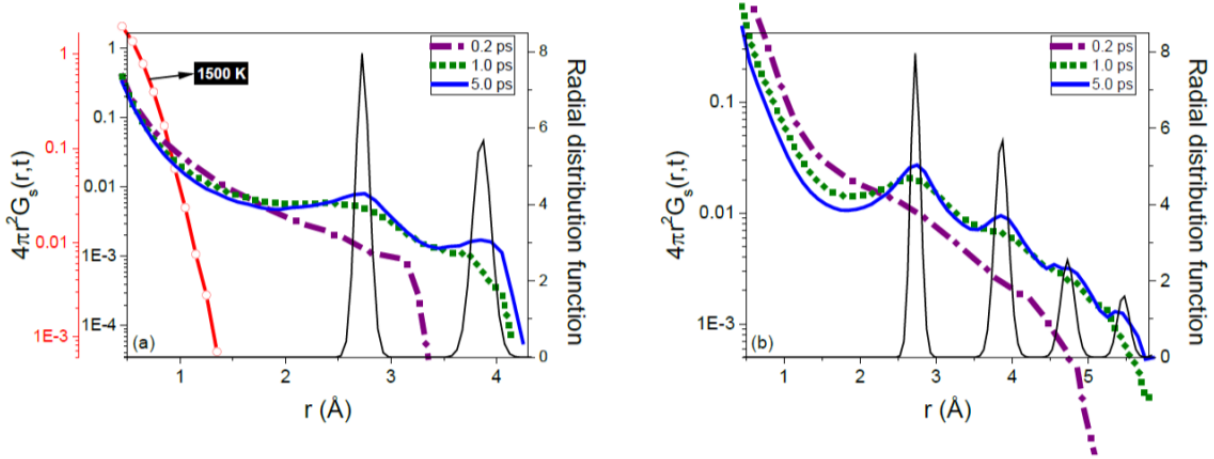


Figure 2.2.2 - (a) Time resolved van Hove self-correlation function for oxygen ions at different times following radiation impact, with a knock energy of 2 keV. The radial distribution function (RDF) of oxygen ions at 300 K is also shown (the two peaks in RDF correspond to the nearest $\langle 1\ 0\ 0 \rangle$ and $\langle 1\ 1\ 0 \rangle$ distances), and the peaks in the tail of $G_s(r,t)$ matches very well with the nearest neighbor positions from RDF. For comparison, $G_s(r,t)$ for oxygen ions in equilibrium simulation at 1500 K is also shown, exhibiting a simple Gaussian-type decay. (b) $G_s(r,t)$ for the case of 10 keV displacement cascade. The oxygen ions are displaced much farther in this case. Here also, the peaks in $G_s(r,t)$ match very well with that from the RDF.

The peaks in the tail of $G_s(r,t)$ indicate that displaced oxygen ions recover by means of hopping to neighboring sites. Here, we introduce string-like cooperative motion, which involves *simultaneous* jumps of more than one ion to neighboring lattice sites, each ion supplanting the next ion in the string during the motion, culminating with the last ion jumping into a vacant site or into a site by pushing the existing ion into an interstitial position (hence, no further simultaneous transition is possible from this site to a neighboring lattice position). This type of motion has been observed in our simulations and, as will be shown later, plays an important role in the fast annihilation of oxygen defects. Fig. 3 illustrates an example of string-like motion in a two-dimensional system.

Fig. 2.2.3 shows three ions performing string-like correlated motion in which every ion replaces the next ion in the string. The jump of the ions could be in any direction in three-dimensional space during the simulations. An ion making a transition between two lattice sites, say, a' to a'' , could be staying in an interstitial position for any amount of time after leaving a' and before entering a'' . However, all transitions to new sites must occur at the same time to be considered as a string-like cooperative motion. In this work, we have surveyed for any presence of strings at 0.05 ps intervals during the first pico-second after the PKA knock and then at every 0.1 ps intervals for the rest of the simulation; if the first ion transition in Fig. 2.2.3 to B, second ion to C, and third ion to D occur during the same time interval, we have a string-

like cooperative motion. This kind of motion can complement the well-known vacancy-interstitial recombination and helps in the recovery of defects.

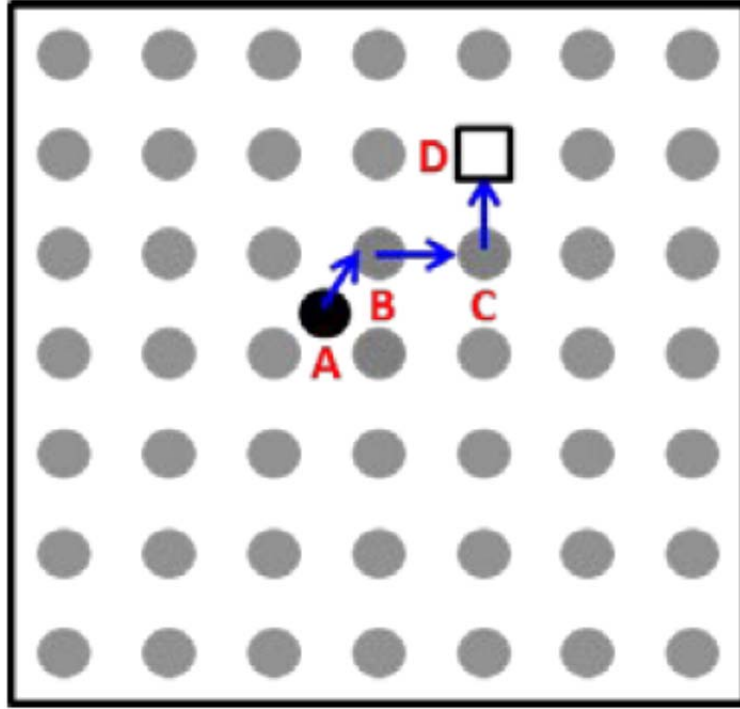


Figure 2.2.3 - A sample 2-dimensional system with an interstitial and a vacancy. A is an interstitial position while B, C and D are lattice sites. The atoms at A, B and C make cooperative jumps and, after the transition, will be at B, C and D, respectively.

As mentioned already, Frenkel-pair is the dominant defect type during irradiation. The Frenkel-pairs usually get annihilated by means of simple vacancy-interstitial recombination. In this process, a vacancy has to migrate to a site adjoining an interstitial or/and an interstitial jumps towards a vacancy thereby both getting annihilated eventually. The whole process involves several independent steps, if the initial vacancy and interstitial are well-separated. However, during string-like motion, an ion jumps not only into a vacant neighboring site but also into an occupied one by inducing the ion on the latter site to make a jump to a neighboring lattice site. Performed this way, an interstitial can recombine with a vacancy several steps away much faster (lesser number of steps) by means of cooperative jumps than would be possible by simple vacancy-interstitial recombination.

For our later results, we now define the lifetime of any ion involved in a transition. As noted earlier, an ion belongs to a lattice site if it is inside a sphere of radius 1 \AA centered on the site. For the ion in Fig. 2.2.3 making a transition between lattice sites B and C (from B to C), if t_1 is the most recent time the ion belonged to B and t_2 is the time when it first belongs to C, the lifetime of ion involved in this transition is $(t_2 - t_1)$. The lifetime directly indicates the amount of time an ion has spent in interstices of the lattice before making a transition, with longer lifetime corresponding to longer stay at an interstitial site (as a defect).

We define the length of the string (n) as the number of ions involved in cooperative motion; e.g. the string in Fig. 2.2.3 has $n = 3$. In our simulations, most of the strings (approximately, 90%) correspond to $n = 2$ while strings involving as many as 6 ions have been observed. The probability distribution of the length of string, $P(n)$, is shown in Fig. 2.2.4(a) and 2.2.4 (b) for 2 keV and 10 keV simulations, respectively. The behavior is evidently exponential, in both the cases.

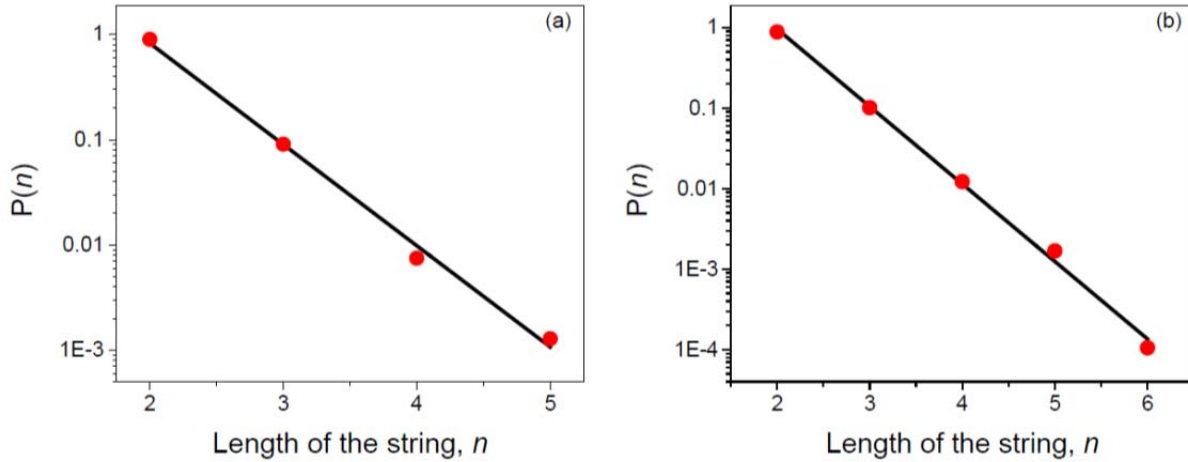


Figure 2.2.4 - Probability distribution of length of the strings observed during (a) 2 keV and (b) 10 keV cascade simulations. $P(n)$ evidently follows an exponential distribution.

In Fig. 2.2.3, we refer to the first ion making a transition from A to B as the “initiator” of string. Even though every string has two ions at its edges (for $n = 2$, both ions involved are at the edges), only the *initiator* ion replaces next ion in the string during cooperative motion. Hence, there is a unique *initiator* ion for any chosen string. We categorize the rest of the ions participating in string motion as *neighbors*. In this work, we contend that string-like cooperative motion is mostly *initiated* by oxygen ions that have long been displaced from their actual positions to interstitial sites, i.e., an *initiator* ion in any particular string has, on average, longer lifetime compared to the *neighbor* ions participating in that concerted motion. To corroborate this, in Fig. 2.2.5, we have plotted the probability histograms of lifetime of all ions, divided into *initiators* and *neighbors*, involved in cooperative motion. The histograms are normalized with the number of ions in their respective groups.

The histograms in Fig. 2.2.5 clearly indicate that *neighbor* ions in the string have preference towards shorter lifetimes while the *initiator* ions have higher probabilities than *neighbor* ions at longer lifetimes. We have evaluated average lifetime for both the groups and the ratio ($ri-n$) of *initiator* group lifetime to that of *neighbor* ions is found out to be 1.92. Hence, *initiator* ions have, on average, almost twice the lifetime compared to *neighbor* ions in the string. This seems to indicate that string-like cooperative motion is mostly initiated by oxygen ions that are relatively long-displaced.

More compelling evidence that *initiator* ions of cooperative motion are long-life defects can be obtained if we only consider cooperative jumps starting from a time subsequent to the ballistic phase; here, we have chosen $t = 0.5$ ps, and, also, $t = 1.0$ ps. In both these cases, all the cooperative jumps that might have been artifacts of cascade initiation and the ensuing ballistic phase will be discarded and only those taking

place during defect recovery phase will be counted. The resulting histograms are shown in Fig. 2.2.6. The propensity for the *neighbor* ions to have shorter lifetimes is more pronounced now, so does the tendency of the *initiator* ions to have longer lifetimes. The ratio of *initiator* group lifetime to that of *neighbor* group lifetime ($ri-n$) is 2.07 and 2.54, for starting times 0.5 ps and 1 ps, respectively. By going towards even higher starting times, we can focus entirely on the fate of long life defects. Table 2.2.1 illustrates $ri-n$ for different starting times. The average lifetime of *initiator* ions is almost seven times compared with that of *neighbor* ions, if we consider a starting time of 3.5 ps. By going towards higher starting times, this ratio increases even further, in agreement with our assertion, although we believe there are not enough instances of cooperative motion to obtain statistically reliable values (we can understand this from Fig.2.2.1 (a) that after $t = 3.5$ ps, the rate of defect annealing for oxygen ions is almost negligible). With the help of Fig. 2.2.5 and Fig. 2.2.6 as well as Table 2.2.1, it is quite clear that cooperative motion is mostly *initiated* by long-displaced oxygen ions as a mode of getting annihilated.

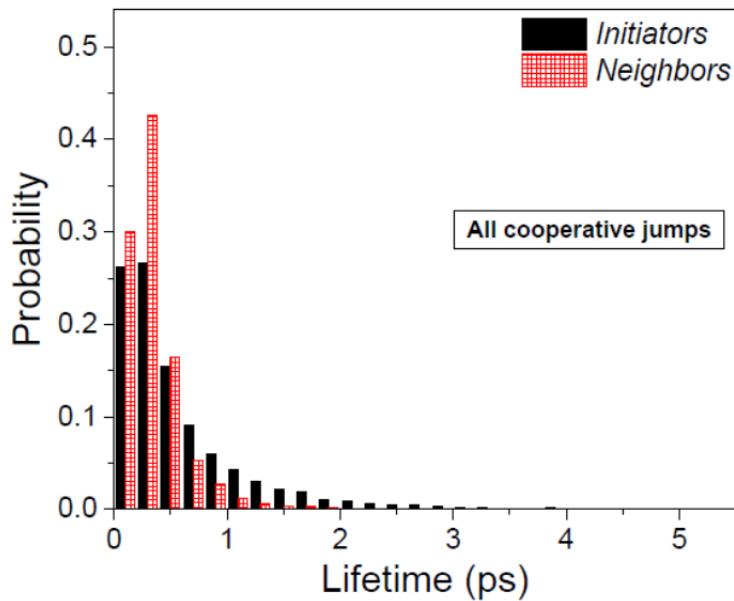


Figure 2.2.5 - Lifetime probability histogram for “initiator” and “neighbor” ions that have participated in string-like correlated motion. Longer lifetimes correspond to long-life defects and vice-versa.

By now, we have verified that long life defects can employ cooperative motion, by mostly becoming *initiator* ions, to get annihilated. But what fraction of defects really undergoes cooperative motion? A tiny fraction would motivate no one. To investigate the importance of string-like cooperative motion, we consider all the annihilated oxygen defects that have made replacement jumps onto neighboring oxygen sites and evaluate the fraction of them initiating a string motion during their recovery. Fig. 2.2.7 shows the results. Several things are worth noting:

1. The probability of an oxygen defect annihilating by means of cooperative motion, competing with vacancy-interstitial recombination, is almost constant, when its lifetime is varied from 0.2 to 2 ps. In this case, the defect could be either *initiator* or *neighbor* in the string.
2. However, the probability of this ion *initiating* a string increases with increase in lifetime of the defect. The probability has increased from 10 to 23 percent by varying the lifetime of the defect.

from 0.2 ps to 2 ps. Hence, longer the time an ion has been in a defective state, the higher the probability that it will annihilate by means of *initiating* a correlated jump.

3. It is equally interesting to note that the probability of the defect being a *neighbor* of the string decreases by increasing the lifetime of the defect (evident from (1) and (2)).

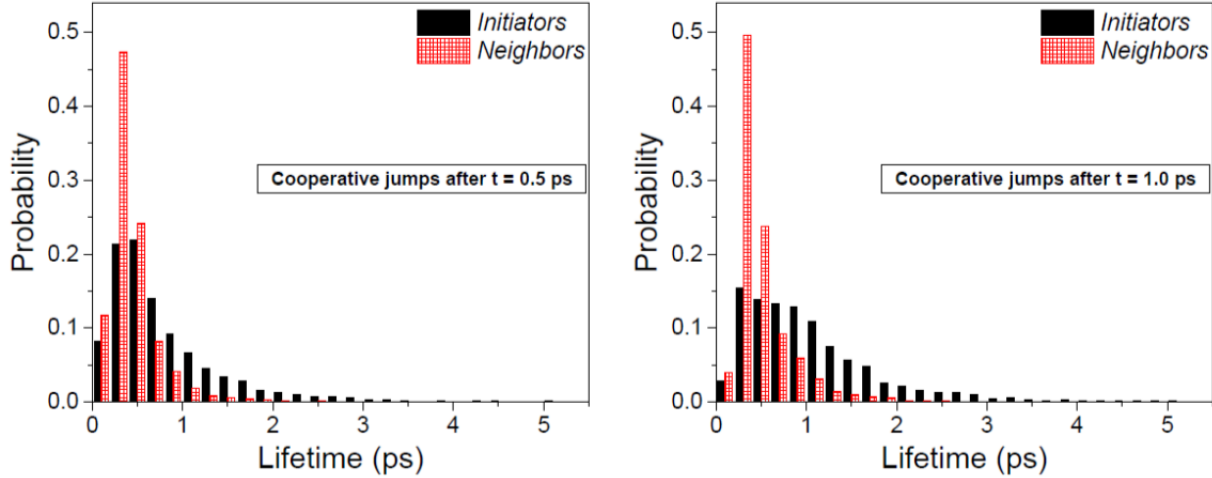


Figure 2.2.6 - Lifetime probability histogram for oxygen ions involved in cooperative jumps that occur with starting times (a) $t = 0.5$ ps and (b) $t = 1.0$ ps. With increasing starting time, the *initiator* ions seem to have higher lifetimes while the *neighbor* ions tend towards shorter lifetimes.

Table 2.2.1 – The pronounced lifetimes of initiator ions, normalized to neighbor ion lifetimes, is shown for various starting times during 2keV cascade simulations

Starting time (ps)	Ratio of initiator group to neighbor group lifetimes
0	1.92
0.5	2.07
1.0	2.54
1.5	3.30
2.0	4.27
2.5	5.07
3.0	5.66
3.5	6.78

From Fig. 2.2.7, it is apparent that string-like correlated motion is an important mode of defect annihilation, especially for long-displaced ions, while the remaining recovery takes place by simple vacancy-interstitial combination. We see qualitatively similar results for 10 keV PKA knock, from Fig. 2.2.7(b). Finally, we seek to confirm all the above results using a different interionic potential. For this purpose, we have simulated UO_2 using Basak potential.⁴⁰

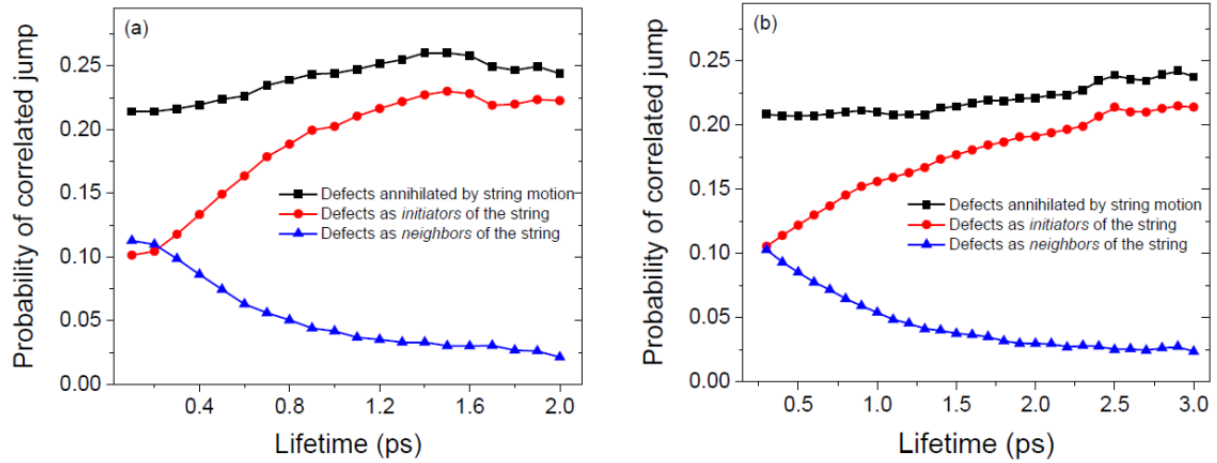


Figure 2.2.7 - Probability of an annihilated defect to have employed cooperative motion for (a) 2 keV and (b) 10 keV atomic displacement cascades.

2.3: The role of CSL Boundaries on Displacement Cascades in β -SiC

Several investigations show that grain boundaries are instrumental in reducing the point defects which are formed during the cascade simulations.^{41,42,43} Thus materials with a large volume fraction of grain boundaries are often considered to be good candidates for resisting radiation induced damage. Recently, Zhang *et al.* have shown that engineered nanocrystalline SiC with a high density of stacking faults promotes efficient recombination of point defects which results in enhanced resistance to amorphization.¹⁵ A computational study by Swaminathan *et al.*⁴⁴ with various tilt grain boundaries in β -SiC, on the other hand, has shown that the damage in the in-grain region is not affected by the grain boundary type and the magnitude of damage is comparable to the damage in single crystals under normalized conditions.

In the current study, we have investigated the interaction of displacement cascades generated by a primary knock-on atom (PKA) with a $\Sigma 9\{122\}[110]$ tilt grain boundary in β -SiC using molecular dynamics (MD). A key thrust is on the investigation of the statistical nature of atom mobility near the interface using an isoconfigurational ensemble.

In principle, there are many possibilities of orientations between two grains. Among the possible orientations, a few of them are regarded as special for which the GB boundary is described as a coincident site lattice (CSL) boundary.⁴⁵ A CSL can be described as a superposition of the two crystals (crystal A and crystal B) rotated around the axis P with a common origin, such that the intersection consists of coincident lattice points – the lattice points which are common to both of the lattices. Generally, a CSL is designated as $\Sigma\{hkl\}[hkl]$ where Σ is defined by the ratio of the unit-cell volume of the CSL to that of the original lattice, $\{hkl\}$ is the mirror plane and the $[hkl]$ is the rotation axis. CSL boundaries are extensively studied as they are frequently found in experiments and they can be handled well with computational techniques. In the present study we have used a p -type $\Sigma 9\{122\}[110]$ tilt grain boundary.

MD simulations are performed using LAMMPS package developed at the Sandia National Laboratories.⁴⁶ The interatomic interactions are described by a Tersoff potential optimized by Devanathan *et al.*⁴⁷ In order to obtain the most stable bicrystal configuration, the energy of the atoms is minimized using a

conjugate gradient (CG) algorithm. The lowest energy configuration, thus obtained, is then equilibrated (for 50 ps) at the desired temperature and zero pressure using a NPT ensemble. For radiation cascade simulations, a primary knock-on atom (PKA) is given additional momentum perpendicular to the grain boundary as indicated in Figure 2. Fixed boundary conditions are applied for the boundaries parallel to the GB plane, while periodic boundary conditions are used in the other directions. In each grain, three distinct regions are defined as shown in Figure 2.3.1. In Region 3, the relative positions of the atoms are kept constant throughout the simulation while in the other two regions, the atoms are free to move. In Region 2, the atoms are coupled to a Nose-Hoover thermostat to absorb the excess thermal energy that is generated by the PKA while the atoms in Region 1 move according to the Newton's laws of motion without any constraints. In this investigation, the PKA (Si atom) is introduced with a 5 keV initial energy in a simulation box consisting approximately 400,000 atoms.

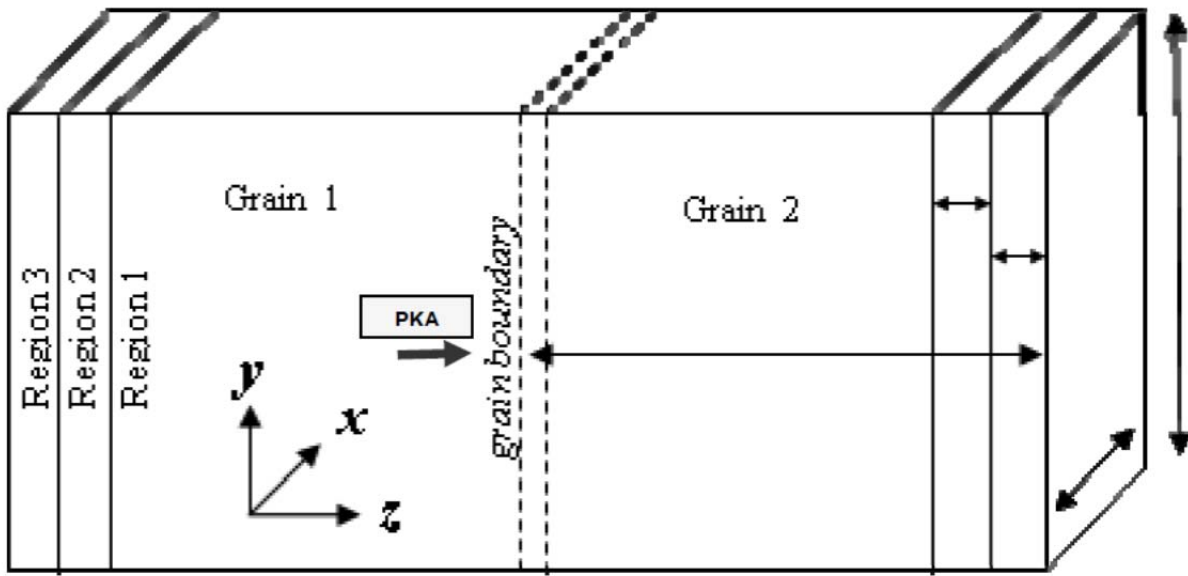


Figure 2.3.1 - Schematic of MD simulation cell for cascade simulations

The number of displaced atoms generated in a displacement cascade for a single crystal is contrasted with that for a bicrystal in Figure 2.3.2. The data is averaged over ten independent cascades in the isoconfigurational ensemble. It is interesting to note that while the number of displaced atoms at the thermal spike in both crystals is approximately the same, the number of displaced atoms which survive at the end of the annealing phase is less for the bi-crystal. This indicates that the bi-crystal promotes more annihilation of the displaced atoms during the annealing phase.

The displacement distribution in the knock direction (averaged over 40 isoconfigurational copies) for the atoms near the GB interface is shown in Figure 2.3.3. Interestingly we observe an average displacement in the negative z direction as time progresses. Since the knock direction is in the $+z$ direction, we can conclude that several displaced atoms near the GB start moving towards the GB at short timescales. This reverse migration stems from the correlated dynamics at the interface and results in more annihilation of the displaced atoms at the GB interface. Note that the displacement distributions shown in Figure 4 are calculated over the atoms located inside a hypothetical cubic box placed at the GB (around 20,000 atoms).

This ensures that the average negative displacement is not due to any contribution from the relatively less displaced atoms, away from the interface.

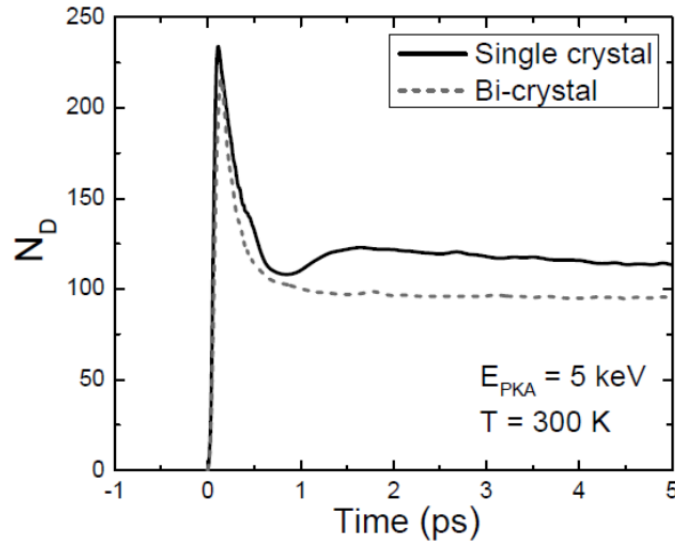


Figure 2.3.2 - Temporal variation of the number of displaced atoms (ND)

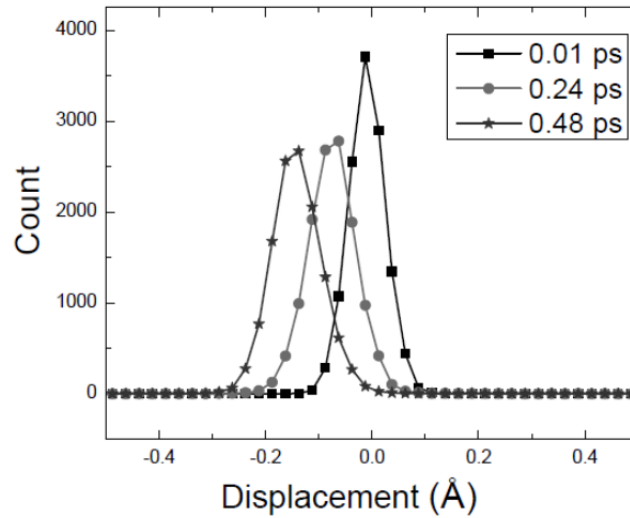


Figure 2.3.3 - Displacement distribution near the GB along the knock (z) direction

2.4: Dynamical heterogeneity and facilitation in superionic conductors including UO_2

In the kinematically constrained models,⁴⁸ it is posited that the DH arises as a consequence of mobile atoms facilitating mobility in the adjacent atoms.^{49,50} It is shown that structural relaxation in glass-forming liquids arises through the dynamics of elementary excitations that are facilitated and hierarchical.⁵¹ The concept of dynamic facilitation (DF) is closely related to DH in that the mobile clusters can be decomposed into smaller dynamical subunits⁵² with spatiotemporal correlations between them, where dynamical events facilitate subsequent dynamics in neighboring particles leading to large-scale DH over time. Hence, DF forecasts that when particles in a microscopic region of space are mobile,

they assist the dynamics of particles in neighboring regions to become mobile, thereby allowing mobility to propagate continuously and in a spatially correlated way throughout the system. DF, in the approach developed by Chandler, Garrahan, and co-workers, plays a key role in the structural response of an arrested state; a jammed region can become unjammed only if it is physically adjacent to a mobile region.⁴⁹ This particularly restrictive condition makes the DF idea unique⁴⁸ and at odds with the spontaneous and random generation of mobile and immobile regions.⁵³ DF is also predicted within the RFOT approach though not as cause but as a consequence of relaxation of the mosaic regions.⁵⁴

2.4.1: Waxing and waning of dynamical heterogeneity in the superionic state

Detecting DH in a superionic state is challenging for two reasons: First, the superionic states are completely in equilibrium enveloped by two well-defined thermodynamic states—liquid and crystal (solid). A supercooled state, in stark contrast, is in a frustrated, nonequilibrium condition, and is bounded by an equilibrium liquid and a nonequilibrium glassy state. Typically, DH is quantified by the generalized four point susceptibility function (χ_4) or through similarmetrics.^{55,56,57,58,59} The theoretical study by Toninelli *et al.* shows that $\chi_4(t)$ can be divided into several time regimes such as ballistic, elastic, early beta relaxation, and so forth.⁵⁶ For supercooled liquids, $\chi_4(t)$ shows a maximum at a time that is $O(\tau\alpha)$, where $\tau\alpha$ is the alpha relaxation time. Further, the magnitude of $\chi_4(t)$ -max shows a monotonic increase with decreasing temperature⁶⁰, illustrating the growing spatial correlations. Conspicuously, $\chi_4(t)$ has an elastic contribution from phonons that increases with time. For perfect crystals, $\chi_4(t)$ grows unbounded without decay, which indicates a general difficulty in differentiating deeply supercooled states from the crystalline states, especially with MD simulations that have limited time windows. In our study, we have used the correlation in the propensity—a metric defined as the mean square displacement of an ion in an isoconfigurational ensemble^{61,62}—and van Hove self-correlation function²³ to uncover the onset of DH.

Figure 2.4.1.1 delineates the main result of our investigation: It shows the progression of the spatial correlation, C_d , based on 100 independent isoconfigurational runs evaluated at $r = 2.6 \text{ \AA}$, which is close to the shortest O-O interionic separation distance. At 1500 K, C_d shows an oscillatory behavior that emanates from the vibratory motion of the oxygen ions; the mean value, however, remains constant for the whole duration of the simulation (500 ps). On increasing the temperature, C_d exhibits two discernible changes: (i) the magnitude of C_d , which represents the strength of the correlation increases, and (ii) the magnitude increases gently and then decreases after passing through a maximum. Unlike in the super cooled states, C_d , however, exhibits a plateau like period before decay. Thus the correlation in the propensity brings out the transition from a crystalline state into a superionic state through an increased correlation strength, and a peaking and decay behavior in C_d that signifies the emergence of dynamical heterogeneity. With increasing temperature, the magnitude of C_d increases with the peaks being exhibited at shorter times—the maximum amplitude can be observed at 2500 K. And on further increase in the temperature, the amplitude of C_d decreases. Figure 2.4.1.2, which shows the variation of the peak magnitude of C_d , depicts the waxing and waning of DH among the oxygen ions. For temperatures 2200 and 1900 K, the peak amplitude of C_d is determined as the mean value during the “plateau” period: 30–80 ps and 200–400 ps for 2200 and 1900 K, respectively. Note that C_d averaged over 1 \AA is somewhat smoother with the peak magnitude observed at approximately 2400 K; similar trend is observed at other radial locations as well. Based on the peak magnitudes of C_d , the maximum DH intensity can be regarded to fall in the temperature range of 2400–2500 K.

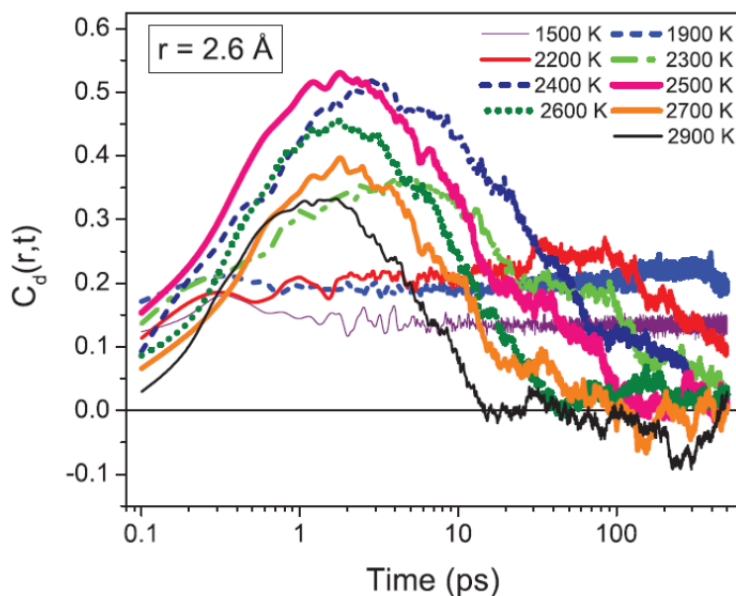


Figure 2.4.1.1 - Spatial correlation (C_d) of the dynamic propensity of oxygen ions evaluated in a restricted, isoconfigurational ensemble for different temperatures.

The temporal behavior of C_d reveals a low temperature (αT) and a high temperature (λT) DH behavior with the former corresponding to the lower temperatures near T_α (1900–2300 K), while the latter corresponds to the higher temperatures near T_λ (2400–2900 K). The αT stage is characterized by deviations from a constant C_d , low correlation strength and a relatively long plateau like period, signifying correlated but hindered ionic motion. The low correlation strength also indicates that only a relatively small number of ions participate in the DH process.

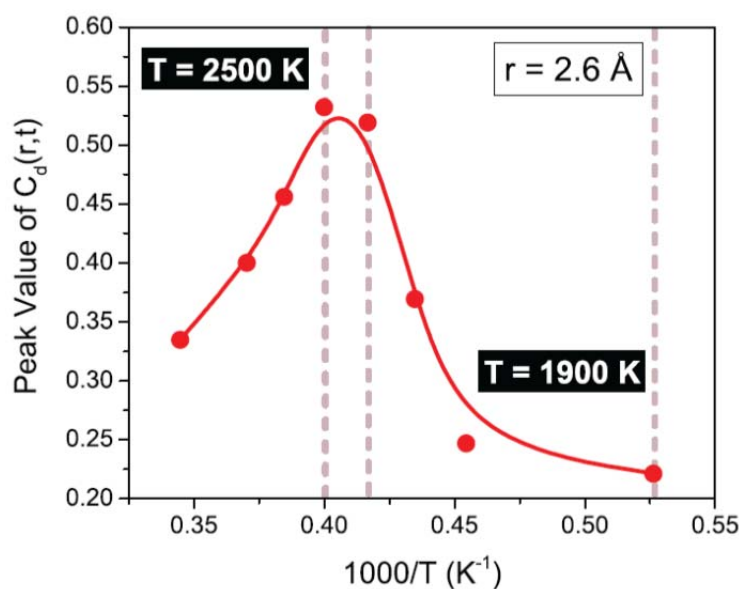


Figure 2.4.1.2 - Waxing and waning of DH among the oxygen ions, illustrated by the variation of the peak amplitude of C_d with temperature.

The α_T DH stage is distinctively different from that observed in typical supercooled liquids—given the preceding crystalline state and the weak growth, it can be characterized as solidlike. While only 500 ps have been simulated for the lower temperatures, we have verified that the system remains in a vibratory state at temperatures lower than T_a . Further, we have used the temperature accelerated dynamics (TAD) of Voter⁶³ to gauge the long-time dynamics—no transitions were accepted for a perfect UO_2 crystal at temperatures lower than T_a , indicating the dominant vibratory motion of the ions without crossing an energy barrier to another state (diffusive motion). In contrast, the high temperature λ_T DH stage is characterized by a significant strength in the correlations and a peaking behavior that is analogous to supercooled liquids. The crossover from the solid like DH behavior to a more Liquid like response (at ~ 2300 K) has a structural origin, which is described in Sec. D of [64].

We will now provide more evidence for the evolution of DH as well as for the crossover from solid like to liquid like behavior of the oxygen ions. The van Hove self-correlation function for oxygen ions—shown in the top panels of Fig. 2.4.1.3 at different temperatures—delineates two striking features: At temperatures above 1900 K, $G_s(r,t)$ deviates from the Gaussian shape and develops a tail, which (i) depicts discernible peaks, particularly prominent at longer times, and (ii) varies exponentially with distance at a time when C_d exhibits a peak amplitude (τ_a). The peaks are characteristic of hopping processes wherein ions undergo discrete jumps²² (Sec. E of [64]); we have verified that the peak locations agree closely with the nearest neighbor positions in the O-O radial distribution function. The exponential tail in $G_s(r,t)$, on the other hand, connotes the presence of faster moving ions—the characteristic signature of DH—which is also observed in super cooled liquids, colloids, and granular materials.²³ With increasing temperature, the exponential tail at τ_a strengthens, which confirms the presence of DH. The α_T and λ_T stages of DH can also be distinguished from the progression of the exponential tail. At 2200 K, the exponential tail in G_s at τ_a (80 ps), which is somewhat underdeveloped with corrugations, sustains for longer periods of time suffering only a modest change, signifying a solidlike (α_T) DH response. In contrast, at a temperature of 2400 K (and above), the G_s tail at τ_a is smoother, which is analogous to that in typical super cooled liquids, signifying a liquidlike (λ_T) DH response; for the higher temperatures, the exponential tail of G_s also deteriorates faster.

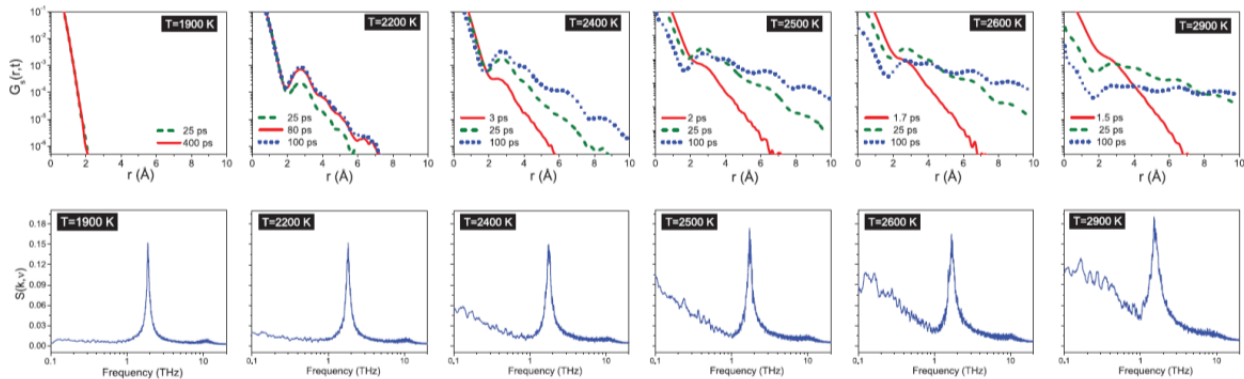


Figure 2.4.1.3 - Top panels: The van Hove self-correlation function $G_s(r,t)$ for the oxygen ions at different temperatures—the solid line corresponds to the time when C_d exhibits a peak amplitude. Bottom panels: Partial dynamic structure function for oxygen ions (arb. units) for a wave vector of $k = 0.28 \text{ \AA}^{-1}$, which is representative of the hydrodynamic limit.

In the bottom panels of Fig. 2.4.1.3, we highlight the crossover from a solidlike state to a more liquidlike state by alerting one to the appearance of a hydrodynamic Rayleigh peak ($\nu \approx 0$) in the partial dynamic structure function of the oxygen ions for a wave vector, $k = 0.28 \text{ \AA}^{-1}$. For $1900 \text{ K} > T < 2200 \text{ K}$, a partially formed hydrodynamic peak is discernible, indicating a somewhat lethargic disordering mechanism. The Rayleigh peak, however, becomes unmistakable with increasing temperature and its magnitude relative to that of the elastic peak again confirms a liquid like state beyond 2400 K .

2.4.2: Dynamic Facilitation in superionic conductors

In the current work, we employ the mobility transfer function^{65,66,67} to assess whether dynamics is facilitated in superionic conductors. The mobility transfer function gives the probability of a neighbor of a mobile ion becoming mobile, relative to that of a random ion becoming mobile. Values close to unity indicate that the mobility is randomly transferred while a higher value indicates the proclivity for mobile ions to transfer their mobility to physically adjacent immobile ions. In our analysis, we show that mobility propagates continuously to the neighboring ions, and the strength of the DF increases at the order-disorder temperature (T_o), exhibits a maximum at an intermediate temperature, and then decreases as the temperature approaches T_λ . This waxing and waning behavior with temperature is identical to the variation of the correlation in propensity (C_d), which we have used in the past²⁰ to establish the onset, rise, and fall of DH in superionic conductors. The close correspondence between DH and DF suggests, but does not prove conclusively, that DF underpins the heterogeneous dynamics in superionic conductors.

The spatio-temporal dynamics of two fluorite-structured superionic conductors, CaF_2 and UO_2 , are evaluated through atomistic simulations. In fluorites, the cations are arranged in a face-centered cubic (FCC) structure while the anions occupy the eight tetrahedral interstitial sites that form a simple cubic sublattice. Both CaF_2 and UO_2 are modeled using rigid-ion two-body potentials. The parameters for CaF_2 , which are adopted from Gillan et al.,⁶⁸ reproduce a number of thermodynamic and defect properties. For UO_2 , the potential also includes an additional Morse term to describe the energy of covalent bonding, attributed only to anion-cation interactions. To account for the partial charge transfer between the ions, each ion has a fractional (non-formal) effective charge, which is the product of its “formal” charge and an ionicity parameter, $\zeta < 1$. The parameters for UO_2 are obtained from Yakub et al.³⁵ which follows an optimization that best reproduces a host of thermodynamic and transport properties. In all the simulations, the long-range Coulomb interactions are calculated using the Wolf direction-summation method,⁶⁹ which we have benchmarked to the standard Ewald method. In the Wolf method, both the Coulombic energies and forces are truncated at a fixed cutoff radius with charge compensation on the surface of the truncation sphere.

All the simulations are performed using periodic boundary conditions in a cubic system with 6144 ions. The Newton equations of motion are integrated using the Velocity-Verlet algorithm with a time step of 1 fs. The system is initially equilibrated in an NPT ensemble for 25 ps at zero pressure. The properties are subsequently evaluated when the system evolves in an NVE ensemble, and all the results are averaged over 10 independent runs.

First of all, we have verified that the potentials reproduce the characteristic superionic transition temperature (T_λ). In Figure 2.4.2.1, the variation of specific heat with temperature is shown, evaluated as

the temperature derivative of total energy whilst the system is maintained at zero pressure. The temperature corresponding to the peak in C_p represents the transition temperature and the agreement with the experimentally measured T_λ is excellent for both CaF_2 and UO_2 .

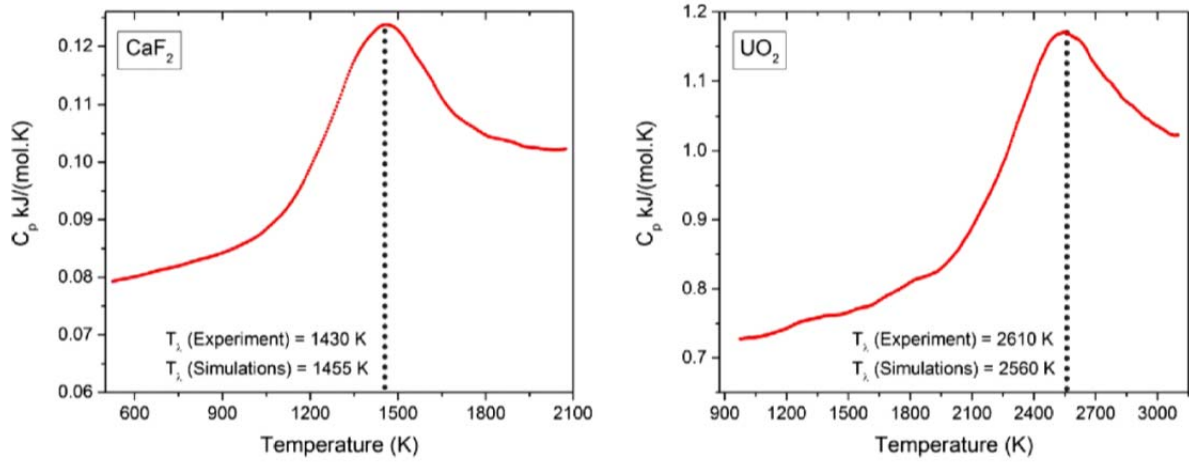


Figure 2.4.2.1 - Variation of C_p with temperature for CaF_2 and UO_2 , obtained from MD simulations.

Unlike supercooled liquids, there is a well-defined crystalline order before the order-disorder transition temperature in superionics. We had shown in our previous work²⁰ that the Wendt and Abraham ratio, defined as $\text{RWA} \equiv g_{\min}/g_{\max}$, where g_{\max} and g_{\min} are the values of the first peak and first minimum, respectively, in the anion-cation radial distribution function, captures the order-disorder or the onset transition temperature (T_α) for UO_2 . We illustrate here that the same metric predicts a similar transition for CaF_2 , as shown in Figure 2.4.2.2. Below experimental T_α , RWA is practically zero for both CaF_2 and UO_2 , indicating a well-ordered crystalline structure with negligible probability of finding a neighboring ion between the lattice sites. Close to experimental T_α , RWA becomes non-zero signaling an onset for the disordered state; as temperature increases, RWA increases rapidly with temperature, which is indicative of enhanced disorder.

The chief metric applied to identify DF is the mobility transfer function that has been used in the past to quantify DF in supercooled liquids. We begin by choosing a time interval Δt_{12} (say, from time t_1 to t_2) and list all the ions that are most mobile; we use top 5%, which is consistent with the past investigations in supercooled liquids. It should be noted here, however, that only anions are considered as they become mobile above T_α , and typically hop from one lattice site to another in a collective manner⁷ without forming permanent defects. Next, a second list of the most mobile ions (top 5%) in the subsequent time interval, Δt_{23} , is created; here, Δt_{12} and Δt_{23} are back-to-back time intervals with $\Delta t_{12} = \Delta t_{23} = \Delta t$.

We now evaluate the probability distribution $P_F(r, \Delta t)$ of finding a smallest distance r between an ion that is mobile in Δt_{23} but not in Δt_{12} , and any of the mobile particles in Δt_{12} ; the configuration of system at the intermediate time t_2 is employed in evaluating these relative distances. We then compare this distribution with $P^*_F(r, \Delta t)$, representing the distribution for random ion mobility; in this case, all the mobile ions in Δt_{23} are randomly selected from non-mobile ions in Δt_{12} . If dynamics is facilitated, then $P_F(r, \Delta t)$ will have a higher first neighbor peak relative to that in $P^*_F(r, \Delta t)$. Identical distributions, however, will reflect random mobility propagation in the system.

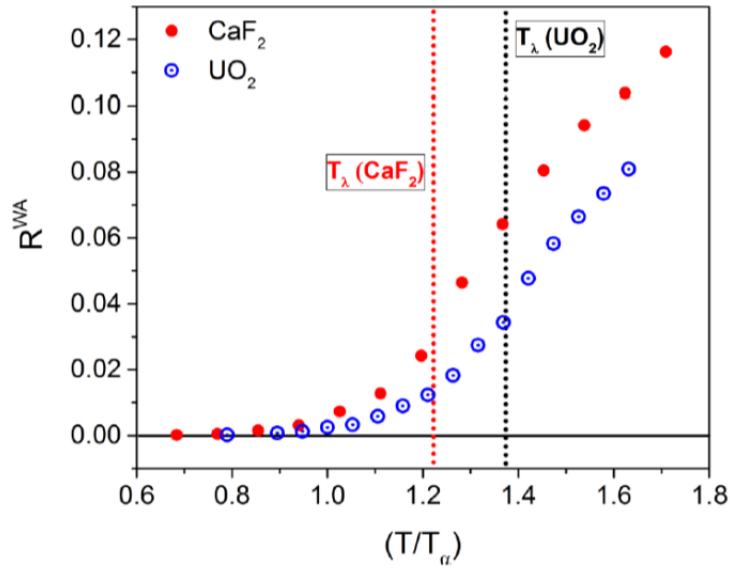


Figure 2.4.2.2 - Wendt and Abraham ratio for CaF₂ and UO₂ showing the order disorder transition at T_α .

Figure 2.4.2.3 depicts the spatial variation of $P_F(r, \Delta t)$ and $P_F^*(r, \Delta t)$ for CaF₂ at two different temperatures, $T = 1400$ K and 1600 K with a Δt of 1.0 ps. The lower temperature (1400 K) is below T_λ where DH is expected to be most prominent, while the higher temperature (1600 K) is above T_λ but below the melting point. As noticed from the left panel (a), the first neighbor peak for $P_F^*(r, \Delta t)$ is significantly higher than that of $P_F(r, \Delta t)$, which demonstrates that the probability of anion becoming mobile in Δt_{23} is significantly higher if it is located in close proximity to an anion that was mobile during Δt_{12} . However, for the same Δt at 1600 K (see right panel in Figure 2.4.2.3), the two distributions are almost identical implying that mobile ions in back-to-back time intervals are almost uncorrelated. Thus, dynamics is strongly facilitated at a temperature of 1400 K but not at 1600 K. The distributions delineated in Figure 2.4.2.4 invoke an identical conclusion for UO₂ thereby strongly suggesting that facilitated dynamics and the ensuing dynamical heterogeneity may be a hallmark of a large class of type II superionic conductors.

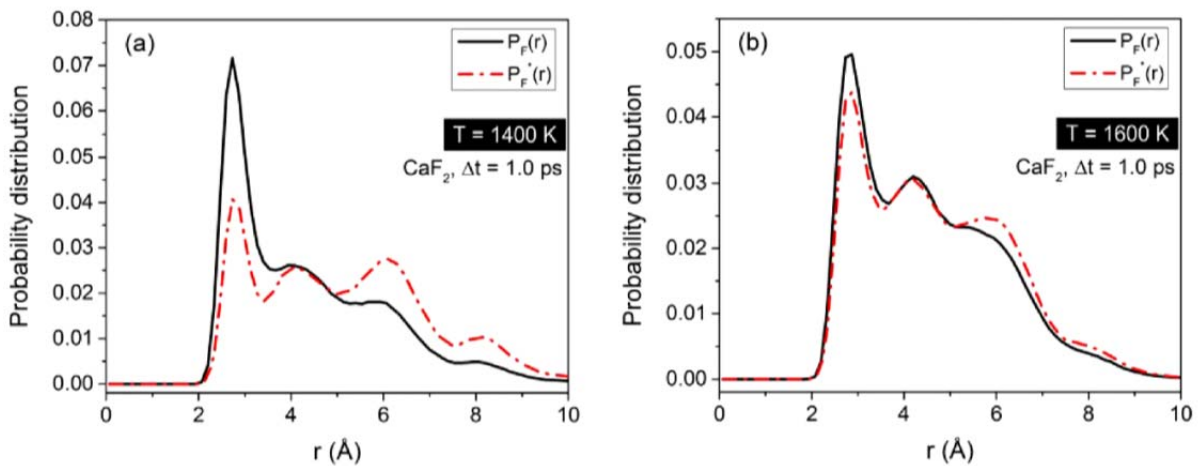


Figure 2.4.2.3 - Probability distributions $P_F(r)$ and $P_F^*(r)$ for fluorine ions at (a) 1400 K and (b) 1600 K.

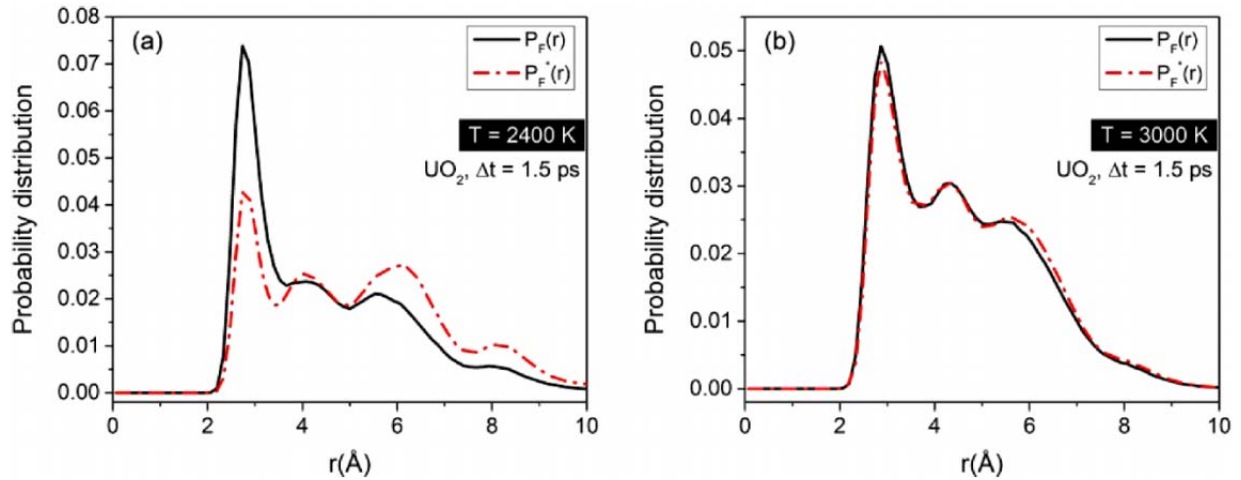


Figure 2.4.2.4 - Probability distributions $P_F(r)$ and $P^*_F(r)$ for oxygen ions at (a) 2400 K and (b) 3000 K.

The strength of DF at any temperature T can be quantified through mobility transfer function $F(\Delta t, T)$ is a measure of the probability for an immediate neighbor of a mobile ion becoming mobile relative to that of a random ion becoming Mobile. Values close to 1 indicate that the mobility is randomly transferred but higher values indicate the proclivity for highly mobile regions to arise near regions that were previously mobile. We show $F(\Delta t)$ for various Δt values and temperatures in Figure 2.4.2.5 for CaF_2 (left panel) and UO_2 (right panel).

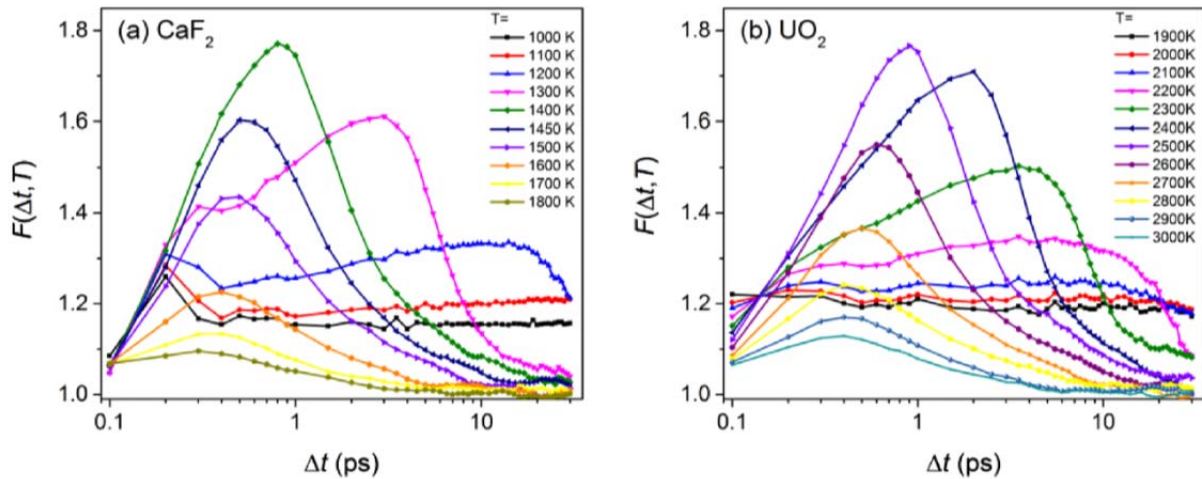


Figure 2.4.2.5 - Mobility transfer function $F(\Delta t, T)$ representing the strength of dynamic facilitation, for (a) CaF_2 and (b) UO_2 over different temperatures and time-intervals. Both CaF_2 and UO_2 show similar variation of $F(\Delta t)$, which may indicate a universality of dynamic facilitation in type II superionic conductors.

At temperatures below T_a , $F(\Delta t)$ shows a near-flat response over all values of Δt indicating that the dynamics is mostly random and non-facilitated. At temperatures near and slightly above T_a (1200 K for CaF_2 and 2200 K for UO_2), a distinct but not a fully formed peak can be identified at long times for both CaF_2 and UO_2 . Thus, an early signature of DF can be detected above the order-disorder transition temperature itself. In other words, with the advent of disorder in the anions, the dynamics is distinctly

manifested as facilitated and not random. The peak in $F(\Delta t)$ increases with increasing temperatures; the shifting to lower values of Δt shows that the relaxation time is significantly shorter at high temperatures. The peak value of $F(\Delta t)$ becomes maximum at a characteristic temperature close to T_λ for both CaF_2 and UO_2 . Interestingly, the peak value of 1.8, approximately (for both conductors), is very similar to moderately supercooled states as well as in colloidal suspensions. We have further verified that DF is manifested in another superionic conductor BaF_2 using atomistic simulations (results not shown). Thus, there appears to be convincing evidence to conjecture that dynamic facilitation is inherent to all fluorite-structured (type II) superionic conductors.

We will now compare the evolution of DF with DH at different temperatures. In Section 2.4.1 we established DH at temperatures greater than T_α using dynamical correlations of propensity in UO_2 . Typically, DH is quantified by the generalized four point susceptibility function, χ_4 . For supercooled liquids, $\chi_4(t)$ shows a maximum at a time that is of the order of alpha relaxation time and the magnitude of $\chi_4(t)$ - max shows a monotonic increase with decreasing temperature, illustrating the growing spatial correlations. However, χ_4 is not a suitable metric for studying superionic conductors owing to its inability to differentiate a crystalline state from a very deeply supercooled state. Together with exponential tail portrayed in the self van Hove correlation and hydrodynamic modes in the dynamic structure function, we showed that DH advances and then retreats in UO_2 at temperatures above T_α . Figure 2.4.2.6 depicts the peak values of $F(\Delta t)$ at different temperatures for UO_2 and CaF_2 and compares that of C_d (only for UO_2). The remarkable waxing and waning behavior of the peak values of C_d and $F(\Delta t)$ compels us to conclude that dynamic facilitation is intimately associated with the spatially heterogeneous dynamics in type II superionic conductors.

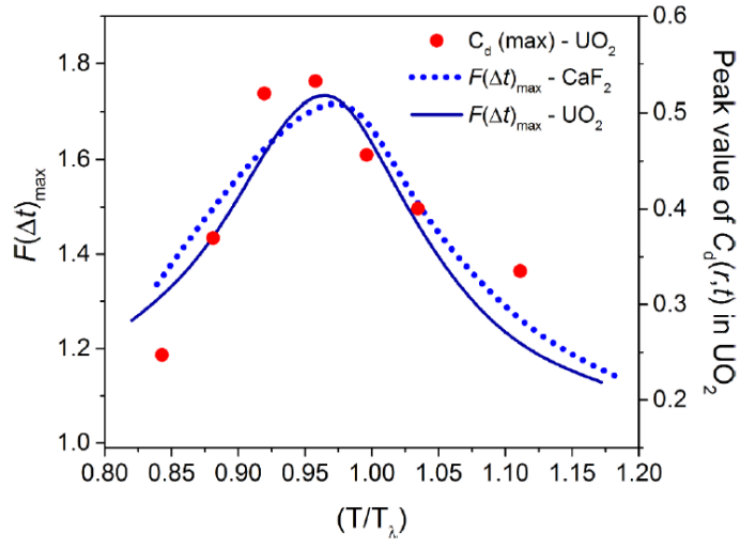


Figure 2.4.2.6 - Waxing and waning behavior of DF in CaF_2 and UO_2 illustrated by the variation of maximum value of $F(\Delta t)$, a measure of DF, with temperature, and comparison to the peak values of C_d (for UO_2), a measure of DH.

Task 3: Characterization of refractory materials for pre-irradiation and post-irradiation comparison

3.1: Cantilever fabrication for measuring radiation impact on residual thin film stresses in 3C-SiC

The cantilever is an ideal structure to characterize the internal stress of the 3C SiC since if a cantilever under fixed-free conditions and made of a homogenous material would have no intrinsic stress-induced bending if the intrinsic stress is uniformly distributed throughout the film thickness. As a result any nonuniformity in the stress distribution throughout the thickness of the film would cause a gradient in the stress. The gradient in the stress gives rise to bending of the cantilever after release from the substrate and is a direct indication of the intrinsic stress gradient of the 3C SiC film.

Two process designs were developed to fabricate the micro cantilever devices with the difference between the two approaches being based on the method used to release the SiC cantilever beams from the silicon substrate. The initial approach involved etching the silicon substrate using a potassium-hydroxide (KOH) anisotropic chemical etch but due to etch difficulties with post-irradiated samples and stress-induced delamination a purely plasma-based approach was needed. The need for a plasma-based process flow was also due to an oversight in the initial photolithographic mask design as discussed at the end of this section.

The mask design was based on a design used by Liudi Jiang et al. who used this design in order to analyze the resonance characteristics of 3C-SiC for microsensor applications.⁷⁰ The anchors serve to eliminate any torsional component of beam deflection. In the mask design process it was important to incorporate microcantilever devices across the entire wafer to account for spatial film thickness and stress variations. Shown below in Figure 3.1.1 is a schematic of the photolithography mask used for pattern transfer of the cantilever design onto the wafer. Each die consists of two sets of four cantilevers with open areas adjacent to each set. This enables a direct comparison of adjacent sets of cantilevers for pre- and post-irradiation.

The preliminary analysis prior to the first step of the cantilever fabrication process involves the use of profilometry to measure wafer curvature after SiC growth and determine the residual film stress. Following the determination of the stress, a 200 nm aluminum thin film is deposited on the SiC to serve as a hard mask for subsequent plasma etching and the structural layer for the first level photolithography. The deposition of the aluminum film was achieved by the thermal evaporation of 99.99% pure aluminum pellets placed on a tantalum crucible which is placed in physical contact with two separate electrodes. The largest concern during the evaporation process is the flow of the molten aluminum from the center of the crucible to the opposing edges. This results in the need to continuously increase the output voltage of the transformer in order to maintain a constant current and therefore a constant deposition rate in order to ensure film quality and uniformity. The aluminum thickness was measured with a monitor wafer using profilometry. This thickness was consistently on the order of 200 nm, taking into account nonuniformities during the evaporation process.

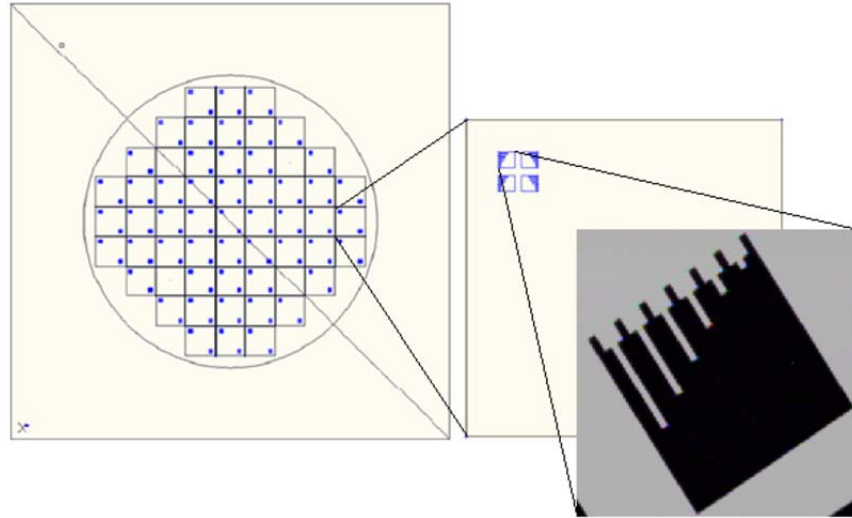


Figure 3.1.1 - 1st level photolithography mask layout.

Following deposition of the aluminum hard mask, the first lithography step is used to transfer the cantilever pattern onto the hard mask. The configuration after the first lithography step is shown in the quarter-dye illustration below in Figure 3.1.2.

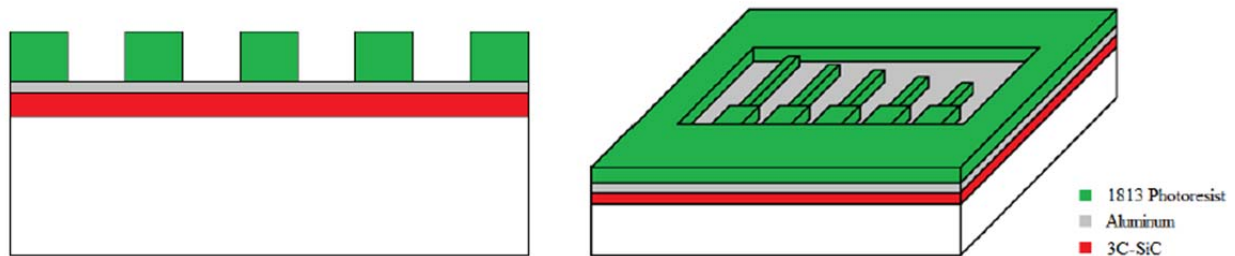


Figure 3.1.2 - Quarter die layout after the first lithography step

The next step in the process involves a chemical wet etching of the exposed aluminum for which the 1813 photoresist acts as a mask. The chemical is a pre-mixed Transene – Type A solution which is heated to a temperature of 40 °C to achieve an approximate etch rate of 80 Å/second. In order to ensure a complete etch, the standard time for an aluminum thickness of 200 nm is three minutes which includes a 50% overetch. Immediately after etching the wafers are thoroughly rinsed, placed in a spin dryer, and optically inspected to ensure the quality of the etching process.

The next part of the process involves plasma etching through the exposed 3C SiC down to the silicon substrate. For this part of the fabrication process an inductively-coupled plasma system was used to anisotropically etch the SiC. The ICP system used was the Alcatel AMS-100 deep reactive-ion etcher. The process parameters used to etch the 3C SiC films are shown below in Table 3.1.1.

The next steps of the process flow involved the removal of the aluminum hard mask and the deposition of thin nitride and polysilicon films in order to perform the 2nd level lithography. The 2nd level lithography was necessary to isolate adjacent areas of each die in order to perform pre- and post-irradiation analysis.

The Si₃N₄ film is ultimately used as a perfectly selective mask for the final KOH silicon etch and was deposited with a standard LPCVD process using ammonia (NH₃) and DCS (SiH₂Cl₂) as feed gases at a constant temperature of 775 °C. Following the nitride deposition, a thin (~150 nm) polysilicon film was deposited in order to serve the dual purpose of providing the pattern transfer layer for the 2nd layer lithography and as an etch mask for the chemical etching of the Si₃N₄. The polysilicon deposition uses disilane (Si₂H₆) as the feed gas at a setpoint temperature of 630°C. The deposition of the silicon nitride and polysilicon was conformal with respect to the features. This was necessary in order to account for lateral etching of both films. At this point in the process flow, the 2nd level lithography mentioned previously is performed. The 2nd-level lithography step forms a trench which is later transferred into the polysilicon layer by plasma etching. The quarter-die of the process flow after the final deposition step is shown below in Figure 3.1.3.

Table 3.1.1 - Plasma process setpoints used in DRIE etching of 3C SiC films

<i>Etching Process Parameter</i>	<i>Nominal Value</i>
Pressure (mTorr)	4.125 - 4.725
SF ₆ Flow (sccm)	80
O ₂ Flow (sccm)	20
Applied RF Source Power (W)	1500
Applied RF Substrate Power (W)	80
Resulting V _{DC} bias (V)	~19
Helium Cooling Pressure (Torr) / Flow (sccm)	7.5 / 0.1

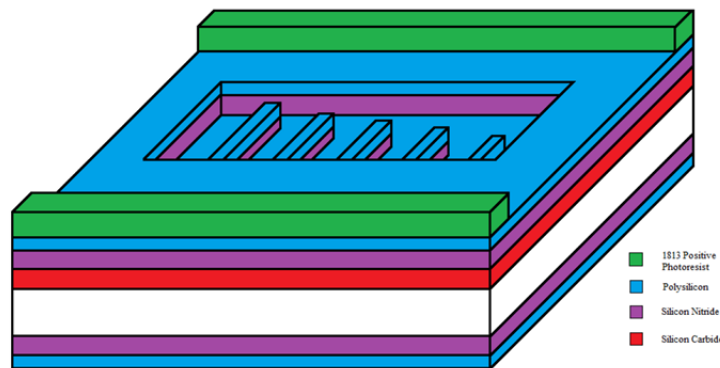


Figure 3.1.3 - Quarter die view of cantilevers following 2nd level photolithography

The next step involves etching the trench pattern into the polysilicon film using the photoresist as the etch mask. The reactive-ion etch of the polysilicon was conducted in a CCP plasma system as discussed above. The plasma etching system used to etch the polysilicon was the Semigroup RIE 1000 TP. The process parameters used in the anisotropic polysilicon etch is shown below in Table 3.1.2.

Table 3.1.2 - Plasma process parameters used to etch polysilicon in KOH-based design process

<i>Etching Process Parameter</i>	<i>Nominal Value</i>
Pressure (mTorr)	30
SF ₆ Flow (sccm)	15
O ₂ Flow (sccm)	7.5
Applied RF Substrate Power (W)	80
Resulting V _{DC} bias (V)	~132

By plasma etching the polysilicon, the material will only be removed from the top of the wafer unlike chemical etching which would remove polysilicon from the top and bottom of the wafer. This is important because the polysilicon film serves as the etch mask for the subsequent silicon nitride chemical etch and by only removing it from exposed areas on the top of the wafer, the polysilicon on the bottom of the wafer will prevent backside etching of the underlying silicon nitride. With the polysilicon being removed only from the trenches, the remaining photoresist is stripped from the wafer using a solution bath known as Nano-Strip™ which is roughly 90% sulfuric acid. Following the removal of the photoresist, the wafers are rinsed and placed in a spin dryer.

Following the polysilicon etching, the Si₃N₄ film is exposed only in the trenches where the cantilevers are released for pre-irradiation analysis. The next step of the fabrication process involves a hot phosphoric acid chemical etch in order to remove the silicon nitride to expose the silicon substrate. Only the silicon nitride not masked by the polysilicon will be etched in the hot phosphoric acid solution heated to 180 °C. The solution is pre-mixed and produced by Transene. The predicted etch rate was 12.5 nm/min and with an added overetch, the overall time of the silicon nitride chemical etch for an approximate thickness of 200 nm was 30 minutes.

At this point in the fabrication process, the cantilevers are ready to be released using KOH chemical etching. It is important to mention that in order to use a specific wafer holder for the KOH etch, which protects the sides from etching, it was necessary to use 300 μm thick silicon wafers. The cantilevers adjacent to the ones treated with KOH etching remain covered by the polysilicon and silicon nitride and therefore remain unreleased, preserving film strain for irradiation; these are later released using the same KOH process for post-irradiation stress measurement and comparison to pre-stress measurements. The KOH solution was heated to 80 °C and consisted of a KOH/deionized water ratio of 40%. The characteristic etching of KOH for (100) silicon occurs along the (110) planes as shown in Figure 3.1.4.

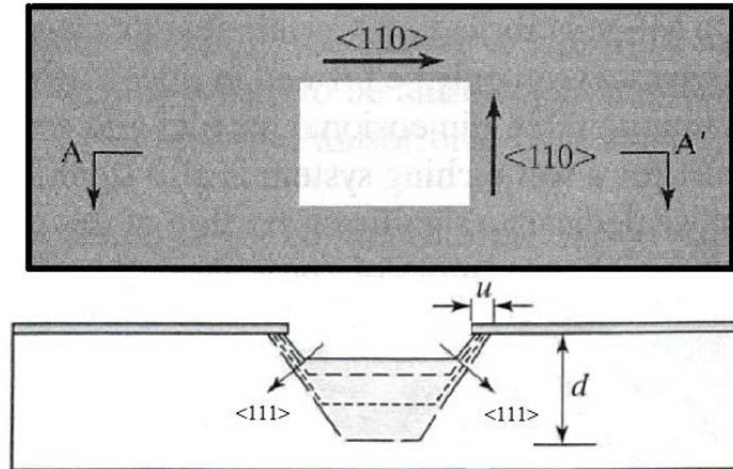


Figure 3.1.4 - Progression of KOH chemical etch of (100) silicon.

For chemical etching of (100) silicon, the etch proceeds most quickly along the $\langle 100 \rangle$ and $\langle 110 \rangle$ directions, with the $\langle 110 \rangle$ coming out of the page when referring to Figure 3.1.4 above. Etching also occurs in the $\langle 111 \rangle$ direction but at a much slower rate than the others mentioned, however it is the etch rate in the $\langle 111 \rangle$ which ultimately allows for the termination of the etch at a point resulting in an inverse pyramidal structure. Based on the size of the initial opening in the mask, the termination of the etch can be directly controlled.

The opening of the mask shown in Figure 3.1.4 was designed for a etch depth of $200\ \mu\text{m}$ with the size of the opening being $583.2\ \mu\text{m}$. This opening was determined based on the longest cantilever beam ($250\ \mu\text{m}$) plus the length of the anchor ($50\ \mu\text{m}$). This mask design introduced the inaccuracy of releasing the entire anchor of the cantilever beam which dampens the true deflection of the cantilever beam based on the size of the anchor. The original mask design is shown below in Figure 3.1.5.

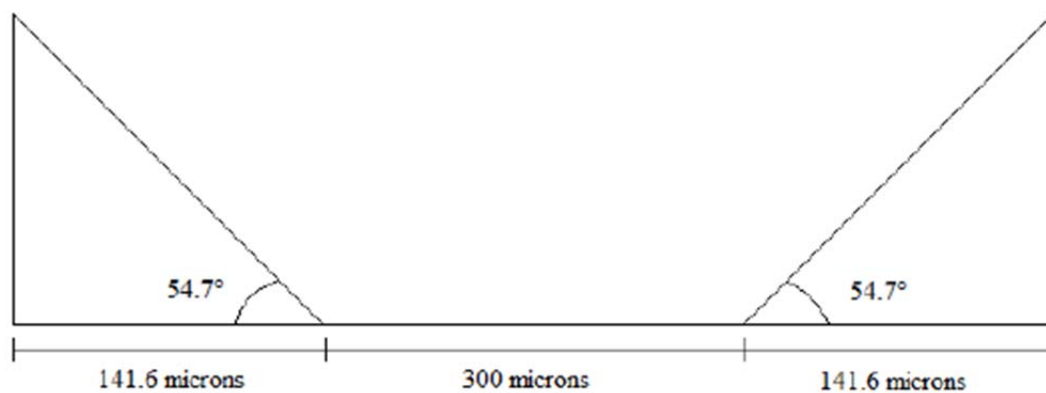


Figure 3.1.5 - Original dimensions used to determine mask design for first level lithography

In order to correct this oversight, the open area of the mask shown in Figure 3.1.6 can be reduced by a total of $50\ \mu\text{m}$ in order for the release point to occur at a point half the length of the anchor. Due to the cost and time constraints of making a new mask, a plasma-based work around was developed by using

a low-bias, high pressure plasma etch which isotropically etched the silicon substrate underneath the thin-film SiC, while incurring negligible lateral etching of the SiC cantilever beams. This etch was done using the previously mentioned DRIE system for which the process is shown below in Table 3.1.3.

By using an isotropic plasma etch, the release point can be controlled by the duration of the etch. Based on initial characterization of the lateral etch rate of the process, the optimal time was determined to be 18.664 minutes. One issue with the initial characterization of the silicon etching process was filaments of silicon adhering to the SiC cantilever beams after release. This can be seen below in Figure 3.1.6 and was corrected by closing the throttle valve between the plasma chamber and the turbomolecular pump to the point where it was only 25% open. This increased the pressure in the chamber to value given in Table 3.4 above and reduced the mean-free path of the ions. Reducing the mean-free path of the molecular species in the chamber results in an increase in the local density of chemically reactive species and thus improves the isotropic etch characteristics.

Table 3.1.3 - DRIE process parameters used in isotropic etching of silicon substrate in plasma based lift off process flow

<i>Etching Process Parameter</i>	<i>Nominal Value</i>
Pressure (mTorr)	4.125 - 4.725
SF ₆ Flow (sccm)	80
O ₂ Flow (sccm)	20
Applied RF Source Power (W)	1500
Applied RF Substrate Power (W)	80
Resulting V _{DC} bias (V)	~19
Helium Cooling Pressure (Torr) / Flow (sccm)	7.5 / 0.1

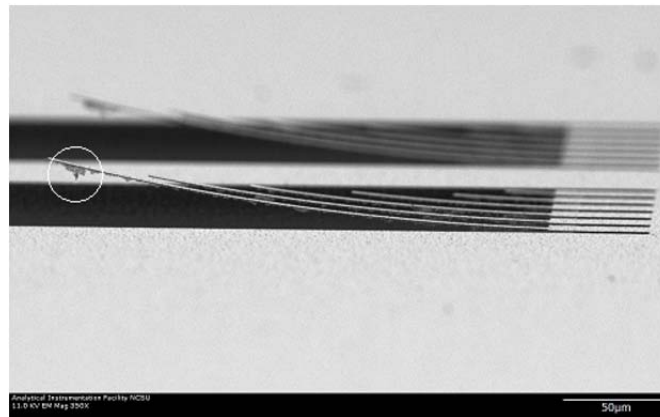


Figure 3.1.6 - SEM image showing released 3C-SiC cantilevers. The circled region notes residual silicon attached to the cantilever due to insufficient overetching of the substrate.

The additional need for a plasma-based cantilever release method was due in combination to the high residual stresses of the thin-film SiC and the evolution of crystalline changes as a result of radiation damage since the peak damage of all radiation experiments described later occurred in the silicon substrate. The change in the crystal structure of the silicon substrate is evident by the evolution of the (311) silicon peak in Figure 3.1.7. The evolution of the (311) Si peak and to a lesser degree the (422) Si peak as a result of increasing radiation dose is due to the amorphization of the Si substrate which changes the anisotropic KOH etching to the point that the stress effects at the edges of the features become problematic and the cantilever devices are destroyed. It was for this reason that an approach utilizing high density plasma etching was used both to etch the cantilever pattern into the SiC and to subsequently release the cantilevers from the silicon substrate.

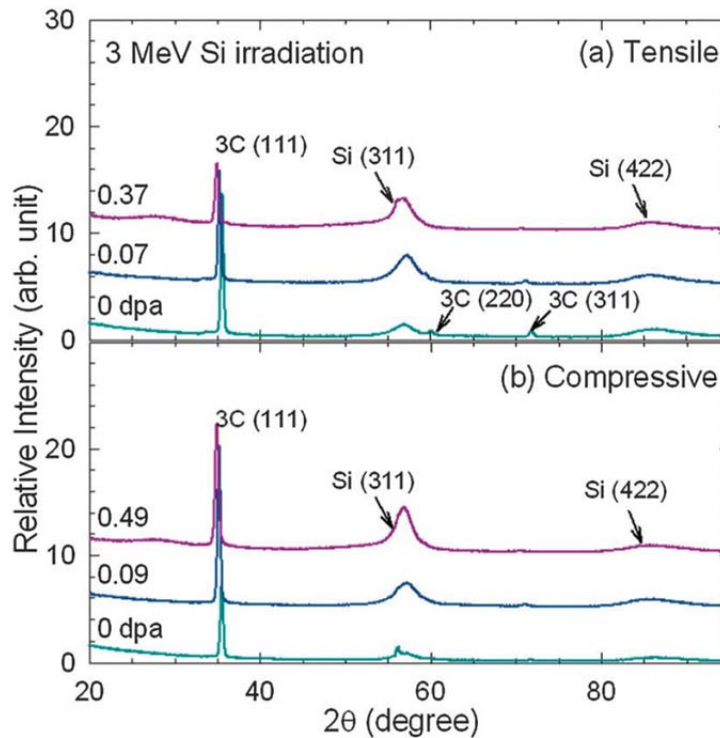


Figure 3.1.7 - Evolution of prominent 3C SiC and Si peaks as a function of irradiation dose. Note the amorphization of the Si (311) peak, necessitating the need for an alternate for KOH release process.

The plasma-based process utilizes sputtered titanium and aluminum to act as hard masks for the etching process, since the polysilicon and silicon nitride used in the KOH process do not yield the selectivity necessary to conduct the plasma etching. As a result, ion irradiation needs to be done through the thin titanium hard mask in order to do post irradiation release. The first step in this process flow involves the DC sputtering of a 200 nm titanium film on the 3C SiC thin-film followed by the identical 1st level lithography first evaluated for KOH lift off of the beams. The titanium is then etched using a buffered oxide etch (BOE) solution which is essentially diluted hydrofluoric acid. This now provides the cantilever pattern that can be etched into the SiC film. The next step in the process flow involves the DRIE plasma etching of the exposed SiC. Following this etch, the deposition of a thin, 100 nm aluminum layer is conducted to serve as a sacrificial layer to do the 2nd level lithography which involves isolating two adjacent sets of cantilevers in each die. After deposition of the aluminum film, the 2nd level

photolithography is performed and the exposed aluminum is chemically etched using the same solution as described in the KOH-based process flow the process progression. The final step in the process flow involves the DRIE isotropic etch of the exposed silicon substrate in order to release the cantilevers. Following this, the remaining exposed titanium is removed by BOE and the remaining aluminum is stripped by chemical etching and since the Transene solution described previously is selective with respect to titanium, the unetched titanium hard mask will not be removed. This process flow is still a work in progress due to the need to perform an additional 2nd level photolithography step after irradiation of the die.

3.2: Resistive elements for in-situ measurement of radiation damage accumulation in 3C SiC

In order to create 3C-SiC samples for the measurement of electrical resistivity, a layer of 3C-SiC is grown on silicon dioxide in order to electronically isolate the thin film from the silicon substrate. There are two methods for oxidation which are employed; dry and wet oxidation. The method used in order to form oxide for the electronic isolation of the SiC thin films is dry oxidation performed at 950 °C. Despite the fact that wet oxidation is a quicker process, dry oxidation is chosen because the density of the oxide layer is greater resulting in a better isolation layer. In order to achieve appropriate isolation, 500 Angstroms of SiO₂ is deposited on 100 mm, <100> oriented, 500µm thick silicon substrates. All wafers are cleaned (RCA bath and buffered oxide etch) and spin dried before being loaded in the oxidation furnace. The depositions are performed in a low pressure chemical vapor deposition furnace using O₂ and HCl gases as precursors at the specified temperature. The furnace configuration is similar to the furnace used to grow 3C-SiC.⁷¹ The design of the furnace and heating source allows for temperature uniformity on the order of +/- 0.1°C. Throughout all oxidation runs the temperature is monitored at three different points in the furnace to ensure a uniform deposition.

The oxygen is the primary gas which reacts with the silicon from the substrates to form the SiO₂ layer. The HCl gas in the process serves several purposes including the removal of any metal ions which may be present on the Si substrates and to keep the furnace and furnace pipes clean of the O₂ gas. With the details of the oxide growth known, several concepts can be applied in order to determine oxidation time and the amount of Si consumed during the process.

The growth rate of SiO₂ in the NCSU Nanofabrication facility (NNF) furnace has been characterized by the staff using the average oxide thicknesses from various furnace runs at various run times. The model used to characterize the data is the commonly used Deal-Grove model. The data is summarized and fit with a polynomial equation in Figure 3.2.1. With the exception of a few samples, the data has tracked with the parabolic relationship fairly well indicating the accuracy of the model.

As evident from the plot, the growth rate of SiO₂ is governed by a parabolic growth rate. Based on previously collected data, the growth time needed in order to achieve the desired 500 Angstroms of SiO₂ is approximately 75 minutes. With this data the growth rate is determined to be 0.111 Angstrom/sec (6.667 Angstrom/min). After the 75 minute deposition at 950 °C, the thickness of the SiO₂ was measured using a Nanometrics® reflectometer. The thickness of the oxide layer varied no more than 5 Angstroms across the surface of each wafer. Using five data points, the thicknesses of the SiO₂ layer on five wafers

was measured and averaged together. All substrates had a nominal thickness of 52nm oxide growth with this process.

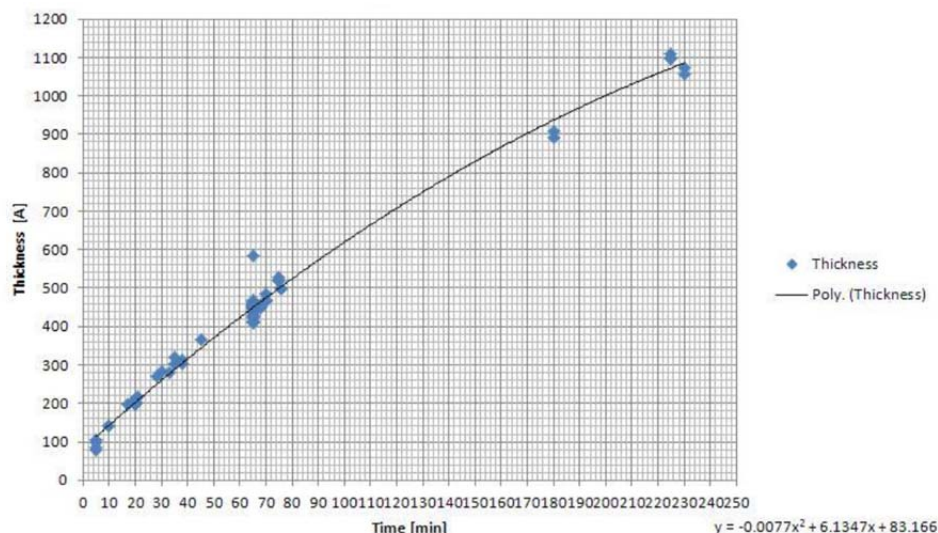


Figure 3.2.1 - Oxide thickness vs. time at 950C for the NCSU NNF dry oxidation process

Once the isolation layer of silicon dioxide was grown on the wafers, a LPCVD deposition of n-type 3C-SiC was performed using the procedure outlined in section 3.1. In addition to being used for resistivity measurements, the 3C-SiC on SiO₂ wafers were also used as monitors for determining the resistivity of the 3C-SiC layers grown on bare silicon wafers. These values are important for the determination of p-n junction parameters. The monitor wafers used to determine the resistivity of the thin films grown on bare silicon substrates were used as the samples for the resistivity tests. Information including film resistivity and thicknesses for two runs will be described in the following section. The final structure of the monitor wafers used for resistivity measurements is illustrated below in Figure 3.2.2.

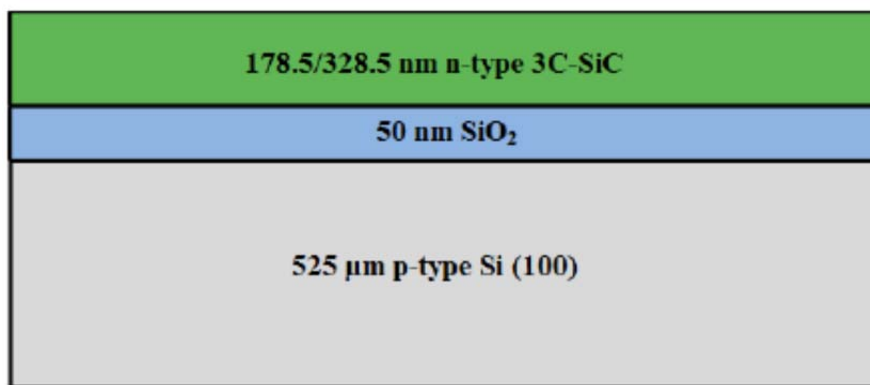


Figure 3.2.2 – Illustration of sample used for resistivity measurements.

Task 4: Irradiation and in-situ measurement of damage accumulation in refractory materials

4.1: Stacking fault generated improvements in SiC radiation tolerance

In the current work, a high-density of SFs with average layer spacing of less than 2 nm are engineered into nanocrystalline SiC during the film deposition process forming a nano-lamellar structure of low-energy interfaces, and these SFs are stabilized at the GBs in the nano-sized grains. Clear experimental evidence and atomic-level insights from MD simulations are presented and discussed for the enhanced radiation-resistant behaviour in this nano-engineered SiC (NE-SiC). The outstanding self-healing behaviour is attributed to the high density of SFs that have significant impact on defect migration and annihilation.

Irradiation studies of the $\langle 0001 \rangle$ -oriented single crystal of 4H SiC (CREE, Inc.) were performed using 550 keV Si⁺ ions at 60° off the surface normal at room temperature. The shallow damage peaked at about 165 nm was readily measured by Rutherford backscattering spectrometry (RBS) in channeling geometry with good depth resolution. The minimum RBS yield from the virgin crystal is ~1.5%, indicating a negligible level of defects or damage in the as-received material. Irradiations to ion fluences from 5×10^{12} to 2×10^{15} Si cm⁻² were performed to produce damage states ranging from minor disorder to a fully amorphous layer. Due to the high crystalline quality of the available 4H-SiC wafer, which was superior to the 3C single crystal wafer, the more detailed study of damage accumulation was carried out on the 4H SiC samples; however, the results should provide relevant reference to the radiation behavior of 3C SiC. To compare and verify the critical dose for amorphization of 3C-SiC, Si⁺ ion irradiations were carried out under the same irradiation conditions (energy, incident angle and target temperature) in the $\langle 001 \rangle$ -oriented 3C-SiC (HOYA CORP. SiC Development Center) to ion fluences of 2.5×10^{14} , 3.25×10^{14} , 4.5×10^{14} cm⁻² and 7.25×10^{14} cm⁻², and the disorder level was determined by RBS channeling measurements.

Two 3C NE-SiC films with either tensile or compressive stress were grown on a Si (100) wafer by the methods described in Section 2. The samples were sequentially irradiated along the surface normal with 3 MeV Si to ion fluences of up to 6.6×10^{15} cm⁻². Irradiation was also performed on a NE-SiC tensile sample with 2 MeV Si, along surface normal, to a much higher fluence of 3×10^{16} cm⁻² in order to estimate the dose required for complete amorphization. The 2 and 3 MeV Si ions, with the Si concentration peaked at depths of ~1600 and 2100 nm, respectively, penetrated through the NE-SiC film and stopped in the Si substrate.

Defect production and damage evolution resulting from ion irradiation depend on ion mass, energy, fluence and irradiation temperature. Because of the variation of energy deposition and defect/damage production with depth and ion irradiation conditions, the local dose in displacements per atom (dpa), which is proportional to the local energy deposition to atoms (as opposed to electrons), is used to quantify and evaluate the response of materials under different irradiation conditions. Defect production and damage evolution are commonly analyzed and correlated as a function of dose in dpa. Ion fluence, defined as the total number of particles passing through a unit area in a specific time interval in units of cm⁻², can be related to local dose at a certain depth or an average dose over a certain depth interval, which can be used for comparison of SiC response under different irradiation conditions. The local or average

dose in dpa was determined for both the present irradiation conditions and prior irradiation studies using the Monte-Carlo code Stopping and Range of Ions in Matter (SRIM) under full-cascade simulations (version 2008.04) with an assumed sample density of 3.21 g/cm³ and threshold displacement energies of 20 and 35 eV for the C and Si sublattices, respectively.¹⁵ The SRIM predicted displacement damage profile is determined from the sum of the predicted vacancy concentration of Si and C and the replacement collisions. The conversion factor at the damage peak from ion fluence (1014 cm⁻²) to dose (dpa) was 0.088 dpa/(1014 cm⁻²) under the 550 keV Si irradiation. For the NE-SiC samples, conversion factors of 0.006 and 0.0074 dpa/(1014 cm⁻²) were used that represented an average dose over the thickness of the NE-SiC films of tensile and compressive samples, respectively.

Characterization of radiation damage was carried out at room temperature using complementary techniques of RBS, glancing-incident angle X-ray diffraction (GIXRD) and transmission electron microscopy (TEM). For the single crystal samples, channelling RBS was performed along <0001> or <001> axial directions using 2.0 MeV and 3.5 MeV He⁺ at a scattering angle of 150° to quantitatively determine the degree of disorder. Due to a much higher non-Rutherford cross section with C, the 3.5 MeV He ion beam was used to detect damage in the C sublattice. For the NE-SiC samples, GIXRD was carried out using a Phillips X'Pert Multipurpose X-ray diffractometer. The glancing incident angle was fixed at $\omega = 5^\circ$ to avoid strong diffraction intensities from the Si substrate. The predominant crystalline phase of the NE-SiC films was confirmed to be polycrystalline 3C-SiC. The effective size of crystallites was estimated from broadening of the SiC (111) reflection using Jade software (Materials Data, Inc.,) employing pseudo-Voigt profile function calibrated with a LaB6 (SRM 660, NIST) internal standard. The nanocrystalline SiC has a columnar structure that is elongated along the growth direction. While GIXRD can only provide an average result assuming a homogeneous crystallite size throughout the film, it provides useful information on size change by examining a large number of grains. Irradiation-induced microstructure changes were examined using a JEOL JEM-3000F transmission electron microscope operated at 300 kV. Crystalline phases and damage states were analyzed by selected-area electron diffraction (SAED).

The MD simulations of displacement cascades were performed using the LAMMPS code with a hybrid Tersoff–ZBL potential.³⁶ Simulation boxes of 3C SiC composed of 100 x 100 x 105 hexagonal units (2 100 000 atoms) with either extrinsic or intrinsic SFs or without SFs were constructed. Three-dimensional periodic boundary conditions were imposed to model a bulk material. Prior to cascade simulations, the simulation box was equilibrated for 50 ps at 300 K by a temperature and pressure controlling scheme.³⁷ During cascade simulations, the outer 4 cells of the simulation box were kept at 300 K using a velocity scaling method in order to avoid unphysical energy propagation induced by the periodic boundary conditions. Displacement cascades were initiated by giving a kinetic energy of 10 keV to a Si atom. Simulations of displacement events along 50 randomly generated directions were performed for each system to acquire adequate statistics. The timestep was varied stepwise in order to achieve an adequate accuracy in atomic motions within a reasonable computational time. The cascade simulations were continued up to 11.2 ps. A Wigner–Seitz cell analysis³⁸ was then employed to identify defects in simulation cells. Diffusivities of Si and C interstitials were evaluated from mean square displacement of Si and C atoms, respectively, in systems containing the corresponding single interstitial atom using a Brenner-type potential.³⁹ For these diffusion simulations, 6 x 5 x 18 hexagonal units (1080 atoms) of various stacking sequences were utilized.

In nuclear reactor environments, energetic neutrons transfer energy to Si and C atoms, producing energetic Si and C recoils that are responsible for radiation damage in SiC. Since Si is more efficient in producing damage than C,¹⁴ the irradiation response of nano-engineered SiC and single crystal SiC has been investigated using Si ions. Damage accumulation dynamics, particularly under similar irradiation conditions, have been observed to be similar in 3C and 4H poly-types.^{14,15,40} Likewise, no significant difference has been observed between single crystal and large grain polycrystalline 3C-SiC.^{40,41} The disorder accumulation in single crystal 4H-SiC samples is shown in Fig. 4.1.1 as a function of dose in dpa. A continuous buried amorphous state is defined as achieving a relative disorder of 1.0. The critical dose for amorphization in 4H SiC was determined to be ~ 0.5 dpa for the Si⁺ ions. The amorphization dose in 3C SiC was previously investigated under 360 keV Ar⁺ irradiation,⁴⁰ and the re-determined dose for amorphization based on threshold displacement energies of 20 and 35 eV for the C and Si sublattices, respectively, was 0.32 dpa.⁴⁰ Damage accumulation and amorphization in single crystal 3C SiC at room temperature were also investigated in this study under 550 keV Si⁺ ions irradiation as shown in Fig. 4.1.1, and the critical dose for amorphization determined by RBS channeling measurements was ~ 0.29 dpa.

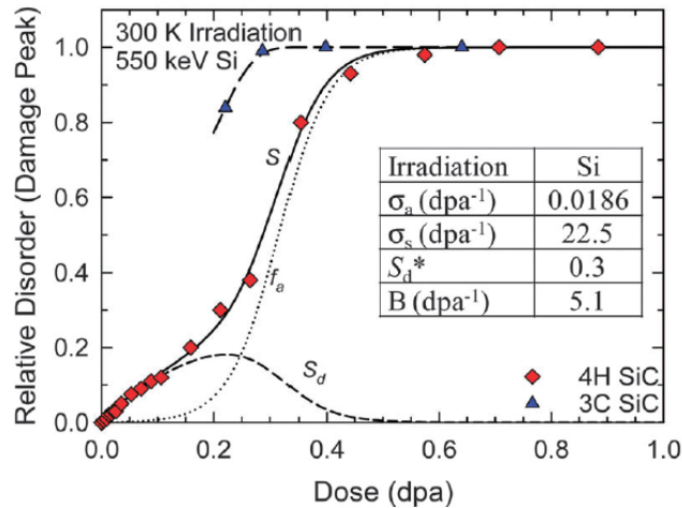


Figure 4.1.1 - Relative disorder at the damage peak as a function of local dose for 3C and 4H SiC irradiated with 550 keV Si ions at room temperature. The solid line is the fit of eqn (1) to the data, based on eqn (2) and (3) that are shown as dotted and dashed lines for f_a (amorphous fraction) and S_d (defect fraction), respectively. The fit parameters are summarized in the inset. The long dashed line for the 3C-SiC data is a curve fit to guide the eye.

The irradiation response of the 3C NE-SiC films under Si irradiation was characterized using GIXRD, as shown in Fig. 4.1.2 for both tensile and compressive samples. The GIXRD spectra for the as-deposited films and the irradiated films indicated no evidence of significant amorphization in the NE-SiC, as indicated by the strong 3C (111) diffraction peak, for doses of up to about 0.37 and 0.49 dpa, which were much higher than the amorphization dose of 0.29 dpa measured in 3C single crystal SiC. The GIXRD results indicated that both the tensile and compressive films were radiation resistant. This behaviour is dramatically different from that observed for SiC nanocrystallites embedded in an amorphous SiC matrix where the material is more radiation sensitive.^{29,30}

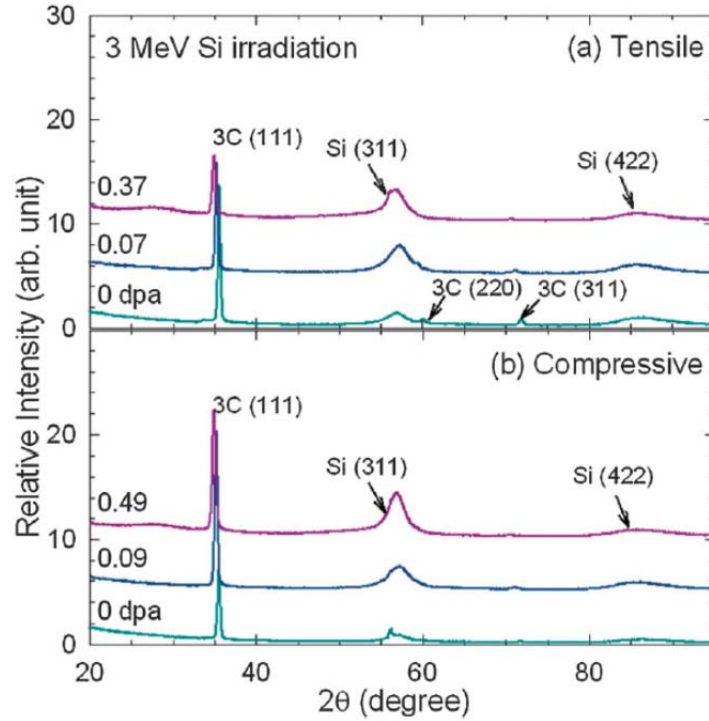


Figure 4.1.2 – GIXRD spectra for the as-deposited and irradiated NE-SiC samples. The results of both (a) tensile and (b) compressive samples are shown over a wide diffraction angle. The average irradiation dose and diffraction indices are marked on the plots. A broad peak between 25 and 30° at 0.37 or 0.49 dpa is attributed to the amorphization of the Si substrate.

Molecular dynamics cascade simulations have been used previously to study nanoscale defect production and damage accumulation processes in single crystal and nanocrystalline 3CNC-SiC.^{22,42,43} In this study, MD simulations were employed to study defect production and migration in three different simulation cells corresponding to experimental conditions: 3C-SiC single crystal, 3C-SiC containing a high density of extrinsic stacking faults, and 3C-SiC containing a high density of intrinsic stacking faults. The interval for neighboring stacking faults was randomly spaced from 1.00 to 1.99 nm. Fig. 4.1.3 (top) shows a typical defect distribution in 3C NE-SiC containing extrinsic stacking faults after a 10 keV Si primary knock-on atom (PKA) initiated close to a [111] direction. Predominate defects were intrinsic point defects: Si vacancy (Si_V), Si interstitial (Si_I), C vacancy (C_V), C interstitial (C_I), and Si and C anti-site defects (Si_C , C_{Si}). In Fig. 4.1.3 (top), Si_{SF} and C_{SF} represent Si and C atoms forming the stacking faults. Most defects created were single interstitials and vacancies with no evidence of direct amorphization. Defect production created by displacement cascades was simulated in all three simulation cells. No significant difference was observed in the defect number or defect configuration among those three cell structures, except for the formation of C split interstitial on the silicon sublattice (C_{spSi}) and C vacancy (V_C). As shown in Fig. 4.1.3 (bottom), the numbers of C_{spSi} and V_C increase rapidly around 0.1 ps due to the displacement processes, and then decrease to near constant values within a few ps due to rapid defect recovery processes. The average numbers of surviving C_{spSi} and V_C defects are 15% and 10% lower, respectively, in the simulation cells with SFs than in the single crystal cell. Such a decrease in defect production in the presence of SFs will contribute to the observed radiation tolerance, but is not a dominating factor. In addition, the MD results indicate that the mobility of interstitial Si was enhanced somewhat in the NE-SiC, while that of interstitial C and vacancies was largely unchanged. The enhanced

mobility of the interstitial Si was attributed to the existence of the stacking faults, as the mobility was clearly dependent on stacking-fault density.

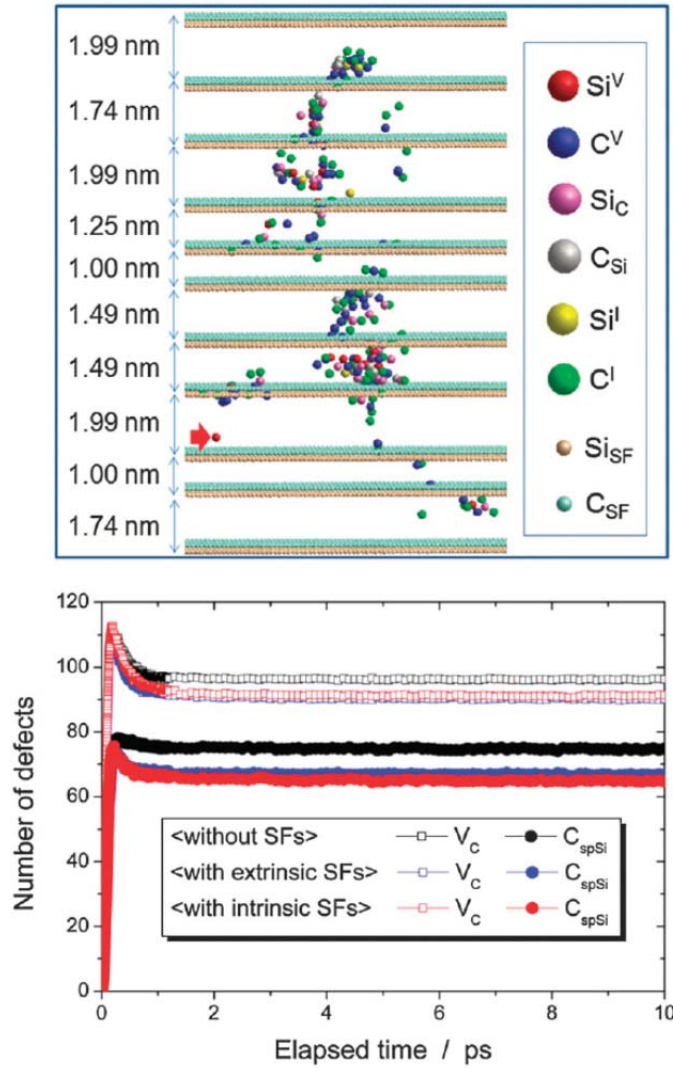


Figure 4.1.3 - Top: cross section of defect distribution produced by a 10 keV Si recoil at 300 K in 3C NE-SiC containing extrinsic stacking faults with random spacing. The arrow represents the initial position of the PKA. Scattered point defects are observed. Bottom: variation in VC and C_{spSi} numbers during and after the onset of displacement cascade.

Cross-sectional TEM images of the compressive NE-SiC are shown in Fig. 4.1.4, which are representative of the tensile samples. The engineered films with columnar structure were oriented along the c-axis and contained high densities of SFs that could be clearly observed with separation distances at the scale of nanometers in both the as-deposited sample and in the sample irradiated to 0.09 dpa. For high-dose irradiation at 0.49 dpa, the crystalline structure of the NE-SiC was largely intact, as shown in Fig. 4.1.4(f) and in the inset showing the electron diffraction pattern. The TEM results were consistent with the XRD result shown in Fig. 4.1.4(b) from corresponding compressive samples.

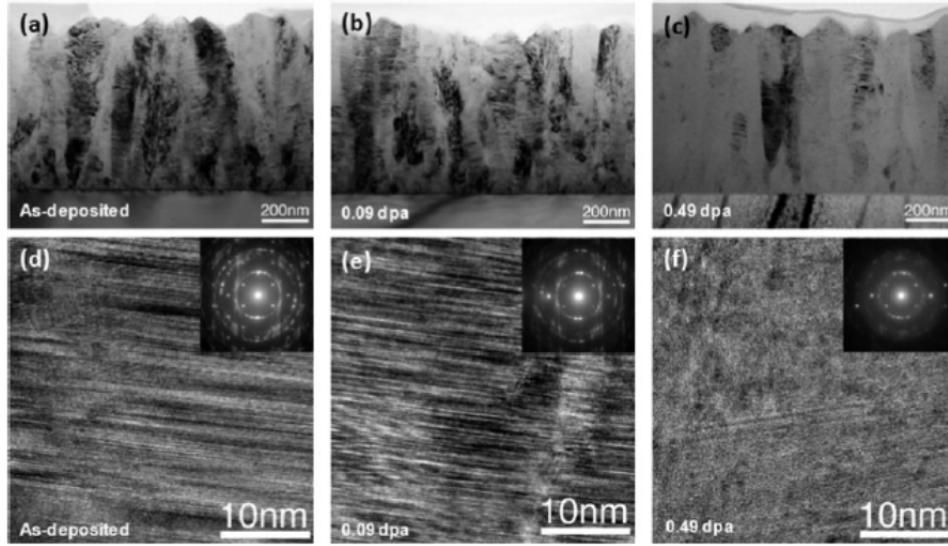


Figure 4.1.4 - TEM images of a thin section of the as-deposited films (a and d) and the films irradiated to $1.2 \times 10^{15} \text{ cm}^{-2}$, 0.09 dpa (b and e) and $6.6 \times 10^{15} \text{ cm}^{-2}$, 0.49 dpa (c and f). Electron diffraction patterns are included as insets for the corresponding irradiation dose.

A bright field TEM image of the tensile NE-SiC sample irradiated by 2 MeV Si⁺ ions to a high fluence of $3 \times 10^{16} \text{ cm}^{-2}$ is shown in Fig. 4.1.5. Strong layered diffraction contrast in the TEM image (marked by an ellipse in Fig. 4.1.5), and a high resolution image of the same area clearly show an amorphous/crystalline lamellar structure. The corresponding SRIM predicted dose profiles for the whole ion range and for the NE-SiC film are overlaid on the corresponding TEM micrographs in Fig. 4.1.6. The predicted damage peak (17 dpa) is located at a depth of about 1500 nm in the Si substrate, as shown in Fig. 6(a). The interface of the NE-SiC and Si substrate is clearly observable. Due to the nature of the energy loss processes for energetic ions, the local dose under the current irradiation conditions is lower at the surface than that at the interface, as shown by the SRIM prediction in Fig. 6(b). The implanted Si peaks at B1600 nm, with a maximum concentration of B1.5% in the NE-SiC film. The influence of any non-stoichiometric effect due to the implanted Si is considered negligible. The lamellar structure shown in both Fig. 4.1.5 and 4.1.6(b) indicates that eventually defect accumulation at or between the stacking faults results in some amorphization. Because of the increased disorder along the stacking faults, the columnar shaped nano-grains essentially subdivide along the SFs. The amorphous/crystalline lamellar structure shown in Fig. 4.1.5 can be viewed as a decrease in the effective grain size, which is reflected in the peak broadening in the GIXRD spectra shown in Fig. 4.1.2. The stable GBs of the columnar structure up to high irradiation doses suggest that the bonding structure of the GBs in NE-SiC may be radiation resistant; detailed studies are being conducted to identify unique mechanisms. Moreover, these GBs play an important role in stabilizing the SFs. The observation of the lamellar structure shown in Fig. 4.1.5 provides clear evidence in support of the critical role of stacking faults in enhancing the radiation resistance of the NE-SiC structure.

Amorphization of NE-SiC film by irradiation with 2 MeV Si to $3 \times 10^{16} \text{ cm}^{-2}$ can be observed near the interface in the TEM images shown in Fig. 4.1.5 and 4.1.6(b). While the TEM images and electron diffraction pattern indicate the existence of SiC crystallites or lamellar structure in the top most part of the

film, the bottom of the film near the interface with the substrate is completely amorphous based on the electron diffraction pattern (Fig. 4.1.5, left bottom inset). Due to the nature of ion-solid interactions, non-uniform irradiation damage is produced along the ion path, as shown in Fig. 4.1.6. The local dose in the NE-SiC film is 1.7 dpa at the surface and about 3.5 near the SiC/Si interface. Since the bottom of thin film receives a larger damage dose than that at the top, the transition of the film from crystalline at the surface to fully amorphous at the interface is understandable. Based on the depth of the crystalline-amorphous range in Fig. 4.1.5 and 4.1.6(b), the critical dose for amorphization is estimated to be about 3 dpa in the NE-SiC at 300 K. Based on both XRD and TEM results for the NE-SiC and RBS results for the 3C single crystal, the 3C NE-SiC demonstrates improved radiation performance, with an order of magnitude increase in radiation resistance.

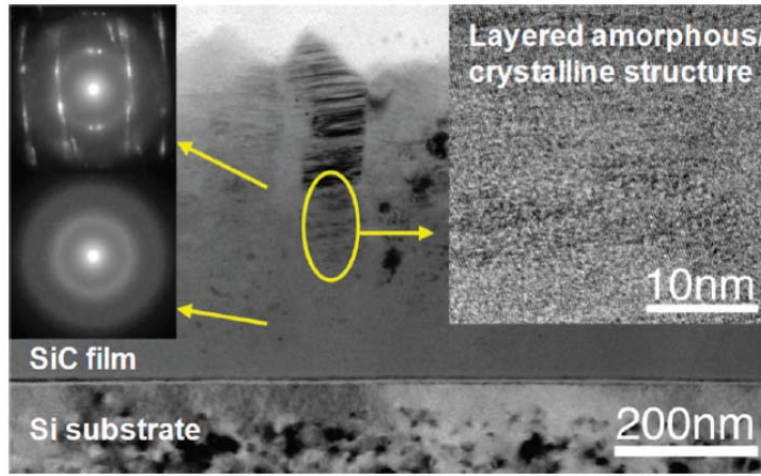


Figure 4.1.5 - TEM images of a thin section of the film irradiated by 2 MeV Si irradiation to $3 \times 10^{16} \text{ cm}^{-2}$. Diffraction contrast in the bright-field image indicates the existence of crystalline layers. The SAED patterns of the middle and bottom regions of the film are shown as insets. The high-resolution TEM image (right inset) reveals the existence of the lamellar structure consisting of amorphous and crystalline layers.

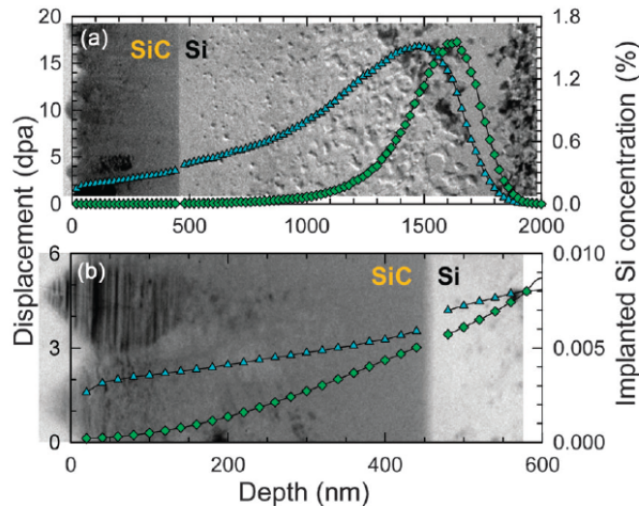


Figure 4.1.6 - SRIM predicated damage profile in displacements per atoms and doped Si concentration are overlaid on the TEM images for the sample irradiated by 2 MeV Si to ion fluence of $3 \times 10^{16} \text{ cm}^{-2}$: (a) the whole ion range, and (b) details of the NE-SiC film.

In order to obtain additional insights on defect evolution and amorphization mechanisms, a defect-stimulated and damage accumulation model¹⁵ was fit to the data in Fig. 4.1.1. In this model, the total disorder, S , produced by ion irradiation is given by $S = f_a + S_d$, where f_a is the contribution from amorphous clusters and domains that constitute an amorphous fraction, and S_d is the contribution from isolated point defects and small defect clusters in the residual crystalline regions. The amorphous fraction, f_a , is given by the expression $f_a = 1 - (\sigma_a + \sigma_s) / \{\sigma_s + \sigma_a \exp[(\sigma_a + \sigma_s)D]\}$, ⁴⁴ where σ_a is the amorphization cross section, σ_s is the effective cross section for defect-stimulated amorphization, and D is the local dose (dpa). The contribution of isolated point defects and small defect clusters can be described as $S_d = S_d^* [1 - \exp(-BD)] (1 - f_a)$, where S_d^* is the saturation value for the defect-induced disorder that is proportional to the local displacement rate, and $\sim (\text{dpa}^{-1})$ is proportional to an effective recombination volume for the specific defects giving rise to S_d .

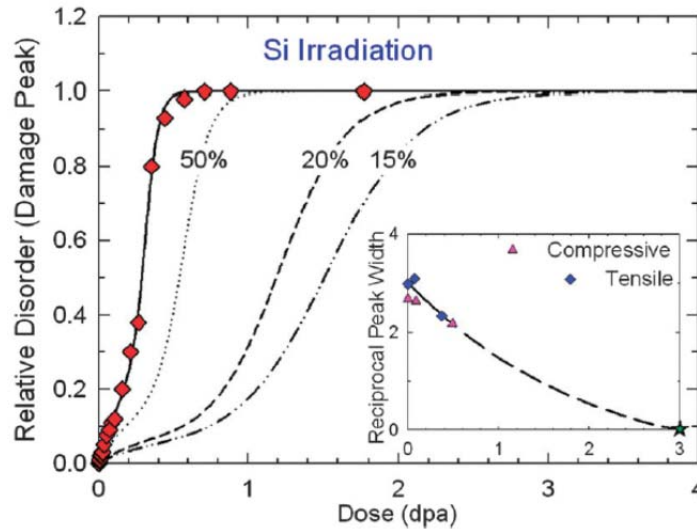


Figure 4.1.7 - Damage accumulation in single crystal SiC under 550 keV Si irradiation. The shift of the damage accumulation to higher dose is attributed to dynamic recovery of point defects, where 50% (dotted line), 20% (short dashed line), and 15% (dot-dashed line) defect survival is assumed relative to the single crystal case. The inset shows that the reciprocal of the 3C(111) peak width (1/degree) determined by GIXRD decreases with the irradiation dose (dpa), and full amorphization of the NE-SiC samples is attained at ~3 dpa (star determined by TEM). The dashed line is the extrapolation between the GIXRD and TEM results to guide the eye.

In this model, defect clusters or amorphous nuclei may directly be produced in the core of a cascade (σ_a term), and the irradiation-induced point defects accumulate and stimulate further amorphization (σ_s term). Parameters S_d^* (defect concentration) and B (recombination volume) reflect the contribution from the isolated point defects. Sigmoidal disorder accumulation, as shown in Fig. 4.1.1, is observed under Si irradiation. The model results suggest that, for single crystal SiC, the amorphization process is controlled by the cross section σ_a and σ_s for direct amorphization and the effective cross section for defect-stimulated amorphization, respectively. Under low-dose irradiation, disorder behaviour is dominated by the accumulation of isolated point defects. In the region where the disorder increases nearly linearly with dose, amorphization is dominated by defect-stimulated amorphization (much larger σ_s than σ_a , as shown in the inset in Fig. 4.1.1) where defect accumulation from cascade overlap leads to the growth of

amorphous nuclei. Further increase of irradiation dose leads to coalescence of amorphous domains. If there are less amorphous nuclei or immobile defect clusters produced directly within the cascades (small σ_a) or less surviving defects (suppressed σ_s) to drive amorphization, the accumulation of disorder will be substantially reduced. Under Si irradiation, a small σ_a is suggested by the model fit shown in Fig. 4.1.1, which is also confirmed by the MD simulation in Fig. 4.1.3, as few clusters are produced by the Si PKAs. Assuming fewer surviving defects in NE-SiC, shifts of damage accumulation to higher dose are predicted in Fig. 4.1.7, for cases where the point defect survival is decreased to 50%, 20% and 15% relative to that in single crystal SiC. It is worth noting that the delay of amorphization is mainly attributed to the suppressed defect accumulation at low disorder levels (below ~ 0.2). The results from experimental measurements, MD simulation, model fit and its predictions suggest that radiation tolerance is determined by how well the microstructure can effectively remove point defects.

Enhanced radiation tolerance in NE-SiC is clearly evident. The sharp 3C (111) peaks in Fig. 4.1.2 indicate well-retained crystalline structure in NE-SiC at doses of up to 0.49 dpa. The broadening of the 3C (111) peak (Fig. 4.1.2) is attributed to some increasing amount of disorder from the accumulation of point defects and formation of layered amorphous domains with increasing dose. The decrease in peak width (the effective crystallite size) with increasing dose, shown in Fig. 4.1.7 as an inset, is due to the development of an amorphous/crystalline lamellar structure. Complete amorphization in the NE-SiC samples is eventually achieved at a local dose of 3 dpa, as estimated from the TEM images in Fig. 4.1.5 and 4.1.6(b), which indicates an order of magnitude increase in radiation resistance relative to 3C-SiC single crystals (amorphization dose of 0.29 dpa under Si irradiation). Comparing the results in Fig. 4.1.7, about 80% to 85% of the point defects that would survive in the 3C single crystal may be annealed in the NE-SiC. This suggests a defect survival rate as low as 15–20% in the NE-SiC samples relative to that for single crystal SiC.

The decrease in point defect survival may result from enhanced annihilation of point defects at GBs in the nanosized grains; however, the contributions of GBs alone are not believed to be the primary factor for the remarkable radiation resistance behaviour observed in the NE-SiC. The effects of GBs on radiation damage accumulation have been demonstrated in large-grained polycrystalline SiC under irradiation at high-temperatures (>1100 °C),⁴⁵ where defect denuded zones of only a few tens nm thickness are observed near GBs, and grain interiors possess high-densities of extended defects. If the grain size is less than the characteristic defect denuded zone for given irradiation conditions (dose rate and temperature), then defect accumulation should be minimal in the grain interiors, which is essentially the underpinning concept for increased radiation tolerance in nanocrystalline materials. Although denuded zones may be established at GBs⁴⁵ where the point defect concentrations are lower than the intragrain concentrations, the denuded zone is primarily a high-temperature phenomena where interstitials and vacancies are both mobile. The denuded zone width in chemical-vapor deposited 3C SiC with grain size between 5 and 10 nm is observed to be 8.9, 17 and 57 nm under neutron-irradiation at 1010, 1130 and 1380 °C, respectively.⁴⁵ Furthermore, the temperature-dependent diffusion coefficient⁴⁵ suggests that such denuded zones are negligible at room temperature in 3C SiC, which is also supported by the lamellar structure perpendicular to the GBs in our TEM observation, and, therefore, cannot account for the extraordinary defect annihilation observed in the current work. The lack of effective denuded zones in SiC at room temperature is consistent with previous MD results that indicate point defects are stable within atomic distances of GBs in NC-SiC.^{17,22} Previous MD studies also confirm that grain size does

not significantly affect defect production¹⁷ or has a limited effect above 20 nm;²² thus, defect production is expected to be unaffected by GBs in the current samples that have an average grain size of ~60 nm and above in the NE-SiC films used in this study.

Based on the integrated experimental and simulation results from the current study, we propose a new mechanism of defect annihilation: stacking fault enhanced defect annihilation. Compared to defect dynamics in single crystal or NC-SiC, the enhanced self-healing in NE-SiC is due to the high density of stacking faults, which we assume promote point defect recombination and annihilation through increased close-pair recombination, increased mobility of Si interstitials, changes in defect survivability within and near faults, and some restriction of the normal 3D-random walk diffusion of interstitial defects to interlayer diffusion. Stacking faults in 3C SiC are low-energy configurations that can be easily engineered into materials by controlled deformation and processing conditions. The nm-scale distances between the layered SF structures are much smaller than cascade dimensions; therefore, the majority of PKAs and secondary recoil atoms (SRAs) are dispersed across multiple SFs. In single crystal or NC-SiC, interstitials can recombine with immobile vacancies or annihilate at the GBs through a 3D random walk. In NE-SiC, SFs are structural disturbances to the ordered interaction forces and the low-energy migration channels, therefore, change barriers for diffusion that reflect and constrain interstitial migration. Due to the modified interstitial diffusion at the SFs, the normal 3D random walk diffusion process becomes a more 2D-like motion between the neighbouring SFs, and the probability of interstitial recombination with nearby vacancies is significantly increased. Moreover, the existence of the SFs could also impact collision cascades, leading to more localized point defect production and higher recombination rates. The lower defect production, increased mobility of Si interstitials, and confined 2D-like migration induced by the stacking faults could explain the enhanced defect annihilation in NE-SiC.

Previous studies on interfaces involved model bi-metallic nanolayered materials. Stacking faults in nanocrystalline materials provide a self-layered nanostructure in a monolithic material that maximizes interface areas to promote self-healing. 3C-SiC is not only a model material, but also a material with great potential and proven applications in nuclear technology. While demonstrated for irradiation-induced amorphization at room temperature, the enhanced radiation resistance is expected to be effective at the higher temperatures in nuclear applications. The extraordinary self-healing of the SFs demonstrated by the integrated experimental and computational work presented here may have significant implications for the design, discovery and development of a broader class of novel materials.

4.2: Origins of radiation tolerance in nanolayered SiC

Structural changes in SiC with a high-density of planar defects, under electron beam are examined via irradiation by in situ transmission electron microscopy (TEM). As a consequence, we found that irradiation-induced point defects migrate two dimensionally within the nanolayers defined by the (111) planar defects, and we propose that defect annihilation is effectively enhanced by this defect behavior. The TEM samples were then irradiated at ambient temperature with a 300-keV electron beam at various fluxes using a JEOL JEM-3000 F TEM equipped with a field emission gun. The beam current density in the central part of the electron beam was measured using a Faraday cage by placing the electron beam away from the sample. TEM images and electron diffraction patterns were recorded on imaging plates

(Eu²⁺-doped BaFBr) which were developed by an imaging plate processor, a Digital Micro Luminography FDL 5000 system (Fuji Film).

Figure 4.2.1a shows a cross-sectional bright-field TEM image and selected-area electron diffraction pattern of a SiC thin film deposited on the Si substrate. The electron beam was incident along the nearly [110] direction of the substrate. From the distinct diffraction contrast, it is apparent that columnar growth occurs in the specimen; and as a consequence SiC nano-columns are formed. Their width becomes large with the progress of crystal growth. In addition to the Bragg spots from Si, rings due to 3C-SiC are observed in the diffraction pattern. It should be noted that the first ring corresponding to the 111 reflections of 3C-SiC possesses intensity maxima, as marked with arrows, along the growth direction, indicating that the nano-columns possess the (111) preferential orientation. Numerous band contrasts can be seen in some of the nano-columns of Fig. 4.2.1(a), and it has been confirmed that these contrasts are observable in most of the nano-columns by changing diffraction conditions. Figure 4.2.1(b) shows a high-resolution TEM image of a SiC nanocolumn, which is rotated nearly 90° counterclockwise compared to Fig. 4.2.1(a). In addition to the atomic arrangement corresponding to the [1 1 0] projection of 3C-SiC, many stacking faults (closed triangle) and twins (open triangle), with interval spacings of <10 nm, exist on the (111) plane, thus forming a nanolayered structure. The formation of the planar defects is consistent with the existence of streaks along the growth direction in the diffraction patterns. The stacking faults and twins nearly perpendicular to the growth direction are hereinafter referred to as (111) planar defects.

To examine the radiation response of SiC with such a high-density of (111) planar defects, we performed electron beam irradiation experiments. Figure 4.2.2 shows crosssectional bright-field images of the specimens (a) before and (b) after electron irradiation. In Fig. 4.2.2(a), a SiC nanocolumn with dark contrast is adjacent to the light contrast regions which correspond to the nano-columns with different crystallographic orientations. The samples were irradiated with a 300-keV electron beam at a flux of 2.6×10^{20} e/cm²/s, and the irradiation times (fluences) are 1800 s (4.7×10^{23} e/cm²). In contrast to electron irradiated bulk 6 H-SiC single crystal,²¹ no remarkable defect clusters are observed in Fig. 4.2.2(b). This suggests that the radiation-induced point defects are rapidly annihilated by the presence of the planar defects. A significant difference of damage accumulation processes was also observed in nanocrystalline materials relative to the bulk state.⁷²

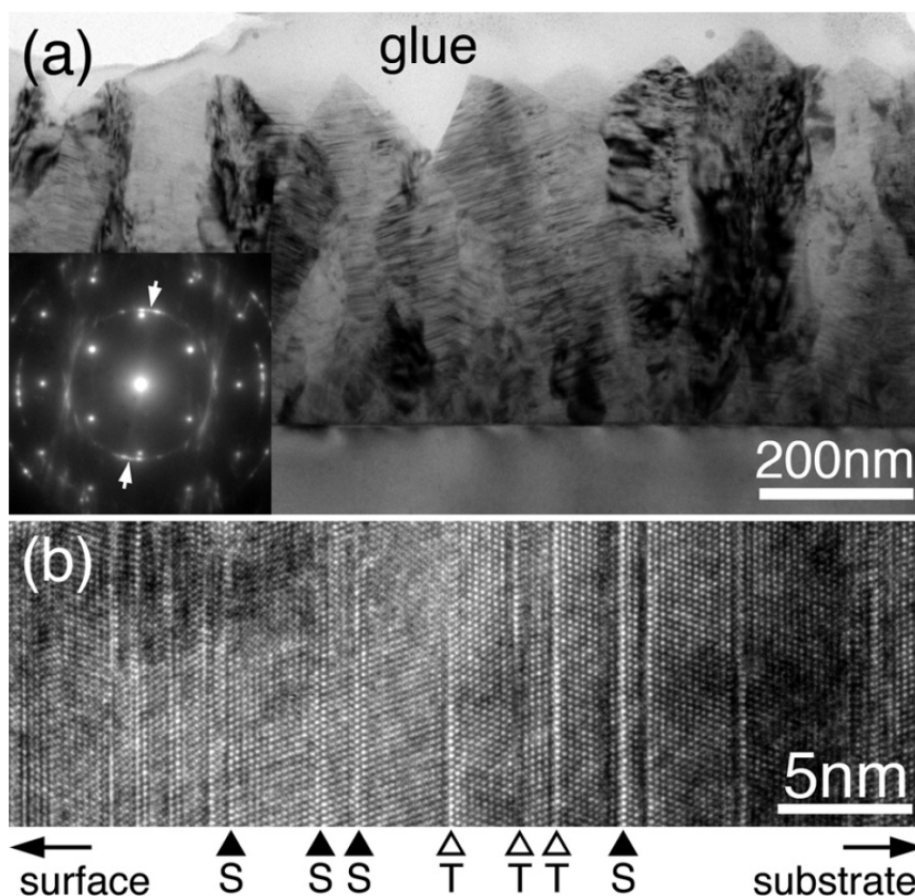


Figure 4.2.1 - (a) Cross-sectional bright-field TEM image and electron diffraction pattern of as-deposited SiC thin film. (b) High-resolution TEM image obtained from a SiC nano-column. Open and closed triangles denote twins and stacking faults, respectively.

Diffraction contrasts disappear at the locations marked with arrows in Fig. 4.2.2(b), indicating the occurrence of a crystalline- to-amorphous phase transformation.⁷³ In fact, it was confirmed that halo rings due to amorphous material appear in the electron diffraction patterns (not shown). It is apparent that the density of stacking faults becomes lower at the remaining crystal regions (e.g., see the location marked with a triangle in Fig. 4.2.2) and the nano-column becomes narrow at the encircled region. The crystal orientation is slightly changed after irradiation, and as a consequence, the diffraction condition is different between Figs. 4.2.2(a) and 4.2.2(b). It should be noted that the planar defects neighboring the one marked with a triangle are visible, and therefore, the disappearance of planar defects observed here is an essential phenomenon. In Fig. 4.2.2(b), we have intentionally performed electron irradiation for a long time in order to show remarkable amorphization. In this case, surface sputtering effects should be considered. Actually, compositional and structural changes due to the preferential sputtering of carbon atoms were observed in our previous study.⁷⁴ However, we confirmed that amorphization occurs at a short irradiation time, as described below, and therefore, the electron-beam induced structural changes observed here are not due to the surface sputtering during irradiation.

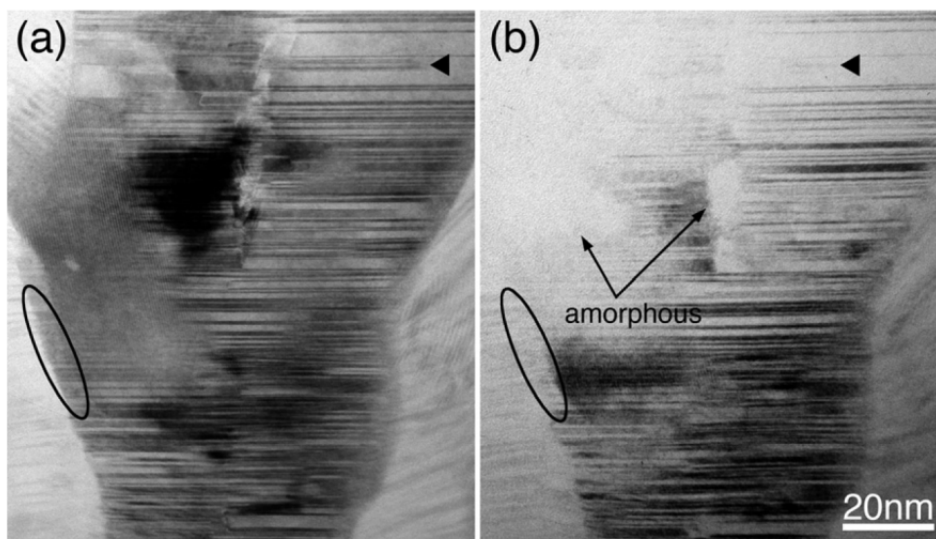


Figure 4.2.2 - Bright-field TEM images of SiC nano-columns (a) before and (b) after electron irradiation. Although the electron beam intensity is homogeneous in the displayed region, amorphization occurs heterogeneously.

Although the electron beam intensity is homogeneous in the region displayed in Fig. 4.2.2(b), amorphization occurs heterogeneously. To clarify the origin of the heterogeneous amorphization, structural changes during irradiation were examined using high-resolution TEM. Figure 4.2.3(a) shows a high resolution TEM image of a grain boundary of as-deposited specimen. The crystallite of the left-side corresponds to the projection in the pole-axis direction, while the one of the right-side satisfies only a two-beam condition. It is apparent that two crystalline phases are continuously connected and no amorphous layer exists at the boundary. After electron irradiation with 300 keV electrons at a flux of $3.8 \times 10^{20} \text{ e/cm}^2/\text{s}$ for 360 s, both the grains and grain boundary receive the radiation damage. The ordered atomic arrangements are still maintained at the grain in Fig. 4.2.3(b), whereas the grain boundary is highly damaged and amorphization occurs. This suggests that the damage accumulation preferentially occurs at the grain boundaries. As a consequence, the shape of grains is changed and the width of nano-columns becomes small with irradiation as observed in Fig. 4.2.2, which is also supported by the glancing-incident angle X-ray diffraction observation of increasing width of the 3C(111) main diffraction peak.¹⁵

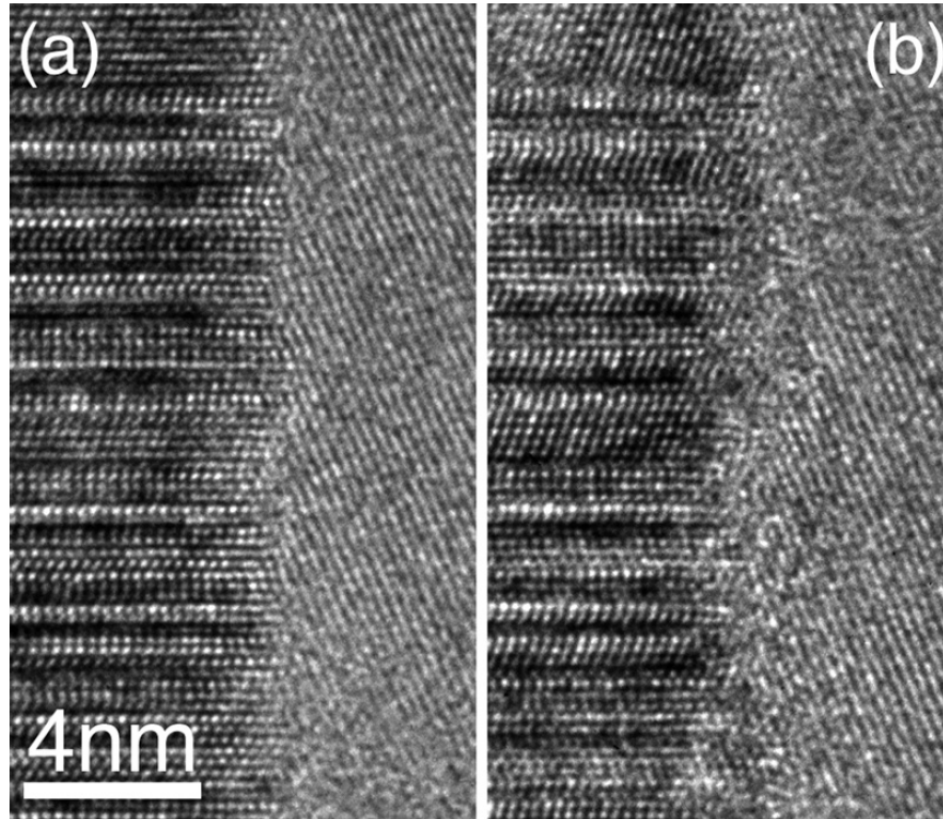


Figure 4.2.3 - Electron-beam-induced amorphization at a grain boundary. (a) Before and (b) after irradiation.

The electron-induced-amorphization was observed not only at the grain boundary but also inside the grain, as shown in Fig. 4.2.2(b). Figure 4.2.4 shows structural evolution of a single grain under electron irradiation. The electron beam was incident along the $[1\bar{1}0]$ direction, and the specimen was irradiated with 300-keV electrons at a flux of 2.2×10^{20} e/cm²/s for (b) 240 s (fluence: 5.3×10^{22} e/cm²), (c) 480 s (1.1×10^{23} e/cm²), and (d) 960 s (2.1×10^{23} e/cm²). In addition to the (111) planar defects, different defects marked with arrows can be observed in the grain (Fig. 4.2.4(a)). There are four equivalent (111) planes in 3C-SiC, and therefore, the additional defects are regarded as the $(\bar{1}\bar{1}\bar{1})$ and $(\bar{1}\bar{1}1)$ planar defects. Among these defects, small ones begin to amorphize first after electron irradiation (Fig. 4.2.4(b)) and the amorphous regions extend along the planar defect with increasing electron fluence (Fig. 4.2.4(c)). This suggests that radiation-induced point defects are preferentially trapped, as observed at the grain boundaries, and damage accumulates at the planar defects existing on a different plane. Complete amorphization occurs at the $(\bar{1}\bar{1}\bar{1})$ and $(\bar{1}\bar{1}1)$ planar defects in Fig. 4.2.4(d), while the crystallinity is maintained at the (111) ones.

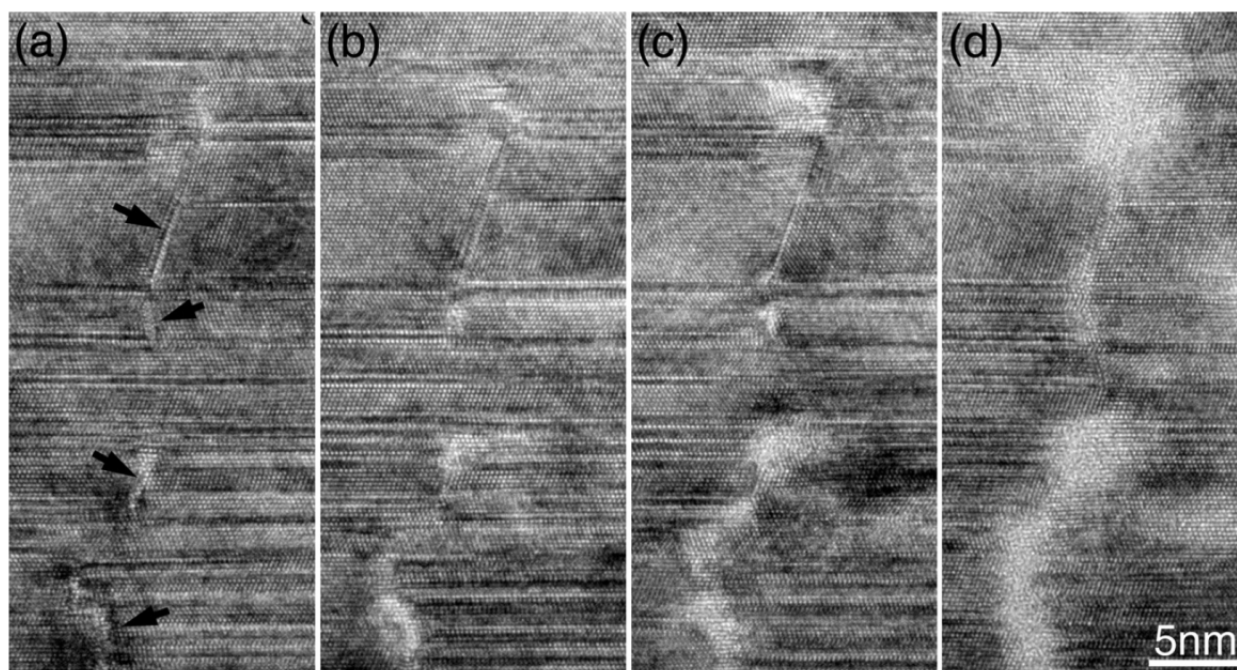


Figure 4.2.4 - Structural evolution of a SiC nano-column under 300-keV electron beam at a flux of 2.2×10^{20} e/cm²/s. Irradiation time (a) 0, (b) 240, (c) 480, and (d) 960 s.

Figure 4.2.5 shows a high-resolution TEM image obtained from the region adjacent to amorphous region marked with a white arrow. Interestingly, it is apparent that highly damaged (indicated by black arrows) and ordered layers are alternately stacked. The formation of a nanolayered crystalline/amorphous structure has been recently confirmed in ion irradiated SiC nano-columns,¹⁵ and the atomistic structure observed in Fig. 4.2.5 is regarded as the stage right before the start of amorphization. It should be noted that some of the spots and fringe patterns show different orientations from the original 3C-SiC. It is known that a remarkable volume swelling occurs in SiC during damage accumulation,^{75,76,77} and therefore, the crystal rotation is attributed to the inhomogeneous volume change between the highly damaged and ordered layers.

Electron irradiation produces point defects, primarily interstitials and vacancies. The formation of the layered damage structure in Fig. 4.2.5 suggests that the radiation induced point defects migrate between the (111) planar defects. The planar defects existing not on the (111) plane become barriers to defect migration and trap the point defects. This situation can explain the anisotropy effect of planar defects on radiation tolerance observed in Fig. 4.2.4. In this limited space, the interstitials and vacancies have an increased chance to annihilate each other; and as a consequence, the recombination and annihilation rates of defects increases. We propose that the two-dimensional limitation of defect migration is the origin of high radiation tolerance of SiC containing high-densities of planar defects.

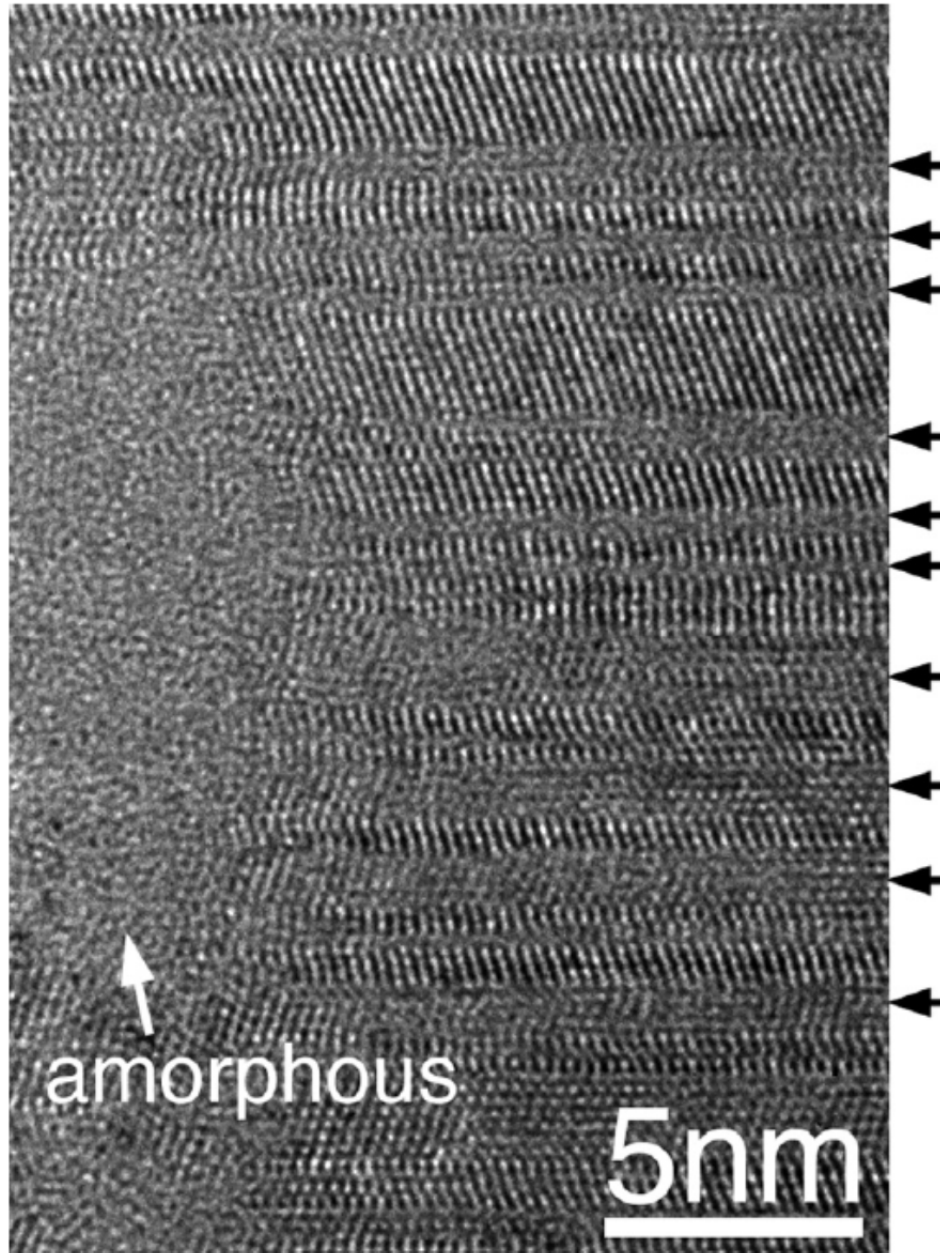


Figure 4.2.5 - High-resolution TEM image near an amorphous region. Highly damaged (marked with black arrows) and ordered regions are alternately stacked and a layered structure is formed.

4.3: Irradiation and in-situ measurement of SiC resistivity changes due to ion beam irradiation

The SiC thin film resistors described in Section 3.2 were irradiated at the University of Tennessee ion beam facility. Each individual sample was cleaved into a 1cm x 1cm square and stuck onto a stainless steel slat with double sided carbon tape. In addition to the samples, pieces of reflective glass were also placed on the slat which allowed beam operators to locate the beam and direct it onto the samples.

The stainless steel slat had a connector on the back which hooks into the vacuum chamber. Once the sample mount was placed in the chamber and it pumped down, the irradiations were performed.

The ion beam system can be configured to perform irradiations with a variety of ions. Silicon ions with an energy of 1 MeV will be used for the irradiation of 3C-SiC samples. The ion fluence each sample is irradiated with is directly related to the time exposed to the ion beam. The lowest ion fluence used was 5×10^{12} ions/cm² and the highest fluence was 1×10^{15} ions/cm². Irradiation times can range from a few 10's of seconds to over an hour per sample, depending on the ion fluence. There were two sets of experiments performed, tests on resistivity samples, and tests on p-n junctions. The tests were repeated twice, once on the samples with a 178.5 nm thick film, and again on the samples with a 328.5 nm thick film.

Based on fluence levels, damage to the SiC layer was estimated using TRIM. The goal of the irradiation experiment is to induce sparse damage in the SiC layer and deposit the ion in the silicon substrate on the other side of the insulating oxide layer. The first structure simulated using TRIM software was for the SiC/SiO₂/Si structure described in section 3.2. The simulations were performed twice, once for a 178.5 nm thick film, and again for 328.5 nm film. The conditions of the simulations are kept the same for all sample configurations. Ion distribution profiles were created for the implant of 1000 silicon ions with 1 MeV of energy. The simulations demonstrated the path of each ion in the samples, the peak damage location, and the number of collision events using the Kinchen-Pease model. The depth versus Y-axis figures above illustrates the path of each ion as it is implanted into the SiC/SiO₂/Si structures. There are not many observable differences between the profiles of the two sample thicknesses. A small number of ions stop in the thicker films. This result is demonstrated in Figure 4.3.1 illustrating the distribution of ion depths.

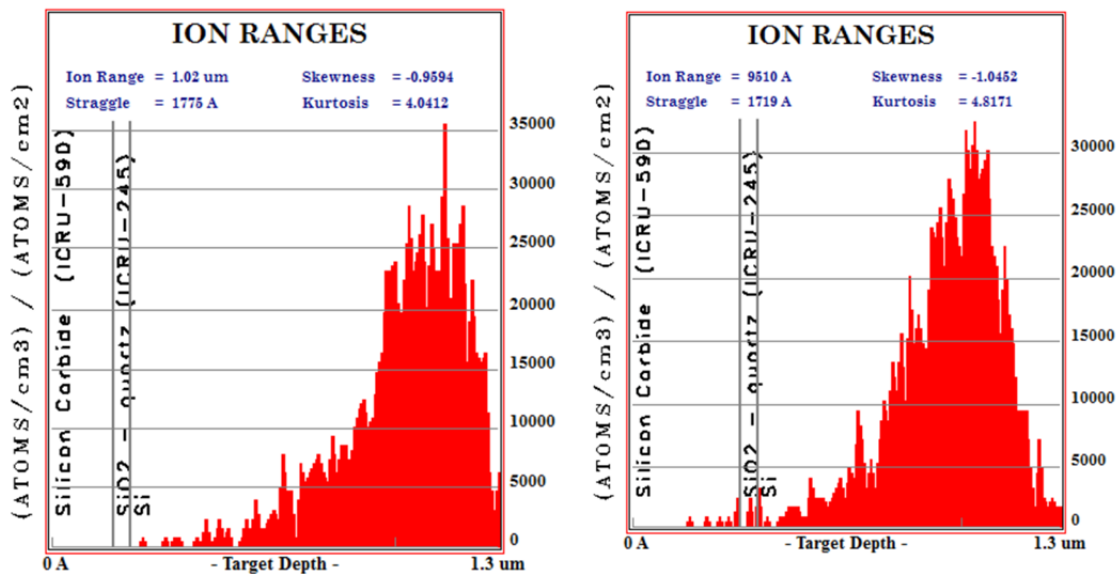


Figure 4.3.1 – ion ranges calculated in TRIM for the two thin film SiC resistor structures fabricated. Note that most ions reside on the insulated (right hand side) portion of the substrate.

The average range of a 1 MeV silicon ion implanted into the SiC/SiO₂/Si structure is 1.02 μ m when the 3C-SiC thickness is 178.5 nm. The average range decreases to .951 μ m when the 3C-SiC thickness is 328.5 nm. Inspection of Figure 4.3.1 indicates a small number of interstitials resulting from silicon ions stopping in the 328.5 3C-SiC film.

TRIM is also used to determine the number of collision events occurring in each layer of the SiC/SiO₂/Si structures. Figure 4.3.2 displays the number of vacancies created by each incoming ion. The software applies the Kinchen-Pease model in order to determine the number of vacancies created in each material. The number of vacancies produced due to each ion is an important parameter because it indicates the amount of damage accumulating in the 3C-SiC thin film. These values will also be useful for determining the dpa in each sample.

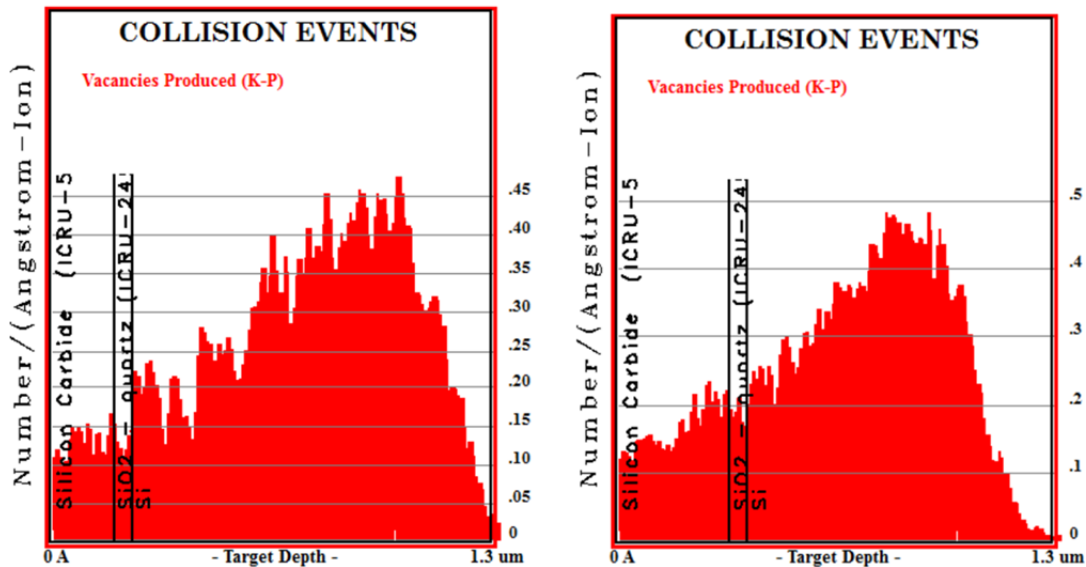


Figure 4.3.2 – Damage event profiles used to estimate DPA in the SiC resistor layer

There are several methods of determining the electrical characteristics of a device on a wafer. In order to perform these tests, a characterization system was purchased from Keithley® in order to measure parameters including but not limited to I-V curves and C-V curves. The tool which was utilized for electrical characterization of p-n junctions is the Keithley® 4200 Semiconductor Characterization System (SCS).

The Keithley® SCS purchased was configured with two preamplifiers (one preamplifier for each electrical contact) which allowed for the measurement of current-voltage parameters on scales in the femtoampere level. The resolution of the system allows for precise measurement of electrical parameters, allowing the user to detect any shifts in electrical properties resulting from low levels of radiation damage which otherwise may not be visible from TEM imaging.

The electrical connections of the Keithley® 4200 allow the system to be connected to a probing station via coaxial cables where the electrical properties of p-n diodes are measured. Once connected to a probing station, pins were placed on the ohmic contacts on the samples which then created a circuit where resulting current values could be measured for a range of electrical potentials. The Keithley® system then recorded and stored the data in Excel tables so that the results could be later analyzed. The Keithley® 4200 SCS presents numerous benefits, not only including its precision, but in its transportability. The future goal of the investigation for measuring I-V curves on p-n junctions is to make in-situ measurements at a radiation source. Once these devices are fabricated, the Keithley® 4200 SCS can be transported to the

ion beam at the University of Tennessee and real time I-V curves can be generated as the ion beam bombards the p-n junctions. This type of test will allow for real time monitoring of radiation damage in the 3C-SiC which may be applied in the future to extreme environment applications. Once this data is obtained the relation between radiation damage and electrical properties can be correlated, yielding a greater understanding of radiation effects in silicon carbide.

The configuration of the Keithley® 4200 with two current preamplifiers allows for the measurement of electrical properties on devices with two contacts. In order to measure other properties, including sheet resistivity of samples, additional preamplifiers are necessary. The measurement of sheet resistivity requires four electrical contacts. Since the addition of preamplifiers to the Keithley® 4200 SCS are expensive, and require the shipment of the system to the manufacturer, a four-point probe (pictured below) was utilized for the measurement of sheet resistivity of 3C-SiC samples.

The system then computes the sheet resistance of the sample in the units of Ω/square . This value can then be converted to resistivity by multiplying the sheet resistance by the thickness of the 3C-SiC layer. Resistivity analysis will be performed on the electronically isolated 3C-SiC films. The analysis with the Keithley® 4200 SCS and four-point probe will be performed twice on samples, before and after irradiation in order to understand how electrical properties change with varying levels of radiation damage.

Since the 3C-SiC discussed in this work has been doped, it is fairly conductive with a resistivity on the order of $0.04 \Omega\text{-cm}$. Radiation damage creates defects in a material which therefore inhibit the flow of current through the material. The relationship between various irradiation fluences and the increase in the resistivity of bulk 3C-SiC was observed. This experiment was performed on the SiC/SiO₂/Si structure, cleaved into $\sim 1 \text{ cm}^2$ squares. Eight samples were taken from the wafer with 178.5 nm thick 3C-SiC and another eight were taken from the wafer with 328.5 nm thick 3C-SiC. Samples were taken from wafers with two different 3C-SiC thicknesses in order to determine the effect of processing conditions on the accumulation of radiation damage. Once the samples were cleaved, preirradiation measurements were made on all 16 samples.

The preirradiation resistivities were measured using the four-point probe described in section 4.1. Each sample resistivity was measured in Ω/square then converted to $\Omega\text{-cm}$ by multiplying by the thickness of the film. Preirradiation resistivities for each of the eight 178.5 nm samples were all nominally $0.044 \Omega\text{-cm}$. The preirradiation resistivities for the 328.5 nm were nominally $0.05 \Omega\text{-cm}$.

The magnitude of the increase in resistivity of silicon carbide is related directly to the ion fluence used to irradiate each sample. Resistivity measurements were made on pieces of isolated 3C-SiC before irradiation and after irradiation using the same four-point probe. Resistivity as a function of fluence is shown in Figures 4.3.3 and 4.3.4 for 178nm and 328nm samples.

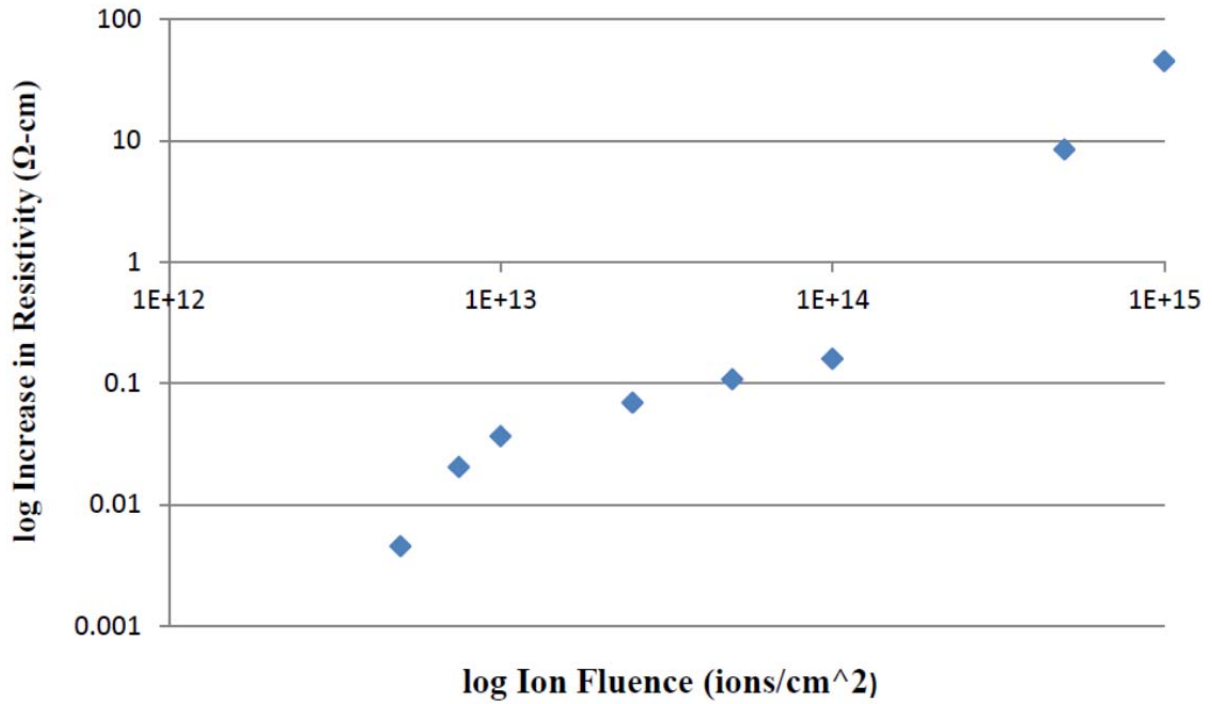


Figure 4.2.3 – resistivity vs. fluence for 178nm thick SiC thin film resistors.

The plot displaying the increase in resistivity as a function of ion fluence displays several trends. At low ion fluence values, the increase in resistivity is gradual, but steadily increases. At intermediate ion fluence values (up to 10^{14} ions/cm²) the increase in resistivity appears to be reaching a maximum value at 0.158776 Ω-cm. At an ion fluence of 5×10^{14} ions/cm², the change in resistivity increases substantially. The increase occurring between 1×10^{14} ions/cm² and 5×10^{14} ions/cm² is over 50 times the previous increase value. A similar trend is present on the samples with 328.5 nm of 3C-SiC. The increase in resistivity of 328.5 nm silicon carbide also undergoes a large increase between ion fluence values of 1×10^{14} ions/cm² and 5×10^{14} ions/cm².

The resistivity versus ion fluence data illustrated in section 5.1 indicate that electrical characterization is an effective means of detecting low levels of radiation damage in 3C-SiC. The increase in resistivity values occurring at ion fluence values on the order of 10^{12} ions/cm² provide a quantifiable indication of the accumulation of point defects occurring in the 3C-SiC. In order to better understand the level of damage created by each irradiation fluence, displacements per atom (dpa) values are determined. The dpa indicates the number of target atoms in the 3C-SiC lattice displaced per silicon ion. A dpa of 1 indicates that on average, every atom in the lattice has been displaced from its original position once. The dpa values are calculated using the collision events taken from TRIM, which were generated using TRIM software. The dpa determined by multiplying the number of vacancies N_V produced per ion occurring in the 3C-SiC by the ion fluence (ϕ), then dividing this value by the number of atoms per unit volume (V) of 3C-SiC.

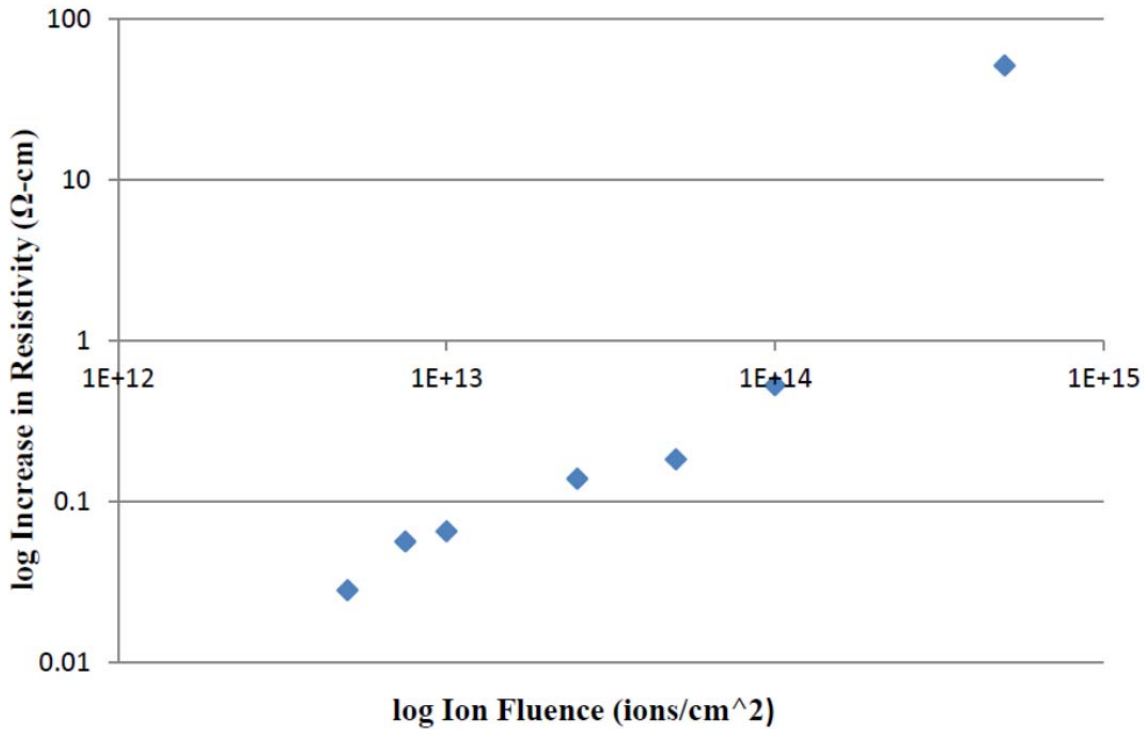


Figure 4.2.4 – resistivity vs. fluence for 328nm thick SiC thin film resistors.

Irradiations performed at ion fluence values of 10^{13} ions/cm² and below result in very small dpa values. For example, an ion fluence of 5×10^{12} ions/cm² causes an estimated dpa of 0.00078 for 178.5 nm 3C-SiC and of 0.00093 for 328.5 nm 3C-SiC. Using TEM imaging, it would be nearly impossible to identify damage in the crystals created at these doses.

The TEM results presented in Section 4.1 indicate that at an intermediate radiation dose of 0.09 dpa, the radiation effects become visible in the TEM images and in the electron diffraction patterns of the 3C-SiC. This level of damage is caused by the clustering of the accumulated vacancies. TEM images were not taken for smaller doses since there is not any significant change in the crystal structure.

The electrical characterization performed on 3C-SiC samples discussed in this chapter are a much more effective means of measuring low levels of damage than TEM imaging. A clear trend of radiation damage accumulated in the 3C-SiC as a function of dose is evident in Figures 4.2.3 and 4.2.4. An observable increase in material resistivity is evident for dpa values over two orders of magnitude smaller than the values used in the TEM images as seen warrants future work, including simulation modeling and additional testing.

The resistivity versus ion fluence plots indicate that at a fluence value of approximately $\sim 1 \times 10^{14}$ ions/cm², an evolution of defects occurs in the crystal structure of 3C-SiC. This rapid increase in resistivity can be explained with another TEM image shown in Section 4.1. Although significant damage accumulation occurs at ion fluences of 5×10^{14} ions/cm² and above, the large increase in resistivity can also be attributed to a change in contact resistance of the 3C-SiC. At larger damage levels, the quality of the film surface

which comes into contact with the four-point probe degrades. The increased contact resistance then contributes to the change in sheet resistance of the film when measured. Future work will be performed in order to distinguish the contribution of contact resistance to sheet resistance.

The accumulation of radiation damage in 3C-SiC irradiated at 0.49 dpa is much more evident than that of 3C-SiC irradiated at a dpa of 0.09. The 3C-SiC irradiated at 0.49 dpa is described by Zhang as having a “lamellar crystalline/amorphous structure”. The 3C-SiC begins to exhibit a level of amorphization, while maintaining some crystalline properties evident from the electron diffraction patterns. Full amorphization of the 3C-SiC lattice is estimated to occur at a dpa of approximately 3 by Zhang. TEM images of full 3C-SiC amorphization have not been produced since the irradiation time required to achieve this level of damage is too long. The transition of the 3C-SiC from crystalline to crystalline/amorphous may related to the transition point in the resistivity versus ion fluence curve.

The radiation tolerance of the 3C-SiC is attributed to the stacking faults in the grains of the material. These stacking faults allow for point defect migration to the grain boundaries, where they are subsequently annihilated. The steady increase in resistivity with irradiation dose can be explained by a combination of point defect accumulation and recombination at the grain boundaries [43, 51]. As defects are created, many are annihilated resulting in only a small increase in resistivity. Once the dpa is large enough, the crystal structure begins to transition into various levels of amorphization [48] since defects are created at a rate faster than which they can recombine. Additional ion fluence data points, on the order of 1×10^{14} ions/cm² to 5×10^{14} ions/cm² may indicate the nature of crystalline to crystalline/amorphous transition.

References

-
- ¹ Ohring, M. (2001, October 20). *Materials science of thin films*. Academic press
 - ² Freund, L.B., Suresh, S. (2003). *Thin Film Materials: Stress, Defect Formation, and Surface Evolution* (pp. 15–83). Cambridge University Press.
 - ³ Harsha, K.S. Sree (2005). *Principles of vapor deposition of thin films*. Elsevier. pp. 685-829
 - ⁴ Cheung, R., Zorman, C., Fu, X., Mehregany, M., Pearton, S. J., Zappe, S. (2006). *Silicon Carbide Micro Electromechanical Systems*. (R. Cheung, Ed.) (pp. 1–15, 18–42, 102–125, 128–147). Imperial College Press.
 - ⁵ Roy, S., Zorman, C., Mehregany, M., DeAnna, R., & Deeb, C. (2006). The mechanical properties of polycrystalline 3C-SiC films grown on polysilicon substrates by atmospheric pressure chemical-vapor deposition. *Journal of Applied Physics*, 99(4), 044108. doi:10.1063/1.2169875
 - ⁶ Serverino, A., C. Frewin, C. Bongiorno, R. Anzalone, S.E. Sadow, and F. La Via. (2009). Structural Defects in (100) 3C-SiC Heteroepitaxy: Influence of the Buffer Layer Morphology on Generation and Propagation of Stacking Faults and Microtwins. *Diamond & Related Materials* 18, 1440-1449.
 - ⁷ Madapura, S., A.J. Steckl, and M. Loboda. (1999). "Heteroepitaxial Growth of SiC on Si(100) and (111) by Chemical Vapor Deposition Using Trimethylsilane." *Journal of the Electrochemical Society* 146(3), 1197-1202.
 - ⁸ Fu, X.-A., Jezeski, R., Zorman, C. a., & Mehregany, M. (2004). Use of deposition pressure to control residual stress in polycrystalline SiC films. *Applied Physics Letters*, 84(3), 341. doi:10.1063/1.1640781
 - ⁹ Frewin, C. L., Locke, C., Wang, J., Spagnol, P., & Sadow, S. E. (2009). Growth of cubic silicon carbide on oxide using polysilicon as a seed layer for micro-electro-mechanical machine applications. *Journal of Crystal Growth*, 311(17), 4179–4182. doi:10.1016/j.jcrysgro.2009.06.037

- ¹⁰ Yun, J., Takahashi, T., Ishida, Y., & Okumura, H. (2006). Dependence of stacking fault and twin densities on deposition conditions during 3C-SiC heteroepitaxial growth on on-axis Si(001) substrates. *Journal of Crystal Growth*, 291(1), 140–147. doi:10.1016/j.jcrysgro.2006.03.005
- ¹¹ Carballo, J. (2010). Residual stress analysis in 3C-SiC thin films by substrate curvature method. Retrieved from <http://scholarcommons.usf.edu/etd/1590/>
- ¹² Capozzoli, Peter M. (2006). Structural and Electrochemical Characterization of Two Proton Conducting Oxide Thin Films for a Microfabricated Solid Oxide Fuel Cell. Retrieved from <http://dspace.mit.edu>.
- ¹³ Chason, E., Sheldon, B., Freund, L., Floro, J., & Hearne, S. (2002). Origin of Compressive Residual Stress in Polycrystalline Thin Films. *Physical Review Letters*, 88(15), 156103. doi:10.1103/PhysRevLett.88.156103
- ¹⁴ Gao, D., Howe, R.T., Maboudian, R. (2003). Characterization of residual strain in SiC films deposited using 1,3-disilabutane for MEMS application. *JM3*, 2(4), 259-264
- ¹⁵ Zhang, Y., Ishimaru, M., Varga, T., Oda, T., Hardiman, C., Xue, H., Katoh, Y., et al. (2012). Nanoscale engineering of radiation tolerant silicon carbide. *Physical chemistry chemical physics : PCCP*, 14(38), 13429–36. doi:10.1039/c2cp42342a
- ¹⁶ Reis, D. A., & Lindenberg, A. M. (2006). Ultrafast x-ray scattering in solids. *Light Scattering in Solid IX*, 371-422.
- ¹⁷ Lunev, A. V., & Tarasov, B. A. (2011). A classical molecular dynamics study of the correlation between the Bredig transition and thermal conductivity of stoichiometric uranium dioxide. *Journal of Nuclear Materials*, 415(2), 217-221.
- ¹⁸ Yakub, E., Ronchi, C., & Staicu, D. (2007). Molecular dynamics simulation of premelting and melting phase transitions in stoichiometric uranium dioxide. *The Journal of chemical physics*, 127(9), 094508.
- ¹⁹ Dent, A., Madden, P. A., & Wilson, M. (2004). Simulation of CaF₂ in the superionic state: comparison of an empirical and realistic potential. *Solid State Ionics*, 167(1), 73-81.
- ²⁰ Annamareddy, V. A., Nandi, P. K., Mei, X., & Eapen, J. (2014). Waxing and waning of dynamical heterogeneity in the superionic state. *Physical Review E*, 89(1), 010301.
- ²¹ X. Mei, "Hyperfaster Correlated Dynamics of Radiation Damage and Recovery in Materials," *PhD Thesis*, North Carolina State University (2013).
- ²² Kob, W., & Andersen, H. C. (1995). Testing mode-coupling theory for a supercooled binary Lennard-Jones mixture I: The van Hove correlation function. *Physical Review E*, 51(5), 4626.
- ²³ Chaudhuri, P., Berthier, L., & Kob, W. (2007). Universal nature of particle displacements close to glass and jamming transitions. *Physical review letters*, 99(6), 060604.
- ²⁴ R. Devanathan, W. J. Weber, and F. Gao, "Atomic scale simulation of defect production in irradiated 3C-SiC," *Journal of Applied Physics*, vol. 90, pp. 2303-2309, Sep 1 2001
- ²⁵ J. P. Chang, W. Cai, V. V. Bulatov, and S. Yip, "Molecular dynamics simulations of motion of edge and screw dislocations in a metal," *Computational Materials Science*, vol. 23, pp. 111-115, Apr 2002
- ²⁶ X.-M. Bai and B. P. Uberuaga, "The Influence of Grain Boundaries on Radiation-Induced Point Defect Production in Materials: A Review of Atomistic Studies," *Jom*, vol. 65, pp. 360-373, Mar 2013.
- ²⁷ T.-W. Chiang, A. Chernatynskiy, S. B. Sinnott, and S. R. Phillpot, "Interaction between voids and grain boundaries in UO₂ by molecular-dynamics simulation," *Journal of Nuclear Materials*, vol. 448, pp. 53-61, 2014
- ²⁸ L. Van Brutzel, J. M. Delaye, D. Ghaleb, and M. Rarivomanantsoa, "Molecular dynamics studies of displacement cascades in the uranium dioxide matrix," *Philosophical Magazine*, vol. 83, pp. 4083-4101, Dec 21 2003
- ²⁹ L. Van Brutzel and M. Rarivomanantsoa, "Molecular dynamics simulation study of primary damage in UO₂ produced by cascade overlaps," *Journal of Nuclear Materials*, vol. 358, pp. 209-216, Nov 30 2006
- ³⁰ R. Devanathan, J. Yu, and W. J. Weber, "Energetic recoils in UO₂ simulated using five different

potentials," *Journal of Chemical Physics*, vol. 130, May 7 2009

³¹ S. A. Taller and X.-M. Bai, "Assessment of structures and stabilities of defect clusters and surface energies predicted by nine interatomic potentials for UO₂," *Journal of Nuclear Materials*, vol. 443, pp. 84-98, Nov 2013

³² K. Govers, S. Lemehov, M. Hou, and M. Verwerft, "Comparison of interatomic potentials for UO₂. Part I: Static calculations," *Journal of Nuclear Materials*, vol. 366, pp. 161-177, Jun 30 2007

³³ S. T. Murphy, M. J. D. Rushton, and R. W. Grimes, "A comparison of empirical potential models for the simulation of dislocations in uranium dioxide," *Progress in Nuclear Energy*, vol. 72, pp. 27-32, Apr 2014

³⁴ Y. Ida, "INTERIONIC REPULSIVE FORCE AND COMPRESSIBILITY OF IONS," *Physics of the Earth and Planetary Interiors*, vol. 13, pp. 97-104, 1976 1976

³⁵ E. Yakub, C. Ronchi, and D. Staicu, "Molecular dynamics simulation of premelting and melting phase transitions in stoichiometric uranium dioxide," *Journal of Chemical Physics*, vol. 127, Sep 7 2007

³⁶ E. Yakub, C. Ronchi, and D. Staicu, "Computer simulation of defects formation and equilibrium in non-stoichiometric uranium dioxide," *Journal of Nuclear Materials*, vol. 389, pp. 119-126, May 15 2009

³⁷ D. Wolf, P. Koblinski, S. R. Phillpot, and J. Eggebrecht, "Exact method for the simulation of Coulombic systems by spherically truncated, pairwise $r(-1)$ summation," *Journal of Chemical Physics*, vol. 110, pp. 8254-8282, May 1 1999

³⁸ D. C. Rapaport, *The Art of Molecular Dynamics Simulation*: Cambridge University Press, 2004

³⁹ J. F. Ziegler, J. P. Biersack, and U. Littmark, *The Stopping and Range of Ions in Solids*: Pergamon, 1985

⁴⁰ C. B. Basak, A. K. Sengupta, and H. S. Kamath, "Classical molecular dynamics simulation of UO₂ to predict thermophysical properties," *Journal of Alloys and Compounds*, vol. 360, pp. 210-216, Oct 6 2003.

⁴¹ X.-M. Bai, A. F. Voter, R. G. Hoagland, M. Nastasi and B. P. Uberuaga, *Science* **327**, 1631 (2010).

⁴² M. J. Demkowicz, R. G. Hoagland and J. P. Hirth, *Phys. Rev. Lett.* **100**, 136102 (2008).

⁴³ A. Misra, M.J. Demkowicz, X. Zhang and R.G. Hoagland, *JOM* **59**, 62 (2007).

⁴⁴ N. Swaminathan, M. wojdyr, D. D. Morgan and I. Szlufarska, *J. App. Phys.* **111**, 054918 (2012).

⁴⁵ M. Kohyama, *Modelling Simul. Mater. Sci. Eng.* **10**, R31-R59 (2002).

⁴⁶ S. Plimpton, *J Comp Phys*, **117**, 1 (1995). (<http://lammmps.sandia.gov/>)

⁴⁷ R. Devanathan, T. Diaz. De la Rubia and W. J. Weber, *J. Nucl. Mater.* **253**, 47 (1998).

⁴⁸ Berthier, L., & Biroli, G. (2011). Theoretical perspective on the glass transition and amorphous materials. *Reviews of Modern Physics*, 83(2), 587

⁴⁹ Garrahan, J. P., & Chandler, D. (2003). Coarse-grained microscopic model of glass formers. *Proceedings of the National Academy of Sciences*, 100(17), 9710-9714.

⁵⁰ D. Chandler and J. P. Garrahan, *Annu. Rev. Phys. Chem.* 61, 191 (2010).

⁵¹ Keys, A. S., Hedges, L. O., Garrahan, J. P., Glotzer, S. C., & Chandler, D. (2011). Publisher's Note: Excitations are localized and relaxation is hierarchical in glass-forming liquids [Phys. Rev. X 1, 021013 (2011)]. *Physical Review X*, 1(2), 029901.

⁵² Gebremichael, Y., Vogel, M., & Glotzer, S. (2004). Particle dynamics and the development of string-like motion in a simulated monoatomic supercooled liquid. *The Journal of chemical physics*, 120(9), 4415-4427.

⁵³ Stillinger, F. H., & Hodgdon, J. A. (1994). Translation-rotation paradox for diffusion in fragile glass-forming liquids. *Physical review E*, 50(3), 2064.

- ⁵⁴ Bhattacharyya, S. M., Bagchi, B., & Wolynes, P. G. (2008). Facilitation, complexity growth, mode coupling, and activated dynamics in supercooled liquids. *Proceedings of the National Academy of Sciences*, 105(42), 16077-16082.
- ⁵⁵ Glotzer, S. C., Novikov, V. N., & Schröder, T. B. (2000). Time-dependent, four-point density correlation function description of dynamical heterogeneity and decoupling in supercooled liquids. *The Journal of Chemical Physics*, 112(2), 509-512.
- ⁵⁶ Toninelli, C., Wyart, M., Berthier, L., Biroli, G., & Bouchaud, J. (2005). Dynamical susceptibility of glass formers: Contrasting the predictions of theoretical scenarios. *Physical Review E*, 71(4), 041505.
- ⁵⁷ Dalle-Ferrier, C., Thibierge, C., Alba-Simionesco, C., Berthier, L., Biroli, G., Bouchaud, J., et al. (2007). Spatial correlations in the dynamics of glass forming liquids: Experimental determination of their temperature dependence. *Physical Review E*, 76(4), 041510.
- ⁵⁸ Karmakar, S., Dasgupta, C., & Sastry, S. (2010). Analysis of dynamic heterogeneity in a glass former from the spatial correlations of mobility. *Physical review letters*, 105(1), 015701.
- ⁵⁹ Karmakar, S., Dasgupta, C., & Sastry, S. (2009). Growing length and time scales in glass-forming liquids. *Proceedings of the National Academy of Sciences*, 106(10), 3675-3679.
- ⁶⁰ Berthier, L., & Kob, W. (2007). The Monte Carlo dynamics of a binary Lennard-Jones glass-forming mixture. *Journal of Physics: Condensed Matter*, 19(20), 205130.
- ⁶¹ Widmer-Cooper, A., Harrowell, P., & Fynewever, H. (2004). How reproducible are dynamic heterogeneities in a supercooled liquid?. *Physical review letters*, 93(13), 135701.
- ⁶² Widmer-Cooper, A., Perry, H., Harrowell, P., & Reichman, D. R. (2008). Irreversible reorganization in a supercooled liquid originates from localized soft modes. *Nature Physics*, 4(9), 711-715.
- ⁶³ Voter, A. F., Montalenti, F., & Germann, T. C. (2002). Extending the time scale in atomistic simulation of materials. *Annual Review of Materials Research*, 32(1), 321-346.
- ⁶⁴ See Supplemental Material at <http://link.aps.org/supplemental/10.1103/PhysRevE.89.010301> for more details
- ⁶⁵ Vogel, M., & Glotzer, S. C. (2004). Spatially heterogeneous dynamics and dynamic facilitation in a model of viscous silica. *Physical review letters*, 92(25), 255901.
- ⁶⁶ Bergroth, M. N., Vogel, M., & Glotzer, S. C. (2005). Examination of dynamic facilitation in molecular dynamics simulations of glass-forming liquids. *The Journal of Physical Chemistry B*, 109(14), 6748-6753.
- ⁶⁷ Gokhale, S., Nagamanasa, K. H., Ganapathy, R., & Sood, A. (2014). Growing dynamical facilitation on approaching the random pinning colloidal glass transition. *Nature communications*, 5.
- ⁶⁸ Gillan, M. (1986). Collective dynamics in superionic CaF₂. I. Simulation compared with neutron-scattering experiment. *Journal of Physics C: Solid State Physics*, 19(18), 3391.
- ⁶⁹ Wolf, D., Koblinski, P., Phillpot, S., & Eggebrecht, J. (1999). Exact method for [21] Xue X, Kanzaki M. NMR characteristics of possible oxygen sites in the simulation of Coulombic systems by spherically truncated, 21 aluminosilicate glasses and melts: an ab initio study. *J Phys Chem B pairwise r summation. J Chem Phys*, 110, 8254-82.
- ⁷⁰ Jiang, L., Cheung, R., Hassan, M., Harris, a. J., Burdess, J. S., Zorman, C. a., & Mehregany, M. (2003). Fabrication of SiC microelectromechanical systems using one-step dry etching. *Journal of Vacuum Science & Technology B: Microelectronics and Nanometer Structures*, 21(6), 2998. doi:10.1116/1.1627804
- ⁷¹ Mattox, Donald M. 2010. "Chapter 6 - Vacuum Evaporation and Vacuum Deposition." In *Handbook of Physical Vapor Deposition (PVD) Processing (Second Edition)*, 195-235. Boston: William Andrew Publishing.
- ⁷² Birtcher, R., & Wang, L. (1991). Microstructural changes induced in Zr 3 Al and U 3 Si during irradiation of the crystalline state. *Nuclear Instruments and Methods in Physics Research Section B: Beam Interactions with Materials and Atoms*, 59, 966-969.
- ⁷³ H. Inui, H. Mori, and H. Fujita: Electron-irradiation-induced crystalline to amorphous transition in alpha-SiC single crystals. *Philos. Mag. B* 61(1), 107 (1990).

-
- ⁷⁴ Ishimaru, M., Bae, I., & Hirotsu, Y. (2003). Electron-beam-induced amorphization in SiC. *Physical Review B*, 68(14), 144102.
- ⁷⁵ Heera, V., Stoemenos, J., Kögler, R., & Skorupa, W. (1995). Amorphization and recrystallization of 6H-SiC by ion-beam irradiation. *Journal of applied physics*, 77(7), 2999-3009.
- ⁷⁶ Ishimaru, M., Bae, I., Hirata, A., Hirotsu, Y., Valdez, J. A., & Sickafus, K. E. (2005). Volume swelling of amorphous SiC during ion-beam irradiation. *Physical review B*, 72(2), 024116.
- ⁷⁷ Ishimaru, M., Hirata, A., Naito, M., Bae, I., Zhang, Y., & Weber, W. J. (2008). Direct observations of thermally induced structural changes in amorphous silicon carbide. *Journal of Applied Physics*, 104(3), 033503.